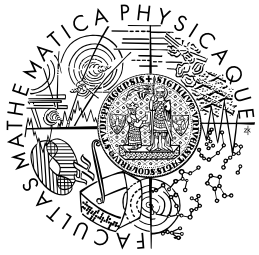

FACULTY
OF MATHEMATICS
AND PHYSICS
Charles University

MASTER THESIS

Juraj Jonák

A new study of orbital and long-term variations of the Be star φ Persei

Astronomical Institute of Charles University

Supervisor of the master thesis:	prof. RNDr. Petr Harmanec, DrSc.
Study programme:	Physics
Study branch:	Astronomy and Astrophysics

Prague 2022

I declare that I carried out this master thesis independently, and only with the cited sources, literature and other professional sources.

I understand that my work relates to the rights and obligations under the Act No. 121/2000 Sb., the Copyright Act, as amended, in particular the fact that the Charles University has the right to conclude a license agreement on the use of this work as a school work pursuant to Section 60 subsection 1 of the Copyright Act.

In ..... date ..... signature of the author

First and foremost, I would like to express my gratitude to my supervisor, prof. Petr Harmanec, for his suggestions, leadership and patience during this work, and to Dr. Miroslav Brož, for the enormous help with the `PYSHELLSPEC` modeling and the interpretation of the results. My special thanks goes to Dr. Denis Mourard, who instigated the topic of this thesis, for his teaching in the reduction process of interferometry data. I am also grateful to Dr. J. Nemravová for her work on the programs `PYSHELLSPEC` and `PYTERPOL` heavily used in this thesis, Dr. J. Budaj for the code `SHELLSPEC`, A. Harmanec for the new reSPEFO program, and to all the observers whose spectra I used. I would further like to thank my friend Jaroslav Jaroš for lending me useful hardware. Last but not least to my dear sister, my parents along with my entire family, who supported me during my studies.

Title: A new study of orbital and long-term variations of the Be star φ Persei

Author: Juraj Jonák

Institute: Astronomical Institute of Charles University

Supervisor: prof. RNDr. Petr Harmanec, DrSc., Astronomical Institute of Charles University

Abstract: The well-known spectroscopic binary φ Per is a peculiar compact system, composed of a Be star with an O-type subdwarf companion. A set of nearly 400 spectra in the red and blue regions from Ondřejov and Potsdam Observatories as well as spectra published in the BeSS database were examined. From the radial velocities of Hα, Hβ, and Hγ emission lines and FUV observations from the IUE and HST, a new precise ephemeris was determined. The revised values of $M \sin^3(i)$ are 11.84 and 1.48 $\mathrm{M}_\odot$ (with uncertainties of 0.64 and 0.09 $\mathrm{M}_\odot$), respectively, for the primary and secondary. In addition, the system shows cyclic variations (with a time scale of about 5 years) in the profiles of Balmer lines, manifested in their radial velocities, central intensities and V/R ratios.
Understanding complex stellar systems requires combining multiple types of observations and creating models of sufficient complexity. In our case, a combination of interferometric visibilities from the CHARA/VEGA array, spectral energy distribution as well as individual spectral lines were used. Radiative-transfer computations were performed with the program `PYSHELLSPEC`, and physical parameters of the φ Per primary and the surrounding disc were derived. They correspond to an evolved system, in which most of mass was transferred from the secondary to the primary, where the former gainer is almost critically rotating, while the donor contracted to the helium main sequence (after the ignition of He in its core).

Keywords: spectroscopic binaries – Be stars – orbital elements – long-term spectral variations

Contents

Introduction

The system φ Per has been examined for nearly 120 years and its exact properties are not yet fully explained. The primary is classified as a Be star because it shows multiple lines of Balmer series in emission while its companion is a stripped helium star. It is, in fact, a remnant of a previously more massive star that transferred most of its mass to the now primary. The primary, most likely spun up by the mass transfer, is rotating rapidly, reaching nearly the critical velocity. Furthermore it is surrounded by an optically thin disc where the observed emission (supposedly) originates.

To study (not only) these types of objects, it is often necessary to consider multiple sources of data as they provide different information. Optical interferometry constrains the spatial distribution of intensity and the angular dimension of the object. This is especially important for determining the distance to the object. Photometry is the base for the spectral energy distribution (SED) providing information about the total intensity in different passbands and thus define the level of the stellar continuum. Furthermore the differences between the observations in different bands give an estimate of temperature. Meanwhile observations of spectral lines tell us not only about the velocity fields in the system but also the presence of particular lines suggest the evolutionary stage of the system. The shape of the line indicates its temperature, density and composition.

The system provides valuable knowledge not only to shed further light onto the Be phenomenon but also to stellar evolution in close binaries. As the process of mass transfer has already ceased, it may serve as a comparison for models of systems with ongoing mass transfer.

The primary objective of this work is to create a model of radiative transfer in the system which is constrained by interferometric visibilities, SED and profiles of individual spectral lines, which are converged simultaneously. Before this is done, however, a set of nearly 400 spectra is analyzed and from the measurements of radial velocities a new value of ephemerid is derived.

1. Be stars

A Be star is a stellar object defined as [Jaschek et al., 1981, Collins, 1987] 'a non-supergiant B star whose spectrum has, or had at some time, one or more Balmer lines in emission'. The very first report of a star which such properties was made by Secchi [1867], who observed a luminous line in the spectrum of γ Cas. Nowadays the presence of a gas envelope was proven to produce the observed emission. However, despite a long history of observations, the mechanism giving rise to this phenomena is still unknown in the present day and several theories exist. It is also possible that multiple mechanisms can lead to the creation of such an envelope.

As summarized by Harmanec [1983], Be stars undergo multiple cyclic variations with timescales ranging from minutes up to tens of years. The long-term variations with years-long periods are the most pronounced ones and appear in the strength of the emission, changes in the violet-to-red emission peak ratio (V/R) and radial velocities (RV). These also depend on the inclination of the star: while stars viewed pole-on show positive correlation between the emission strength and the star's luminosity, stars seen edge-on show the inverse. The reason for this is the expansion of the disc-like envelope – while for pole-on stars the expansion of the envelope increases the apparent radius of the object, stars seen edge-on are dimmed by the cooler material.

One of the earliest model of Be stars was published by Struve [1931] who found that stars that have double emission lines also show extremely flat and broad absorption lines. This suggests rapid rotation of the star, which causes the star to become oblate in shape ejecting matter at the equator. The matter then forms a nebulous ring around the star and produces the observed emission line. The width of the line depends on the inclination of the star's rotational axis. Although every Be star seem to be a fast rotator, they do not necessarily rotate critically and a boost of 100 $\mathrm{km \cdot s^{-1}}$ may be necessary for an orbital ejection. There also exist rapidly rotating classical B stars such as Regulus [McAlister et al., 2005] which do not show any Balmer emission.

After discovering a binary nature of a number of Be stars, Kříž and Harmanec [1975] theorized that a majority of these objects are in fact interacting binaries. The observed changes in the spectra could then be explained as consequence of mass transfer between the components. As one of the stars might be more massive than the other it enters the red giant branch sooner than its less massive companion. It then starts to expand its outermost regions which may overflow the Roche lobe and in a circular motion fall onto the secondary.

Pols et al. [1991] suggested that (at least some portion of) the Be stars were indeed formed by this mechanism but are already past the mass transfer phase. These objects should then have either a helium star, a white dwarf, or a neutron star as a companion with helium stars being the most common (about 80%) of the three. Harmanec et al. [2002] formed a hypothesis based on gas-dynamical modeling of the surrounding envelope where the envelope might be formed via an outflow from the star due to the presence of the companion. This envelope is not axially symmetric and may cause a small mass transfer from the Be star towards the secondary.

Meanwhile detections of faint and extremely hot companions of Be stars started emerging, the first being φ Per [Gies et al., 1998, Mourard et al., 2015] and subsequently others: FY CMa [Peters et al., 2008], 59 Cyg [Peters et al., 2013], HR 2142 [Peters et al., 2016], 60 Cyg [Wang et al., 2017]. All were found from measurements by the International Ultraviolet Explorer spacecraft in the far-UV spectral region. Wang et al. [2018] suspects at least twelve additional candidates with many more systems where the stripped companion is too faint to detect.

The prevalence of binary systems is however not statistically supported as shown by Oudmaijer and Parr [2010], who using adaptive optics observations of 40 B stars and 39 Be stars discovered a similar number of binaries in each group (about 30%). However their focus were well-separated binaries with large mutual distance (by their estimation the sensitivity lies within the range of separation of the two components by 20–1 000 au). Consequently, these are very different from compact systems.

On the contrary, Bodensteiner et al. [2020], who examined known Be stars in the Galaxy, found no confirmed report of an early-type Be star with a main-sequence companion despite the fact that these objects should be easier to detect than the aforementioned hot but faint stripped dwarfs. They conclude that the lack of such systems is not due to an observation or statistical bias but is actually a consequence of the stellar evolution.

Rivinius et al. [2003] studied the far-UV a number of early-type Be stars and explained the short-time variations (0.2–5 d) of majority of these stars as non-radial sectoral pulsations. The remaining objects they were unable to reproduce by this model they suspect may pulsate in different modes, such as tesseral. However, as late-type Be stars are much less photospherically active, it is possible that this may not be the driving mechanism of the Be star phenomenon or that the mechanisms differ between early and late-type Be stars.

1.1 Disks surrounding Be stars

The presence of a disk-like circumstellar structure has become the generally accepted view after interferometric observations of ζ Tau by [Quirrenbach et al., 1994] discovering an elongated extended structure seen in Hα. In addition, the velocity field of the disk was confirmed as Keplerian (i.e. $v_\phi \propto r^{-1/2}$) from spectrally resolved interferometry [Meilland et al., 2007, Delaa et al., 2011].

A geometrically thin disk in vertical hydrostatic equilibrium supported by its rotation has, assuming ideal isothermal gas, a Gaussian vertical density distribution with scale height $H(r)$ [Bjorkman, 1997]

$$H(r) = \frac{c_s}{v_{\mathrm{orb}}}\sqrt{\frac{r^3}{R_\star}} = \frac{1}{v_{\mathrm{orb}}}\sqrt{\frac{\gamma kT}{\mu m_{\mathrm{H}}}}\sqrt{\frac{r^3}{R_\star}} \tag{1.1}$$

being proportional to the speed of sound c_s which can be expressed using gas temperature T, adiabatic constant γ, mean molecular weight of the gas μ and mass of hydrogen m_{H}.

The size of the disk is difficult to derive as one needs to distinguish between the disk's physical extent and the size of the emitting region in a given spectral

band and only the latter property can be observed.

The bulk properties of the disk can be linked to interferometric observations by modeling of radiative transfer in the circumstellar medium. The density of the disk is commonly assumed to follow a power law

$$\rho = \rho_0 \left(\frac{r}{R_\star} \right)^{-n} \tag{1.2}$$

with the slope in the range $n \in [1.5, 4]$ [Silaj et al., 2010] and base density $\rho_0 \in [10^{-12}, 10^{-9}]$ g·cm^{-3} [Tycner et al., 2006, Jones et al., 2008].

While the disks of many Be stars seem to be stable over time, there exist observations of disk dissipation where the emission gradually disappeared. Some examples include the stars 60 Cyg and π Aqr documented by Wisniewski et al. [2010]. On the contrary, some previously thought B-stars suddenly became enveloped in a disk, as was the case of δ Sco [Carciofi et al., 2006]. In general, most Be stars show some variability with periods of growth and dissipation of their disk.

As proposed by Okazaki [1991], the long-term V/R variations are caused by a global one-arm density wave in a Keplerian disk and have periods of years to decades. This is two orders of magnitude larger than the orbital period of the disk.

1.2 The Roche model

Deriving the properties of stars which do not follow spherical symmetry requires an analysis In this case, to describe the the shape of the star an approximation to first order can be used where it is assumed that all the mass of the star is concentrated in the star's centre while the mass of the surface layers is negligible. This allows us to treat the majority of the mass as point-like source of gravitational potential $\nabla\Phi$.

As the inside of the star is in hydrostatic equilibrium, the acting forces have to be in balance with pressure gradient ∇P. This also means that the equipotentials of these acting forces are identical to isobars. The surface of a star is usually defined as a surface where optical thickness is equal to $\frac{2}{3}$. It is however usually assumed that this surface coincides with a specific isobar, which in turn means that the surface of the star is given by an equipotential of acting forces.

1.2.1 Rotating star

We shall describe a rigidly rotating star with mass M with angular velocity ω in non-inertial co-rotating system in cylindrical coordinates l, ϑ, z with z-axis parallel to the axis of rotation and the point-like star at located the origin. Any point in the surface regions is affected by gravity of the centre, while due to the non-inertial description an additional, centrifugal, acceleration arises.

Thanks to the rigid rotation, we can describe effects of these two 'forces' using a potential

$$\Psi = \frac{GM}{\sqrt{l^2 + z^2}} + \frac{1}{2}\omega^2 l^2. \tag{1.3}$$

The set of points where the centrifugal force is in exact balance with gravity can then be found by

$$\nabla\Psi = 0 \tag{1.4}$$

which is fulfilled for a critical radius

$$R_{\mathrm{E}}^{\mathrm{crit}} = \sqrt[3]{\frac{GM}{\omega^2}}. \tag{1.5}$$

The level on this critical equipotential is then

$$\Psi^{\mathrm{crit}} = \frac{3}{2}\omega^2 (R_{\mathrm{E}}^{\mathrm{crit}})^2 \tag{1.6}$$

and the respective polar radius

$$R_{\mathrm{P}} = \frac{2}{3} R_{\mathrm{E}}^{\mathrm{crit}}. \tag{1.7}$$

Thus a star which is nearly critically rotating has an oblate shape with equatorial radius 1.5 times larger than the polar one.

As Rivinius et al. [2013] point out a possible misunderstanding in the definition of critical rotation: 'A star rotates critically, when the rotational velocity at the equator, v_{rot}, equals the Keplerian circular orbit velocity at the equator, v_{orb}'. In case of a non-critically rotating star with polar radius R_p and equatorial one R_e, its orbital velocity is lower than the critical velocity, increasing with faster rotation. One has to distinguish between v_{orb} and v_{crit} defined as

$$v_{\mathrm{crit}} = \sqrt{\frac{2}{3}\frac{GM}{R_p}}, \tag{1.8}$$

$$v_{\mathrm{orb}}(R_e) = \sqrt{\frac{GM}{R_e}}. \tag{1.9}$$

The quantity

$$W = \frac{v_{\mathrm{rot}}}{v_{\mathrm{orb}}} = v_{\mathrm{rot}} \sqrt{\frac{R_e}{GM}} \tag{1.10}$$

defines the necessary boost required to launch the material into orbit. In addition it is also useful to define the ratio of rotational and critical velocity

$$\alpha = \frac{v_{\mathrm{rot}}}{v_{\mathrm{crit}}} = v_{\mathrm{rot}} \sqrt{\frac{3R_p}{2GM}} \tag{1.11}$$

To calculate the shape of a non-critically rotating star, let us define a set of stars with equal masses M and polar radii R_p with different equatorial rotational velocities $v = \omega/R_e$. It is possible to rewrite Eq. (1.3) in terms of α as

$$\Psi = \frac{GM}{\sqrt{l^2 + z^2}} + \frac{GM\alpha^2 l^2}{3R_p R_e^2}. \tag{1.12}$$

The left hand side of the equation holds true for the pole where $l = 0$, $z = R_p$, nullifying the second term and leaving $\Psi = GM/R_p$. For the equator, where

$l = R_e$, $z = 0$, substituting this value of Ψ gives the relation between R_e and R_p as

$$R_e = \frac{3R_p}{3 - \alpha^2}. \tag{1.13}$$

The general shape of a non-critically rotating star can thus, after applying this relation back to Eq. (1.12), be expressed as a set of points where

$$z^2 + l^2 - \frac{729R_p^6}{\left[27R_p^2 - (3-\alpha^2)^2\alpha^2 l^2\right]^2} = 0 \tag{1.14}$$

As was found by von Zeipel [1924], for an oblate star 'the effective temperature has its maximum value at the poles and its minimum value at the equator'. This effect was later named as gravity darkening and causes the poles to be brighter than the equator regions. This can be expressed as

$$T \propto g^\beta \tag{1.15}$$

where the von Zeipel's parameter $\beta = 0.25$ for fully radiative atmospheres, while in the case of convective atmospheres the value $\beta \approx 0.08$ is commonly used.

1.2.2 Binary star

A similar approach can be used when describing a system of two stars gravitationally bounded on an circular orbit. We shall describe this system in a cartesian co-rotating coordinate system following the orbit of the system with the more massive star in the origin. The system's x-axis shall be pointing towards the secondary star while z parallel to the axis of rotation and the whole system be scaled to a unitary radius of the orbit. We also shall note the mass ratio of the components as q.

In total, there are three forces acting on any point (x, y, z) - gravity of both of the stars located at $(0, 0, 0)$ and $(1, 0, 0)$ as well as a centrifugal force which depends on the distance from the rotation axis passing through the center of mass. Therefore the total acting potential scaled by the term GM_1 can be written as

$$\Omega = \frac{1}{\sqrt{x^2 + y^2 + z^2}} + \frac{q}{\sqrt{(x-1)^2 + y^2 + z^2}} + \frac{1}{2}(1+q)\left[\left(x - \frac{1}{1+q}\right)^2 + y^2\right] \tag{1.16}$$

and is commonly referred to as Roche's potential.

The condition for balance between the acting forces can again be written as

$$\nabla\Omega = 0 \tag{1.17}$$

and leads to a set of five points in the orbital plane also known as Lagrangian points. Three of these points lay in line with the components while the remaining two form each form an equilateral triangle with the mass points.

The position of the colinear points (i.e. $y = 0$) is given by an implicit equation for x which can be solved numerically

$$-\frac{\operatorname{sgn} x}{x^2} + \frac{q \operatorname{sgn}(x-1)}{(x-1)^2} + (1+q)x - q = 0. \tag{1.18}$$

As the surface of a star coincides with an isobar of a specific level, surface layers of an expanding star may reach an equipotential containing the L_1 point lying between the two components. This critical equipotential is called the Roche lobe and exceeding it leads to mass transfer. If this happens, Kippenhahn and Weigert [1967] distinguished two cases of mass transfer depending on the distance between the two components:

- case A - slow expansion of the star still burning hydrogen in its core may lead to the primary filling its Roche lobe while still on the main sequence,
- case B - the primary dramatically expands after depleting all the hydrogen in the core and the mass transfer begins as it moves towards the red giant branch.

1.3 Introduction to optical interferometry

Interferometry in general is a method of obtaining information about the source (in our case a distant object) from observing the behaviour of interference fringes. The fringes are created by a combination of two light beams and the subsequent interference of these electromagnetic waves.

1.3.1 Interference of light waves

Due to its linearity, it follows that if both $E_1(r,t)$ and $E_2(r,t)$ are solutions of the wave equation, their sum is a solution to this equation as well. It is appropriate to use the complex representation of an electromagnetic wave (rather it electric component) as

$$E_i = \epsilon_i \exp\left[-\varphi_i i + i k_i r_i - i\omega_i t\right] \tag{1.19}$$

described by its amplitude ϵ, initial phase φ, wave number k and angular frequency ω. The observed intensity I of light is given by the square of this quantity.

The intensity of two interfering monochromatic light waves with same frequency is

$$I = |E|^2 = (E_1 + E_2)(\bar{E}_1 + \bar{E}_2) = \epsilon_1^2 + \epsilon_2^2 + 2\mathrm{Re}[E_1\bar{E}_2] \tag{1.20}$$

with $\bar{E}$ denoting the complex conjugate. For two waves with equal amplitude $\epsilon_1 = \epsilon_2 = \sqrt{I_0}$, this means the resulting intensity is modulated as

$$I = 2I_0\{1 + \cos\left[\varphi_2 - \varphi_1 + k_1 r_1 - k_2 r_2\right]\} \tag{1.21}$$

1.3.2 Light coherence

Light coherence describes the statistical property of electromagnetic wave and represents how 'well' two light beam interfere with each other. Temporal coherence represents how a wave interferes with itself shifted in time and depends on the bandwidth of the signal. If a beam of light consists of two wavelengths λ and $\lambda + \Delta\lambda$ the phase difference between these two waves after a time τ is

$$\phi = \left(\frac{1}{\lambda} - \frac{1}{\lambda + \Delta\lambda}\right) 2\pi\tau. \tag{1.22}$$

The correlation between these two waves drops significantly after time τ_c - coherence time, related to the coherence length l_c as the distance light travels during this time

$$l_c = \frac{\lambda^2}{\Delta\lambda}. \tag{1.23}$$

To quantify the effect of coherence, one can introduce a degree of coherence defined by taking the time-averaged product of two waves

$$\gamma_{12}(\tau) = \frac{\langle E_1(t)\bar{E}_2(t+\tau)\rangle}{\sqrt{I_1 I_2}}. \tag{1.24}$$

Similar to temporal coherence, spatial coherence is related to the correlation of the electromagnetic field in different places. This can be demonstrated using the Young's double slit experiment with two sources, which emit uncorrelated light. If the two sources are located at exactly the same place, we can see the typical fringes. However, shifting one of the sources perpendicularly to the line of sight causes a shift of one of the interference images. After a sufficient shift, the maxima of one set of fringes lie at the same place as the minima of the other set, thus the interference disappears.

The visibility of the interference fringes is closely related to the degree of coherence as

$$v = \frac{I_{\max} - I_{\min}}{I_{\max} + I_{\min}} = |\gamma_{12}|. \tag{1.25}$$

If one assumes that the following properties hold true for an observed object:

1. it is located in the so-called far observation field where the distance R is much larger than the observation area over observing wavelength D^2/λ,
2. it has a small angular diameter, and
3. it is spatially incoherent,

it is possible to formulate van Cittert's – Zernike's theorem which relates the spatial intensity distribution of the source and the degree of coherence for beams collected by two detectors in a plane perpendicular to the line of sight located at coordinates $(0,0,0)$ and $(X,Y,0)$.

Let us assume that a infinitesimally small area $\mathrm{d}S$ of this object located at coordinates (x,y,z) emitting a spherical wave in the form $E = \frac{A}{r}\exp(-i\omega t + kr)$. The phase difference between the two beams is given by the difference in optical path and time of arrival. Denoting R_1 and R_2 as the distance from the source to the respective detector, the resulting observed intensity is

$$I'(X,Y) = \left\langle E\left(0,0,t-\frac{R_1}{c}\right)\bar{E}\left(X,Y,t-\frac{R_2}{c}\right)\right\rangle \left|\frac{\exp(\frac{i\omega R_1}{c})}{R_1}\frac{\exp(\frac{-i\omega R_2}{c})}{R_2}\right|. \tag{1.26}$$

Due to the first assumption, the source is located far from the detectors and thus the time difference between the two terms is much smaller than the total time traveled. As A is the amplitude of the wave, the first term represents the intensity at the source, introducing angular quantities $\zeta = x/z$, $\eta = y/z$ leaves

$$I'(X,Y) = I(\zeta,\eta)\left|\frac{\exp(\frac{i\omega(R_1-R_2)}{c})}{R_1 R_2}\right|. \tag{1.27}$$

The geometry of the problem implies $R_1 = \sqrt{x^2 + y^2 + z^2}$ and taking into account the different position of the detector $R_2 = \sqrt{(x - X)^2 + (y - Y)^2 + z^2}$ where $z \gg x, y, X, Y$. Applying the Taylor series for $t \ll 1$: $\sqrt{1 + t} \approx 1 + \frac{1}{2}t$ and thus

$$|R_1 - R_2| = \frac{X^2 + Y^2}{2z} - \frac{Xx + Yy}{z} = \phi_{XY} - (X\zeta + Y\eta). \tag{1.28}$$

The incoming intensity from the entire object is simply an integration over its area

$$I'_{\text{total}}(X, Y) = \iint \frac{I(\zeta, \eta)}{R^2} \Big| \exp[i\phi_{XY} - i\omega(X\zeta + Y\eta)] \Big| dS. \tag{1.29}$$

The area element can be expressed by the two angular quantities as $\mathrm{d}S = R^2 \mathrm{d}\zeta \mathrm{d}\eta$ and at the same time the distances differ by only a small margin $R_1 \approx R_2 \approx R$, this finally yields the result

$$\gamma_{12}(X, Y) = -\exp(i\phi_{XY}) \frac{\iint I(\zeta, \eta) \exp\left[-2\pi i \frac{X\zeta + Y\eta}{\lambda}\right] \mathrm{d}\zeta \mathrm{d}\eta}{\iint I(\zeta, \eta) \mathrm{d}\zeta \mathrm{d}\eta}. \tag{1.30}$$

Van Cittert's – Zernike's theorem thus directly connects the spatial Fourier transform $\mathcal{F}$ of the source intensity to the observed visibility of fringes.

1.3.3 Application in astronomy

The projected distances between the two detectors X and Y are commonly denoted as u and v which are oriented in the S-N and W-E directions respectively. These two quantities can also be expressed in terms of spatial frequencies $u_f = 2\pi u/\lambda$. The baseline is the modulus of a (u, v) coordinate

$$B = \sqrt{u^2 + v^2}. \tag{1.31}$$

In the case of optical interferometry, the detectors represent individual telescopes observing the source object. The light collected by these telescopes is directed through a set of optical paths in order to adjust for the difference of the optical path.

A set of interferometric measurements forms a (u, v) map, where each observation is represented by two points – the direct and opposite vector of the two telescopes. The rotation of the Earth causes the (u, v) location of each measurement to depend on the time of observation as well.

For interferometers with sufficient baseline it is possible to resolve the diameter of a nearby star. A simple approximation for such object is a uniform intensity distribution in a disk of angular diameter θ, i.e. $I(\rho, \phi) = I_0 \Pi(\rho/\theta)$ described by the door function $\Pi(x)$ and transformed to radial coordinates $(\zeta, \eta) \to (\rho, \phi)$. The total intensity of the disk is $\pi I_0 \theta^2/4$. The corresponding Fourier transform is

$$F(I(\rho, \phi))(u, v) = I_0 \int_0^{2\pi} \int_0^{\frac{\theta}{2}} \exp\left[-2\pi i \rho (u \cos\phi + v \sin\phi)\right] \rho \mathrm{d}\rho \mathrm{d}\phi. \tag{1.32}$$

The term $u \cos\phi + v \sin\phi$ is purely a rotation in the (u, v)-plane with an angle ϕ. From the definition (eq. 1.31) this can be expressed as the baseline B and the

solution of the integral can be written in terms of the first order Bessel function J_1. The observed visibility is

$$V(B) = |\gamma_{12}(B)| = \frac{2J_1(\frac{\pi\theta B}{\lambda})}{\frac{\pi\theta B}{\lambda}}. \tag{1.33}$$

The dependence of V^2 with respect to the baseline for different values of the stellar diameter is shown in Fig. 1.1

A common target for interferometric observations are binaries. Similarly to a single star, each object can be approximated by a uniform disk of angular diameters θ_1, θ_2 and flux intensity I_1, I_2, respectively. Position of the second star relative to the first projected on the sky is $(\delta\zeta, \delta\eta)$. Fortunately, due to the linearity and the translation property of the Fourier transform, Eq. (1.30) can be written as

$$\gamma_{12}(u,v) = -\exp(i\phi_{XY})\frac{I_1\mathcal{F}(\Pi(\rho/\theta_1)) + \exp\left[-2\pi i\frac{\delta\zeta u+\delta\eta v}{\lambda}\right] I_2\mathcal{F}(\Pi(\rho/\theta_2))}{I_1+I_2}, \tag{1.34}$$

which after utilizing Eq. 1.33 and denoting the individual visibility contributions as V_1 and V_2, respectively, results in

$$V(u,v) = \left|\frac{1}{I_1+I_2}\left(I_1V_1(B) + I_2V_2(B)\exp\left[-2\pi i\frac{\delta\zeta u+\delta\eta v}{\lambda}\right]\right)\right|. \tag{1.35}$$

Usually the observed quantity, however, is the squared visibility, which in this case is

$$V^2(u,v) = \frac{1}{(I_1+I_2)^2}\left(I_1^2V_1^2 + I_2^2V_2^2 + 2I_1I_2V_1V_2\cos\left[2\pi\frac{\delta\zeta u+\delta\eta v}{\lambda}\right]\right). \tag{1.36}$$

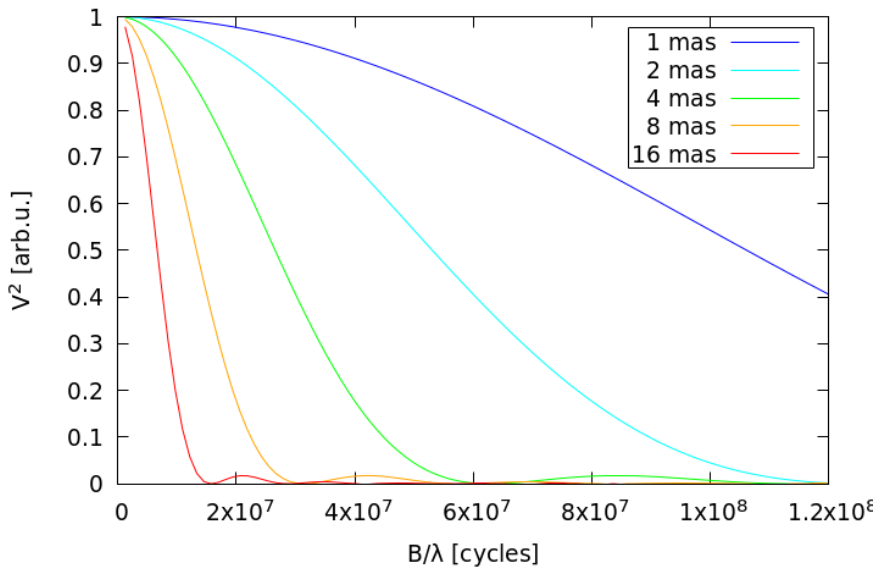

Figure 1.1: Theoretical squared visibility for objects of different diameters.

2. Historical research

2.1 Optical spectroscopy

2.1.1 Early observations, variability of φ Per

Observations of φ Per date back to the end of 19th century, first record of variability of radial velocities was published by Campbell [1902]. He discovered a change in radial velocity in Hγ of about 36 km·s^{-1} measured in its absorption core in five spectra taken between 1898 and 1901 with the Mills spectrograph.

Cannon [1910] obtained 120 spectral plates using a single prism spectrograph between December 1908 and January 1910. The main focus lied on hydrogen lines Hβ, Hγ, Hδ, Hϵ as well as He I λ4472 and Ca K line which appeared in the ascending slope of the RV curve. He assumed $126\overset{\mathrm{d}}{.}5$ period by Campbell [1902] and added their measurements together. However, as it was impossible to find a solution consisting of any pure elliptic motion he proposed a solution in the form of an additional satellite orbiting the star seen in the optical spectra. This satellite is supposed to cause tidal effects on the star and affecting the observed absorption as the observed strength of absorption is highest near the peaks of the RV curve.

Using the Potsdam 0.32-m telescope, Ludendorff [1910] measured 120 radial velocities of Hγ and found this absorption line to be varying in strength, at some times barely visible. However Cannon [1911] pointed out that despite their values were obtained at around the same time, the velocities of Ludendorff [1910] were of higher amplitude.

Jordan [1916] studied radial velocities measured on 112 plates between 1908–1911 using lines Hβ, Hγ, Hδ and Hϵ. All of these were observed as two emission peaks with a faint absorption core. However due to ambiguity of absorption profile in Hβ and emission profile in Hϵ as well as Hδ in some cases, some values were omitted. The RV curves for emission and absorption differed substantially in their velocity amplitudes and he also noticed differences between curves from individual cycles. He suspected a presence of an extensive chromosphere to explain the peculiarities of the spectra but claimed that "beyond this the system is a complete riddle" [Jordan, 1916].

Using a 9inch ($\approx$ 0.23 m) camera at Norman Lockyer Observatory, Lockyer [1925] obtained 55 more observations between years 1923 and 1925. The main focus were intensities of the violet and red emission peaks in Hβ and Hγ and their differences measured by a graduated wedge: for a symmetrical emission line superposed with an absorption core the asymmetry of the line is tied with motion of the absorption and therefore their measurements of V-R can be interpreted as a RV curve for the absorption core. The length of a period of these changes was estimated from 4 cycles as $128\overset{\mathrm{d}}{.}7$. This value did not agree with measured period in radial velocities of $126\overset{\mathrm{d}}{.}5$ by Cannon [1910] as well as $126\overset{\mathrm{d}}{.}6$ by Ludendorff [1910]. To correct this value Lockyer [1925] used epoch by Jordan [1916] and determined that for a constant period its value to be $126\overset{\mathrm{d}}{.}8$. He also suggested an existence of a secondary period of 21 d seen from the residuals of their RV curve as well as a variation in its brightness of two to three tenths of a magnitude as

the star should be dimmer when the absorption core is shallower, however, was not able to prove this.

All the previous observations were reviewed by Frédette [1925], who also re-measured about 50 plates by Jordan [1916], noting a much larger amplitude of the curves by Ludendorff [1910]. The curve of line intensity showed a period of half the velocity period suggesting that the absorption cores are in fact double. From this he suggested the secondary produces a weaker, underlying absorption line, while the emission and the main absorption coming from the primary are shifted slightly to the red and stationary with respect to each other. Furthermore, blending of these lines then causes the observed peculiarities in the velocity curve as well as the discrepancy between the data.

Continuing their research, Lockyer [1926] obtained 106 photographic spectra on 79 nights between 1925 and 1926 again focusing mainly on intensities of observed spectral lines measured using the wedge method. These new measurements due to being more numerous disproved previously found secondary period of 21 d. Instead he suggested an existence of activity pulses which are exhibited by absorption in hydrogen lines. He observed high-order Balmer lines (up to Hρ) that became well defined when low-order Balmer lines had sharpest absorption. Helium lines λ4471 and λ4026 showed variability in their profile, being sharp and strong near phases of zero radial velocity and weak and nebulous when approaching phases with peaks of RV. Thus he suggested a presence of secondary period, half as long as the orbital one. He also studied lines of ionised iron and titanium that were present in the spectra and discovered that these sharp double emission lines varied in relative intensities of their peaks, however these changes had no connection to phase.

Struve and Wurm [1938] noticed similar variation of He lines in ζ Tau and μ Sgr, namely for λ3965 to be always sharp and strong while others to be broad and diffuse but changing in phase. When these lines are sharper he assumed greater amount of He I gas in diluted radiation. he attempted to create a model describing the shell surrounding the B star where he considered only 3 singlet, 2 triplet and an ionized state and their calculation after corrected for collisions. As lines that originate in the outermost regions of the shell are sharp, he suggested the envelope's rotational velocity decreases with radius due to conservation of angular momentum. This shell also produces emission which is continuous and thus it weakens absorption lines.

Dustheimer [1939] used a 37.5 inch ($\approx 0.95\,\mathrm{m}$) telescope of Michigan Observatory to obtain 162 plates and compared these to the ones previously published. He found no evidence for the half-period observed by Lockyer [1926] as the He curve followed the hydrogen one and concluded that there exist real differences between the curves as well as that it is impossible to combine them as was done by Frédette [1925]. Instead he proposed that these variations are caused by pulsations of the primary with period of 126.6 days and due to creation of the lines in different depth of the stellar atmosphere.

Schiefer [1936] however pointed out that in order to produce the light variation which were observed by Guthnick and Prager [1918], a change of radius larger than radius of a typical B-type star would be necessary. Thus to satisfy the light-curve observations he suggested that the star is of very low density, is pear-shaped and with very extensive atmosphere, rotating off-centre of its small and ill-defined

photosphere with period of 126.6 d. In addition the star is also pulsating with the same period and the hydrogen absorption originates between the observer and the star itself, while the emission comes from atmosphere projecting beyond the photosphere perpendicular to the line of sight. The observed spectral variations are thought to be caused by rapid rotation and extensive atmosphere of both components.

To explain peculiarities in helium lines Hynek [1944] obtained new photographic spectra using 69inch ($\approx 1.75\,\mathrm{m}$) Perkins reflector with a two-prism spectrograph. Their main focus were a singlet line λ3965 and triplet lines λ4026 and λ4471. Velocity curve of line λ4026 was more consistent than the other two, however he discovered a sudden change of slope before and after crossing its zero value and between a behavior like a straight line. This also corresponds to phase interval when the lines are much sharper and more intense. Therefore, he suggested that a gas absorbing He 4026 and producing hydrogen lines and singlet He I λ3965 is present and moving in front of the light source in an opposite direction. The gas is also responsible for the observed sharpening of these lines as well as the peculiar behavior of velocity curve.

Calculation of rotational velocity of the primary was first done by Slettebak [1949], who used the broadening of the line He I λ4026, divided the disc of the star into 40 strips perpendicular to star's equator and compared the profile of the line with a narrow lined stars ϵ Cas and ι Her. While all other observed stars were compared with contours of a spherical star, to obtain rotational velocity of φ Per it was necessary to use a gravity darkened contour at critical velocity as the absorption lines were found to be much more broadened than lines of any other star. Its rotational velocity $v\sin(i)$ was found to be about 560 $\mathrm{km{\cdot}s^{-1}}$ while no other star was found to have the velocity higher than 450 $\mathrm{km{\cdot}s^{-1}}$.

2.1.2 Toward a consistent model

Kříž and Harmanec [1975] presented a general hypothesis that the nature of Be stars may come from their binary origin, where the stars are either going through a large-scale mass transfer or already underwent it. Polidan [1976] suggested that a binary consisting of a B-type star and a late-type (spectral type G or K, luminosity type IV or III) cool giant, which is filling its Roche lobe and transferring mass could be representative for the Be group of stars. However, no photometric observations were able to detect any infrared excess for a number of Be stars, despite the fact that a K-type star should provide about one third of the total flux in the K-band.

Peters [1976] introduced such model for a Be star HR 2142 of similar properties as φ Per which contained a K-type giant transferring mass to the Be star. She notes similarities in the spectra of these stars, namely strong Hα emission as well as lines Fe II, O I λ7774 & 8446 and Ca II triplet in infrared, all in emission. She however also notes that the shell absorption is observed in φ Per for most of the cycle, which is not so true for HR 2142.

Presence of a cool secondary was strongly opposed by Hendry [1976], who instead proposed that the φ Per system consists of a B1 primary and B3 secondary star, however the secondary is fainter and therefore invisible in the spectra [Hendry, 1975]. To obtain an orbital solution Hendry [1976] used 184 plates from

various observatories. The projected masses $M \sin^3(i)$ were found to be of about 14.3 and 7.8 $M_\odot$. This is also suggested by the complicated profile of H lines as it is composed of wide absorption from both stars, intense shell absorption from primary and weaker from secondary, double emission from both stars, wider and stronger from the primary.

Upon discovering a weak emission line He II λ4686 with radial velocities varying out of phase to those of other lines and with much higher velocity amplitudes Poeckert [1979] reclassified the secondary as a hot compact object. The model he presented contained a primary with mass of 29 $M_\odot$ orbited by a peculiar object of 3.8 $M_\odot$ surrounded by a dense circumstellar disk where the primary is losing mass and possibly transferring to the secondary. Poeckert [1981] also suggested that while Hendry [1976] found the He I lines to be double and contributed by each of the components, the measured line is in fact a sharp absorption originating in the disk as the high rotational velocity would broaden a photospheric line. Newer model based on 99 photographic and 14 Reticon spectra taken at the Dominion Astrophysical Observatory presents both components to be surrounded by their respective disks. The primary is surrounded by disk of ionized Fe spanning to about 50 $R_\odot$ based on the peak separation seen in spectra. Similarly, the radius of the disk around the compact secondary was estimated as 10 $R_\odot$. The rather complicated profile of Balmer lines led to believe that the outer disks made of neutral hydrogen reach radius of 70 and 50 $R_\odot$ respectively for primary and secondary. The estimate of the radius of the disk around the primary however was met with doubts as the V/R ratio for Balmer lines undergoes large cyclic variations that are thought to be caused by tidal effects and thus the disk must be much larger. The presence of ionized He implies high temperature of the secondary and so it is possible that it is a remnant of a previously more massive star that transferred most of its mass to the primary along with angular momentum which explains its high rotational velocity [Poeckert, 1981].

In an attempt to discover very short changes in spectra, Chalabaev and Maillard [1983] used the Mauna Kea 3.6m telescope to obtain 17 spectra in the red optical region and 4 spectra in the near infrared during three consecutive nights in 1981. They managed to find variations in the Hα profile from the first night in the span of 30 mins and the profile to be changing from night to night. During the other nights, however, no short-term variations were found nor were seen in the NIR region. Due to lack of necessary information they could only speculate about the nature of this event. Similar short-time variations in Hα were observed by Goraya [1984] on two nights in 1979.

Gies et al. [1993] used the 2.1 m telescope at Texas McDonald Observatory to obtain 26 spectra in red optical wavelengths between September 1985 and July 1988. They studied the secondary following emission part of the helium line λ6678 by subtracting the shallow photospheric absorption from spectra assuming a parabolic shape of the absorption component. This emission resolves into two components at quadratures, a stronger one with a large amplitude and a weaker with somewhat smaller semiamplitude, both antiphased to the velocity curve of the primary. These two components are separated by a central shell absorption which causes bias of the emission velocity measurements, which can explain the different amplitudes. Near superior conjunction of the primary they noticed a significant broadening of the emission peak, where its equivalent width increased

by a factor of 2. They suggested that this is due to the enhanced density region, which points towards the secondary, being most clearly visible by the observer at this phase and thus strengthening the emission.

A new detailed study of the system was carried out by Božić et al. [1995], who used all previous spectroscopic RV measurements and photometric observations with the addition of spectra they obtained. Firstly, using the 2 m telescope at Ondřejov Observatory with a Reticon detector they observed 24 red and 11 blue spectra and investigated photographic spectra that were gathered since 1972, they also obtained 6 ISIS spectra using 1.93 m telescope and 5 Aurelie spectra by 1.52 m telescope both located at Haute Provence Observatory. They argue that to measure radial velocities of Balmer lines and He I λ6678, it is necessary to use the wings of emission, which have high projected velocity. The reason for this is that the distribution of circumstellar matter is not axially symmetric, however, assuming Keplerian motion of the disk, these asymmetries mostly affect central low-velocity parts of the line. The wings of the line originate closer to the star where the Roche equipotential surface is nearly spherical.

In their investigations they found the measured radial velocities of emission wings of Balmer lines as well as metallic lines (mostly Fe II) to be following a sinusoidal curve of a similar low amplitude. From an orbital solution they found the eccentricity to be very small (0.06 ± 0.04) with varying longitudes of periastron. Thus they interpreted the eccentricity as being in fact equal to zero, as suggested from carrying out the Lucy-Sweeney test [Lucy and Sweeney, 1971]. While Gies et al. [1993] assumed that the He I λ6678 consists of two emission peaks, Božić et al. [1995] argued that the it is in fact a one double emission profile originating in the disk surrounding the secondary. Focusing on the wings of this emission than yields a sinusoidal curve. Their solution also yields a new estimate for the masses of the components, 16.4 and 1.7 $M_\odot$ for the primary and secondary, respectively.

Štefl et al. [2000] obtained a large number of new spectra, 82 of them in the red (6290–6720 Å) region coming from the 2m telescope at Ondřejov Observatory, 9 more spectra using the 2.2m telescope on Calar Alto and 12 from the 1.52m telescope of the Observatoire de Haute Provence both focusing either on Hα, He I λ5876 or Fe II λ5317. They also used the HEROS spectrograph installed on the 0.72 m Waltz reflector of the Landessternwarte Königstuhl and on the 1.23m telescope of the Calar Alto observatory to obtain 16 spectra in either blue (3450–5560 Å) or red (5820–8620 Å) region. They noticed the observed He lines can be separated into three categories depending whether their profile contains only a shell component (He I λ4713), a photospheric absorption (He I λ5048) or both the shell and emission (He I λ6678). To measure the intensity and radial velocity of He I λ6678 they subtracted the broad photospheric profile that was assumed to be unchanging. The RV curve of both peaks of the line showed a flat distributions where the magnitude of radial velocity did not decrease under 50 km·s^{-1} and -100 km·s^{-1} for the red and violet component respectively and the RV curve showed a discontinuity at phases 0.0 and 0.5.

This disagrees with the models of Gies et al. [1993] and Božić et al. [1995], which suggests that these lines originate in a thin envelope surrounding the secondary. Instead they present a model where the He I lines are produced in a part of the disk around the primary that is facing the hot secondary and is illuminated

and photoexcited by it. Further modeling of the He I λ6678 line profile done by Hummel and Štefl [2001] supports this explanation. Their model assumes a sphere centered on the secondary where photoionization of helium is possible, parts of the disc that happen to be located inside this sphere become sources of both emission and absorption due to the shell absorption of the primary. They however noticed that the shell absorption appeared sooner than predicted by Poeckert [1981] and suggested that this phase shift stems from differential rotation of the disk as well as finite excitation and recombination time of the He atoms. The disk emission radius was found to be of about 10 stellar radii of the primary, similar to the result of interferometric measurements by Quirrenbach et al. [1997].

2.2 UV spacecraft observations

Due to its high temperature the helium companion contributes mostly to the shorter wavelengths, therefore Thaller et al. [1995] studied spectra obtained by the International Ultraviolet Explorer (IUE) spacecraft. To find the values of RV they used a technique called Doppler tomography, where they shifted individual spectra of both primary and secondary to match the observed composite spectra. To do that they assumed a flux ratio of 0.14. While spectral lines of the primary were found to consist of photospheric lines with large rotational broadening, narrow shell absorption lines, disk emission lines of Fe IV and lines that imply presence of stellar wind by their P Cygni profile (C IV λ1550), the spectrum of the hot secondary shows many weak absorption lines of Fe V and an emission of the doublet C IV λ1550. Due to the presence of this peak doublet they suggested the presence of a strong wind from the secondary star, its absorption component having radial velocities of -230 km·s^{-1} and -480 km·s^{-1} for primary and secondary respectively. Their discoveries were a direct evidence that the companion is a small compact object, most probably a star stripped of its envelope by previous mass transfer as had been suggested by Poeckert [1981].

More UV spectra were later obtained by Gies et al. [1998] who used the Goddard High Resolution Spectrograph installed on the Hubble Space Telescope. The spectra were focusing on three different spectral regions, 3 were centered on λ1374, another 3 on λ1647 and one more on λ1735 Å. In the spectra weak narrow lines were found that showed large radial velocity changes with respect to orbital phase and so were associated with the secondary star. They then treated the broad lines from the primary as a varying continuum, used a high order spline to remove it and rescaled the resulting difference spectrum to flux ratio of 0.14. They also rescaled the spline to obtain an isolated spectrum of the primary and then used a cross-correlation method to measure radial velocities. A circular orbit with a period found by Božić et al. [1995] was assumed to derive the orbital solution. There appeared an indication that the orbital period might have lengthened as the epoch occured later than predicted by Božić et al. [1995]. Also the K-velocities were found to be smaller than those observed by both Poeckert [1981] and Božić et al. [1995] and thus the resulting masses lowered to $M \sin^3(i)$ of 8.91 and 1.09 $M_\odot$ for the primary and secondary, respectively.

Due to the discovery of these narrow lines coming from the secondary Gies et al. [1998] challenged the prediction by Poeckert [1981] that the secondary is rapidly rotating as well. Although it is possible that these lines originate in the

disk surrounding the secondary, synthetic spectra of a slow rotator sufficiently matched the observed spectrum. In addition, rotationally broadened lines that follow the velocity curve of the secondary were not found. It was also noticed that there appeared strong narrow lines in one of the 1647 Å spectra, which was made at the orbital phase 0.958 and the lines were attributed to the element Fe IV. Their presence indicate additional material absorbing the light of the primary. As the sightline at this phase misses the Roche lobe of the secondary and at the same time the lines are of much smaller radial velocity than the secondary, Gies et al. [1998] argued that the source must lie in the disk of the primary. There appears to be a confined location where the gas that the primary is observed through at this phase is heated by the much hotter secondary by either its EUV radiation or stellar wind and it is possible for the Fe IV lines to form.

2.3 Photometry

The very first observations of φ Per were done by Guthnick and Prager [1918] at the Berlin-Babelsberg Observatory using 0.3 m refractor and diode photometer. The same telescope was later used by Güssow [1930] with photomultiplier installed. As no standardized photometric system existed at the time, their measurements are not calibrated. This is also the case for observations done by Güssow [1930] at Steward Observatory. Luckily, in their work they used well-observed comparison stars and Božić et al. [1995] were able to transform their results to the standard UBV system.

Dapergolas et al. [1981] observed the star at the Loiano 0.6 m telescope in Bologna. As a comparison star 2 Per was chosen and HD 11151 as a check star. Data of one night were averaged and from the four measured nights the star's brightening was noticed, mainly in the U filter.

Brown [1992] observed on 34 nights in total at the Glenlea Astronomical Observatory in Canada. A Schmidt-Cassegrain telescope of 0.35 m was used equipped with B and V filters. For transformation into Johnson's system every night three to five cycles were made consisting of 4 Per serving as comparison star and 2 Per and 51 And as check stars. In the analysis data that were later published by Božić et al. [1995] as well as previously unpublished data by Halbedel [1986] were used. While the data clearly showed that the brightness undergoes some long-term variation, after subtracting these changes and plotted with respect to orbital phase, three points coming from different cycles lying between phases 0.43 to 0.52 were found to be about 0.1 mag dimmer and similarly another two points near phase 0.1 suggesting presence of minima. However, as there were only four cycles that showed these minima, Brown [1992] suggested their cause not to be due to eclipses but instead with either periodic variations in opacity of surrounding gas or presence of a gas stream from the secondary to the primary. The presence of these sudden minima was later disproved by Božić et al. [1995], who found that they are not associated to specific phases and instead proposed the star either undergoes some other type of light variability or rare stages of rapid changes.

Božić et al. [1995] described secular changes in brightness and colour of φ Per as mild, where the star had been slowly dimming while becoming bluer in $B-V$ and redder in $U-B$. At the same time the Balmer emission in the spectra was

fading as well, which is the case of Be stars with 'positive correlation' between the emission strength, and the star's luminosity as devised by Harmanec [1983].

2.4 Interferometry

The first interferometric observations were carried out by Quirrenbach et al. [1997] using a double-telescope interferometer located on Mt. Wilson, USA. In total, 66 measurements were made between 1991 and 1992 on 6 baselines of different length, spanning from 4.2 to 23.6 m. To resolve the diameter of the circumstellar disk, they fitted their data taken in Hα region and used an elliptical Gaussian fit as the circular would not be accurate and this resulted to the value of 2.67 mas. The disk appeared as quite elongated, which could be interpreted as being seen nearly edge-on, which led them to estimate the minimal inclination to be 63°, consistent with an assumption of $i > 65°$ by Božić et al. [1995]. As the disk surrounding the star polarizes passing light, they also used a 0.9m telescope with an optical spectropolarimeter at Pine Bluff Observatory. They observed on 14 nights from 1989 to 1993. With addition from photometric IR excess, the polarization can also be used to calculate the inclination, as while the IR excess depends solely on the density of the disk, polarization apart from density diminishes when the star is viewed pole-on and is maximal when viewed edge-on. Therefore inclination can be estimated by comparing the star's intrinsic polarization to the maximum polarization. This approach however does assume that the disk is optically thin for the IR excess to be invariant to inclination, which is not necessarily the case for Be stars whose disks are most likely thick to electron scattering. Regardless of this limitation it still can be used as an estimate for inclination. Consistently with interferometric observations, for the elongated disk of φ Per the intrinsic polarization was nearly equal to maximal polarization.

During last months of 2004, Tycner et al. [2006] observed φ Per using the Navy Prototype Optical Interferometer equipped with narrow-band filters focusing on the Hα line. Each observation was recorded every 2 ms for 30 s and the resulting squared visibilities (V^2) were averaged over 1s intervals. Although three stations were used for observations, due to simultaneous observations with another Be star γ Cas it was not possible to combine all three beams and thus the values of other observables, namely closure phase and triple product, could not be measured. In their modeling the total V^2consists of visibilities of the photosphere and the disk with contribution from the photosphere in the Hα region taken into account. As the primary was not well resolved even at their longest baselines, they ignored the effects of their rapid rotation and only assumed the diameter from photometric relations [Barnes et al., 1978], which equals to 0.39 mas in case φ Per. They considered three possible models of brightness distribution in the interstellar medium, a uniform disk, a uniform ring, or a Gaussian distribution. The best describing model for the γ Cas system was the Gaussian, while for the φ Per system, they were unable to disprove the other two. However, they were able to constrain the photospheric contribution from spectroscopic observations, which was very consistent with the Gaussian model and thus they also concluded this one to provide the best description of the system. The results from this model also agreed well with values published by Quirrenbach et al. [1997].

Gies et al. [2007] observed φ Per in the near infrared K-band for four nights in

October 2003 with the CHARA Array at Mt. Wilson Observatory. On one night a baseline of 249 m was used while on the rest they used a 111m baseline. In their modeling they also included the secondary companion. They noted a lower size of the disk compared to previous studies (2.30(8) mas and 2.89(9) mas by Tycner et al. [2006]). This they attributed to larger opacity in Hα region that was used in those studies as while the Hα is mainly dependent on the density of neutral hydrogen, the K' emission is produced by free-free processes in the ionized gas. Similarly, more measurements were made by Touhami et al. [2013] by the same instrument in 2008 and 2009, though the baseline used spanned from about 60 to 325 m and obtaining a result not very different from Gies et al. [2007]. However, they note that the ratio of the radii based on Hα and K-band observations is much smaller than in other stars they surveyed, where the Hα region can be several times larger. This, they explain, is the effect of tidal forces from the motion of the secondary that truncate the size of the disk.

The hot secondary was for the first time directly detected by Mourard et al. [2015], who during the years 2011 to 2013 used the CHARA Array. In total they obtained 18 observations, out of which 10 were done using the MIRC instrument operating in 6-telescope mode in the near-infrared H-band, for the 8 remaining the VEGA instrument was used in the 4T mode in visible range. From the interferometric observations they were able to determine a visual orbit of the secondary and with addition of RV measurements in Hα region and by the HST they found a new orbital solution with a revised orbital period of $126\overset{\mathrm{d}}{.}6982(35)$ (vs. $126\overset{\mathrm{d}}{.}6731(71)$ by Božić et al. [1995]). They constructed a kinematic model of the disk from Hα observations and found that the disk should follow a nearly Keplerian orbit and its FWHM to be 3.4 ± 1.7 and 5.9 ± 1.7 times larger than the diameter of the primary for continuum and Hα respectively.

They also derived the distance of the system to be (186 ± 3) pc, which is also very close to a nearby α Per cluster with distance of 177 pc. The φ Per system shares similar proper motion and systemic velocity to the cluster as well and thus Mourard et al. [2015] suggested φ Per to by an outlying member of the cluster. If that were indeed the case, φ Per and the cluster should share the same age, which was found to be 52 Myr.

2.5 Numerical simulations

To simulate the evolution of the envelope-stripped companion, Schootemeijer et al. [2018] used the MESA evolutionary code with modeling of mass transfer between the components. They found that in order to reach the values observed today, the most probable initial mass of the present subdwarf had to be (7.2 ± 0.4) $M_\odot$, and of the now Be star 3.8 ± 0.4 $M_\odot$. Before the onset of the mass transfer they found that the system had to be detached with orbital period of about 16 d and the beginning of mass transfer started with an expansion of the more massive star as it left the Main Sequence (the so-called case B mass transfer). During the mass transfer most of the material remained within the system, i.e. the best model was described by a nearly conservative transfer. From these calculations they also derived the age of the system to be (57 ± 9) Myr, in accord with the age of the α Per cluster, as proposed by Mourard et al. [2015].

From these simulation they suggested that the companion is currently in a

short helium shell burning phase due to its high luminosity compared to He core burning stars by an order of magnitude. This also allowed them to predict that while the companion will likely turn into a CO white dwarf, the massive Be star is on its way to end its life as a core-collapse supernova. However, due to expansion at later stages, it will probably fill its Roche lobe and start a reverse mass transfer and in the end merging of both stars is possible.

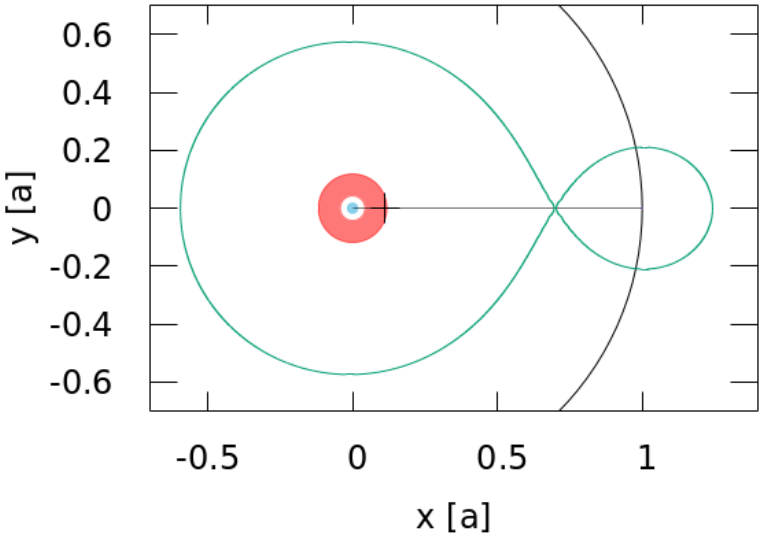

Figure 2.1: Model of the φ Per system as published by Mourard et al. [2015] with the disc (red) of size 5.9 stellar radius, the cross denoting the barycentre of the system and the Roche lobe is shown in green.

Source	Epoch [RJD]	Nr. of obs.	Lines meas.	Stat.
Campbell [1902]	14 537–15 700	5	H$\gamma^{(s)}$	Li
Ludendorff [1910]	16 058–18 758	121	H$\gamma^{(s)}$	Po
Cannon [1911]	18 278–19 301	129	Hβ–ϵ, Ca K	DO
Ludendorff [1912]	18 940–19 034	14	H$\gamma^{(s)}$	Po
Jordan [1916]	18 152–9 399	112/97	Hγ–$\epsilon^{(a)}$/Hβ–$\delta^{(e)}$	Al
Frédette [1925]	19 795–30 379	31	Hβ–$\zeta^{(s)}$	Dl
Dustheimer [1939]	19 331–24 503	162	Hβ–$\iota^{(s,e)}$	Mi
Schiefer [1936]	25 090–25 278	32/32	Hβ–$\zeta^{(s)}$/Hβ–$\delta^{(e)}$	AA
Hynek [1944]		116	Hγ	Pe
Miczaika [1950]	32 805–33 389	34/33/33	Hγ,δ/Hϵ/H$\zeta^{(s)}$	Hb
Abt and Levy [1978]	41 881–42 778	21	H/He I$^{(a)}$	KP
Poeckert [1981]	42 762–43 855	32/32	H$\beta^{(e;s)}$/He I$^{(a;s)}$	DA
		31/32	He II/Fe II$^{(e)}$	DA
Jarad et al. [1989]	45 696–46 068	23	He I$^{(a)}$	SA
Gies et al. [1993]	46 447–47 367	20/26	Hα/He I$^{(e)}$	MD
Singh et al. [1994]	40 093–46 726	23/53/53	Hβ/Hγ,δ/He I	Ok
Thaller et al. [1995]	43 763–45 239	16	UV	IUE
Božić et al. [1995]	16 059–18 974	26	H$\alpha^{(e)}$	Po
	41 623–48 653	78/78	Fe II$^{(s)}$/H$\beta^{(e)}$	On
		56	Hζ–$\iota^{(a)}$	On
	48 883–49 613	25/35/24	Hα/M$^{(e;a)}$/He I$^{(e)}$	On
	46 693–46 696	6	Hα/He I$^{(e)}$	HP
	49 002–49 008	2/3	He I$^{(e)}$/M$^{(e;a)}$	HP
Gies et al. [1998]	50 023–50 372	12	Cr V, Fe V	HST
Štefl et al. [2000]	49 206–51 471	82/87	Hα/He I$^{(e)}$	On
	49 298–49 708	4/2/3	Hα/Fe II/He I	CA
	49 655–50 076	5/3/4	Hα/Fe II/He I	HP
	50 826–51 091	16	Hα,$\beta^{(e)}$	H
Mourard et al. [2015]	51 056–54 024	22	H$\alpha^{(e)}$	KP
	50 709–56 666	52	H$\alpha^{(e)}$	Be

Table 2.1: List of spectroscopic observations

Note: whenever given, the letter after the name of a line corresponds to whether the line was measured in its shell profile (s), as a broad photospheric absorption line (a) or broad disk emission line (e); column 'Stat.' represents different stations:
Li... Lick Ob., Mills spectrograph; Po... Potsdam Ob., 0.32 m; Do... Dominion Ob. Ottawa; Al... Allegheny Ob.; Mi... Michigan Ob., 0.95 m; AA... Ann Arbor, 0.95 m; Pe... Perkins Ob. 1.75 m; Hb... Heidelberg, 0.72 m; KP... Kitt Peak N. Ob., 2.1 m; DA... Dominion Astroph. Ob.; SA... St. Andrews Ob., 0.5 m; MD... McDonald Ob., 2.1 m; Ok... Okayama Astrophysical Ob., 1.88 m; Ok... Okayama Astrop. Ob. 1.88 m reflec., var. emul.; IUE... International Ultraviolet Explorer; HST... Hubble Space Telescope; On... Ondřejov Ob., 2 m; CA... Calar Alto Ob., 2.2 m; HP... Observatoire de Haute Provence, 1.52 m; H... HEROS spectrograph; Be... Be Star Spectra database [Neiner et al., 2011], various observers

3. Analysis of spectra

3.1 Overview

Using the 2m Perek telescope located at Ondřejov Observatory in total 89 spectra in the red region (approx. 6260–6730 Å) were obtained since 2001 by a number of observers. Out of these 31 were secured between the years 2001 and 2005, 7 in 2010 and 2011, and the remaining 51 between 2014 and 2017.

Additionally I used the Be Star Spectral database[1] (BeSS) [Neiner et al., 2011] where professionals as well as amateur astronomers upload their observed spectra of a large number of Be stars. In total I was able to find 150 spectra in the Hα region obtained since 1997 with spectral resolution higher than 10 000. As many of these spectra were of echelle-type spanning a large interval of wavelengths, I was able to find 58 of them that included the blue Balmer line Hβ as well.

Furthermore I reviewed about a hundred of old (measured in the beginning of the twentieth century) spectra from Potsdam Observatory. These contained the line Hγ in the violet spectral region. The journal of all analyzed spectra can be found in Table 3.1.

The most prominent objects in the red spectra are the Balmer line Hα and He I λ6678. Unfortunately the strong emission of Hα caused an over-saturation in 13 Ondřejov spectra and so I was unable to use these for the analysis of the Hα profile. Both these lines consist of emission as well as absorption component blending together, thus showing a rather peculiar shape which is evolving in time.

For the purpose of visualising the spectra I created a `python3` package[2]. Spectral measurements are first ordered in time and then each spectrum is coloured based on the observed intensity at wavelengths in the vicinity of a particular spectral line. The results can be seen in Fig. 3.1 and 3.2 for line Hα and Hβ, respectively.

The orbital phase, further denoted as φ, of an observation performed at time T was calculated as

$$\varphi = \frac{(T - T_0) \mod P}{P}. \tag{3.1}$$

Epoch [RJD]	Range λ[Å]	#Spectra	Observatory	Featured lines
16000–19100	4000–4800	101	Po	Hγ
50700–59200	6500–6700	151	BeSS	Hα
		(51)	BeSS	He I λ6678
50700–59200	4800–4950	58	BeSS	Hβ
52200–58000	6400–6900	89	On	He I λ6678
		(76)	On	Hα

Table 3.1: List of spectra analyzed in this work.
Note: #Spectra in parentheses represent a subset of the above record. The Observatory column contains the following abbreviations: Po – Potsdam Observatory, BeSS – BeSS spectral database, On - Ondřejov Observatory.

[1] `http://basebe.obspm.fr/basebe/`
[2] `https://sirrah.troja.mff.cuni.cz/~jonak/python/dynspe/dynspe.html`

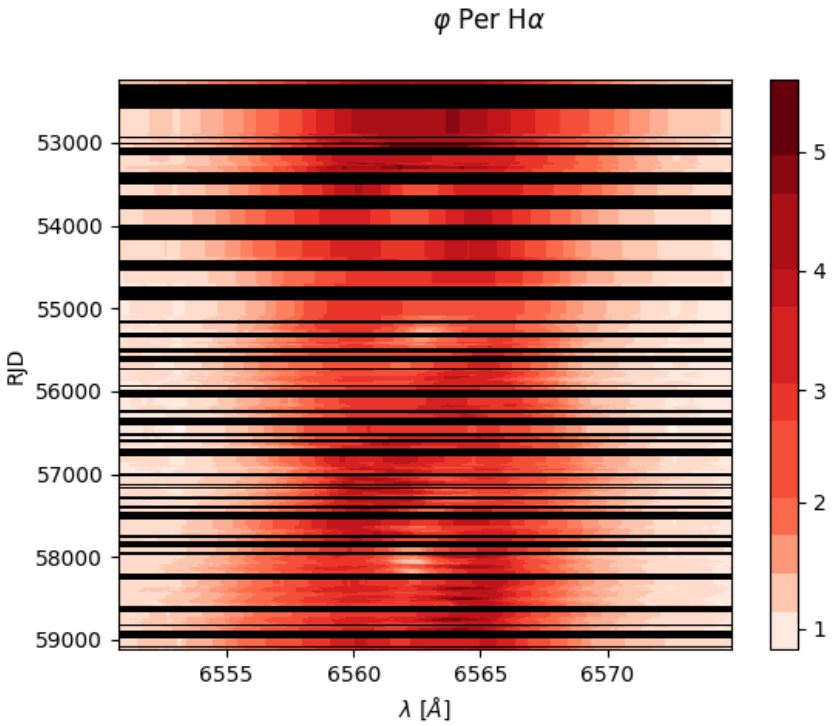

Figure 3.1: Trailed spectrum of Hα – spectral profile of the line (wavelength is on the horizontal axis) are ordered in time (vertical axis) and the measured intensity of the segments is represented by a colour-scale on the right.

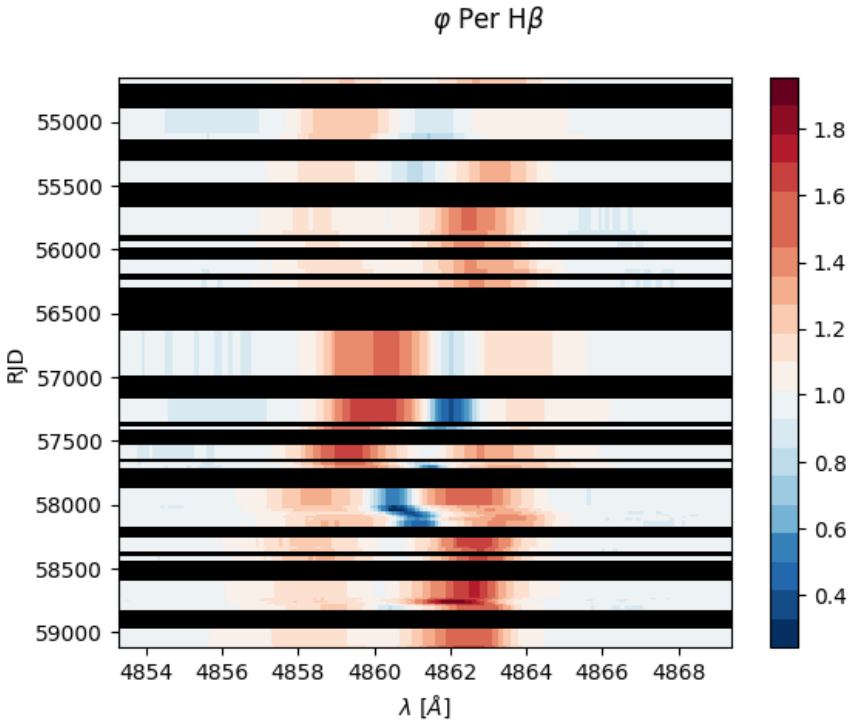

Figure 3.2: Trailed spectrum of Hβ – the same as Fig 3.1.

For the processing of the Ondřejov spectra I used the DOS-based program SPEFO (described by Horn et al. [1996] and was further developed by J. Krpata). There exists a new java-based rework of this program, called reSPEFO[3], currently being developed by A. Harmanec (a detailed description can be found in Appendix C of the work by Harmanec et al. [2020]). I used its version 1.0.7 while working with BeSS data and pre-release of version 2 for Potsdam spectra.

There do not appear any significant differences when working with either of these programs that would affect the data processing and I shall address them in general as SPEFO.

The first step of processing was to normalize the spectra. This I did using a selection of points lying on the stellar continuum, where there are no lines present. The program then forms a Hermit polynomial passing through these points and divides the spectrum by it.

3.2 Measuring radial velocities

SPEFO allows one to manually measure radial velocities using the oscilloscopic method, where the line is compared with its flipped image. This allows the user to manually select the point where this mirror image is best correlated with the direct one and the shift necessary to do so marks the difference between the actual and laboratory position. This process is described in more detail by Wolf et al. [2021].

To remove a zero-point error of the spectrograph I first measured a number of selected unblended atmospheric lines, produced by H_2O and O_2 molecules in the air. In each Ondřejov spectrum I found at least ten such lines, for most of the BeSS spectra I was able to find only about five such lines as these spectra cover a shorter wavelength range. All velocities of the stellar lines were then corrected for the difference between the mean radial velocity of atmospheric lines and calculated heliocentric RV correction.

On the other hand, there are no atmospheric lines present in the blue spectral region. Luckily, as every BeSS blue spectrum had been measured using an echelle spectrograph, there was a corresponding red spectrum available. This allowed me to use the correction from red atmospheric lines for the blue BeSS spectra as well.

Hα and Hβ

The presence of a moving interstellar disc makes stellar lines asymmetrical. Thus the measured radial velocity varies for different elements of the line. Nevertheless, when measuring the velocity of Hα and Hβ I followed the suggestion by Božić et al. [1995] and focused on the wings of the lines. Each line was measured three times and the error of radial velocity was estimated from root-mean-square error of these three measurements.

Figure 3.3 shows the star underwent secular changes where the whole curve was shifted in radial velocity. It seems as if the line was quite rapidly red-shifted to an average value of about 15–20 $\mathrm{km \cdot s^{-1}}$ during the years 2004–2005 and 2013–2016. Between these events there seem to be a slightly longer stage where the line was blue-shifted instead to an average value of some 20–40 $\mathrm{km \cdot s^{-1}}$.

[3] `https://astro.troja.mff.cuni.cz/projects/respefo/`

To study purely the orbital motion I attempted to remove these trends. I calculated normal points on the curve averaging by three periods (≈ 380 d) using the program HEC23 and afterwards fitted these normal points using the program HEC36[4] by Hermit polynomial.

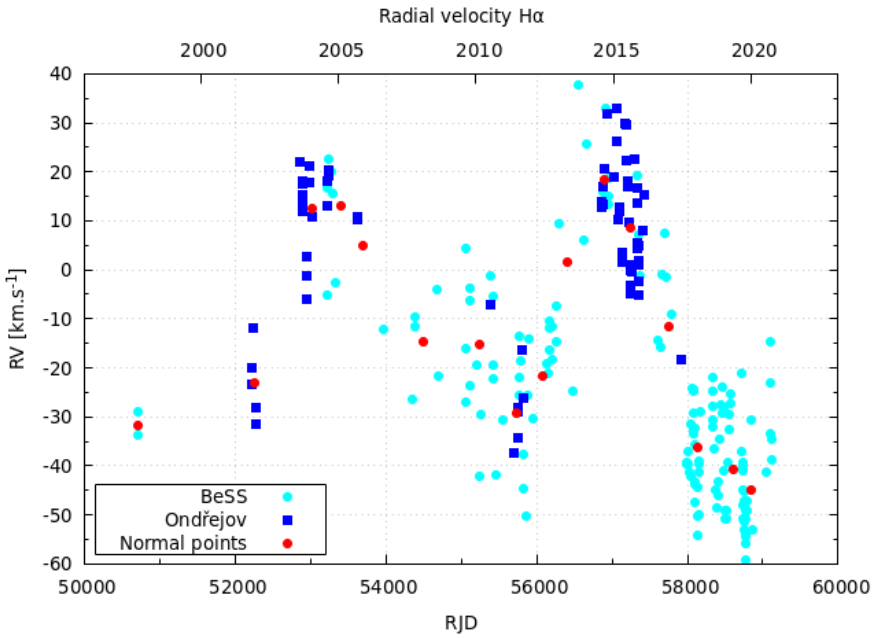

Figure 3.3: Radial velocity of Hα emission wings with calculated normal points. The spectra are distinguished by their source: blue squares represent Ondřejov spectra while cyan circles correspond to the spectra from the BeSS database. The measured uncertainties are of the order of the size of each datapoint.

Hγ

I reviewed spectra from Potsdam Observatory secured between the years 1902 and 1911. These were obtained in the violet spectral regions (4000–4800 Å). Similarly to the line Hβ the emission of Hγ is narrower than the underlying photospheric absorption giving the line a complicated emission-absorption profile.

[4] `https://astro.troja.mff.cuni.cz/ftp/hec/HEC36/`

3.3 Deriving a new value of ephemeris

From the measured radial velocities I calculated the orbital elements of the primary star. However, as shown in Fig. 3.3, the mean velocity is changing in time. In order to find a solution I used the normal points calculated by HEC23 as 'seed-points' – observations were clustered into common datasets based on the closest seed-point in time. In total this process resulted in 16 distinct datasets, however the two measurements from the year 1997 (RJD 50 709) were merged into the following dataset.

As the lines were each measured in SPEFO several times, the measurements provide some estimate of the measured error σ_j^{stat}. For the calculation I assumed the corresponding weight w of a measurement as

$$w_j = \left(\frac{0.5\,\mathrm{km{\cdot}s^{-1}}}{\min(0.5\,\mathrm{km{\cdot}s^{-1}}, \sigma_j^{\mathrm{stat}})} \right)^2 ,$$

where measurements with $\sigma_j^{\mathrm{stat}} < 0.5\mathrm{km{\cdot}s^{-1}}$ were of weight 1. This arbitrary value was chosen due to the complicated emission profile of the lines.

The solution was calculated using the pascal code SPEL [Horn et al., 1996]. In the calculation the fitted parameters were period P, epoch HJD_0, velocity amplitude of the primary K and systemic velocity of each dataset γ, while due to the assumption of a circular orbit eccentricity was fixed at 0. I first computed a solution from the Ondřejov and BeSS spectra only. To get a more robust solution I included the radial velocities of the primary star measured by Božić et al. [1995] and of the secondary published by Gies et al. [1998] and Mourard et al. [2015]. This allowed me to solve for the velocity amplitude of the secondary K_2 and I ran the program once again. The results of both calculations can be seen in Table 3.2 and Figure 3.4. From the values of period and velocity amplitudes, it is possible to determine the projected semi-major axes for the circular orbit $a_1 \sin(i)$ and $a_2 \sin(i)$ as

$$a_j \sin i = \frac{P}{2\pi} K_j \,, \tag{3.2}$$

as well as the masses $M_1 \sin^3(i)$ $M_2 \sin^3(i)$

$$M_j \sin^3(i) = \frac{1}{2\pi G} K_{3-j} (K_1 + K_2)^2 P \,. \tag{3.3}$$

The error is estimated using the formula for propagation of uncertainties

$$\sigma(f(x_{1\ldots j})) = \sqrt{\sum_{i=1}^{j} \left| \frac{\partial f}{\partial x_i} \sigma(x_i) \right|^2} \,. \tag{3.4}$$

		Solution 1		Solution 2	
Parameter		Value	Error	Value	Error
P	[d]	126.635	0.060	126.6446	0.0069
HJD_0		56930.49	0.95	56929.72	0.67
K_1	[km·s^{-1}]	11.19	0.55	11.16	0.43
K_2	[km·s^{-1}]			89.34	1.74
γ_1	[km·s^{-1}]			-7.53	0.85
γ_2				-8.31	0.53
γ_3				-9.83	1.38
γ_4				-2.67	2.25
γ_5		-30.68	1.97	-30.73	2.20
γ_6		9.23	1.60	9.32	1.78
γ_7		11.18	2.06	10.90	2.30
γ_8		3.24	2.75	2.83	3.07
γ_9		-14.60	2.65	-14.54	2.95
γ_{10}		-13.62	2.07	-13.69	2.31
γ_{11}		-29.63	1.64	-29.61	1.83
γ_{12}		-22.53	2.82	-22.51	3.15
γ_{13}		-2.16	2.43	-2.48	2.71
γ_{14}		20.25	1.26	20.26	1.41
γ_{15}		9.89	0.88	10.04	0.98
γ_{16}		-9.48	0.20	-9.65	2.50
γ_{17}		-37.17	0.08	-37.15	1.02
γ_{18}		-37.53	0.10	-37.51	1.28
γ_{19}	[km·s^{-1}]	-41.94	0.10	-41.84	1.22
$M_1 \sin^3(i)$	[$\mathrm{M}_\odot$]			11.84	0.64
$a_1 \sin(i)$	[$\mathrm{R}_\odot$]			27.9	1.1
$M_2 \sin^3(i)$	[$\mathrm{M}_\odot$]			1.48	0.09
$a_2 \sin(i)$	[$\mathrm{R}_\odot$]			223.6	4.4

Table 3.2: Best-fit parameters of ephemeris. Solution 1 consists only of Hα velocities measured by the author. Solution 2 includes measurements of Hγ (dataset 1), data from Božić et al. [1995] (dataset 2) and velocities of the secondary from IUE [Thaller et al., 1995, Mourard et al., 2015] (dataset 3) and HST [Gies et al., 1998] (dataset 4).

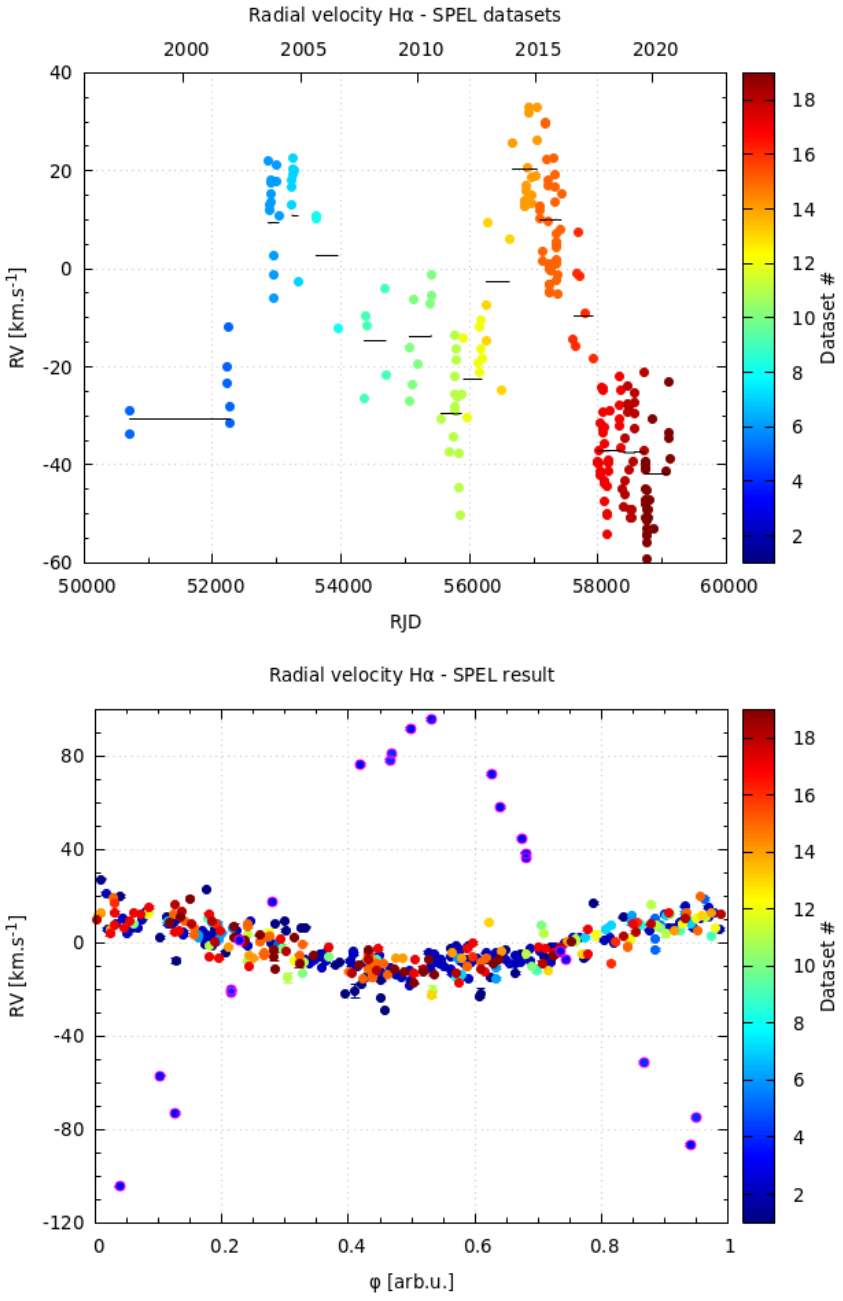

Figure 3.4: Finding ephemeris in SPEL. The datasets are colour-coded in the time diagram (top) and this colour is retained in the resulting phase diagram (bottom). Values for the secondary star are distinguished by a pink outline. In addition the γ-velocity is plotted as a line for each dataset above 4.

3.4 Line intensity

Another parameter that can be measured for a spectral line is its intensity relative to the continuum. Lines (or rather their components) may be then divided to two categories, absorption and emission lines. Naturally, if there are multiple sources of photons where the lines can form, it is possible to detect lines that consist of both an absorption as well as an emission component.

The total area of a line is called its equivalent width and represents total flux that is contained in the line. The equivalent width of a line in a normalized spectrum is given by

$$EW = \int_{\text{line}} (1 - F_\lambda)\, \mathrm{d}\lambda. \tag{3.5}$$

As can be clearly seen from this equation, EW of an emission line is negative.

3.4.1 Hα and Hβ

A common Balmer line profile of a Be star that is viewed edge-on consists of two double emission peaks, labeled as red-shifted (R) and blue-shifted (V), separated by an absorption shell core with a wide underlying broad absorption from the rotating star. Howeverin many cases the R and V 'peaks' are not clearly defined. Therefore I calculated V/R only for spectra with clearly distinguished peaks.

The equivalent width of Hα (can be seen in top part ofFig. 3.6) as well as its intensity underwent secular changes as well. The total emission in Hα most likely reached its maximum in the early 2000s and by 2010 it rapidly decreased to less than half of its previous value. Since then the emission has been steadily increasing.

The V/R ratio of Hα has developed in a yet different mode as the plot shows an appearance of a cycle about 5 years long. In addition, the amplitude of this effect has been increasing over time.

It is harder to make conclusions from the line Hβ separately, as these blue observations are more sparse than the red ones. In addition, the profile of Hβ has a strong absorption core reaching below the continuum at some times. Thus the line has a mixed absorption-emission profile which poses difficulties in interpreting its EW. However, comparing the long-term variations of V/R and central intensity between the two lines, the intensity of both of the lines have been rising since 2010, although Hβ is much weaker than Hα. V/R changes are evident in both cases with nearly identical values.

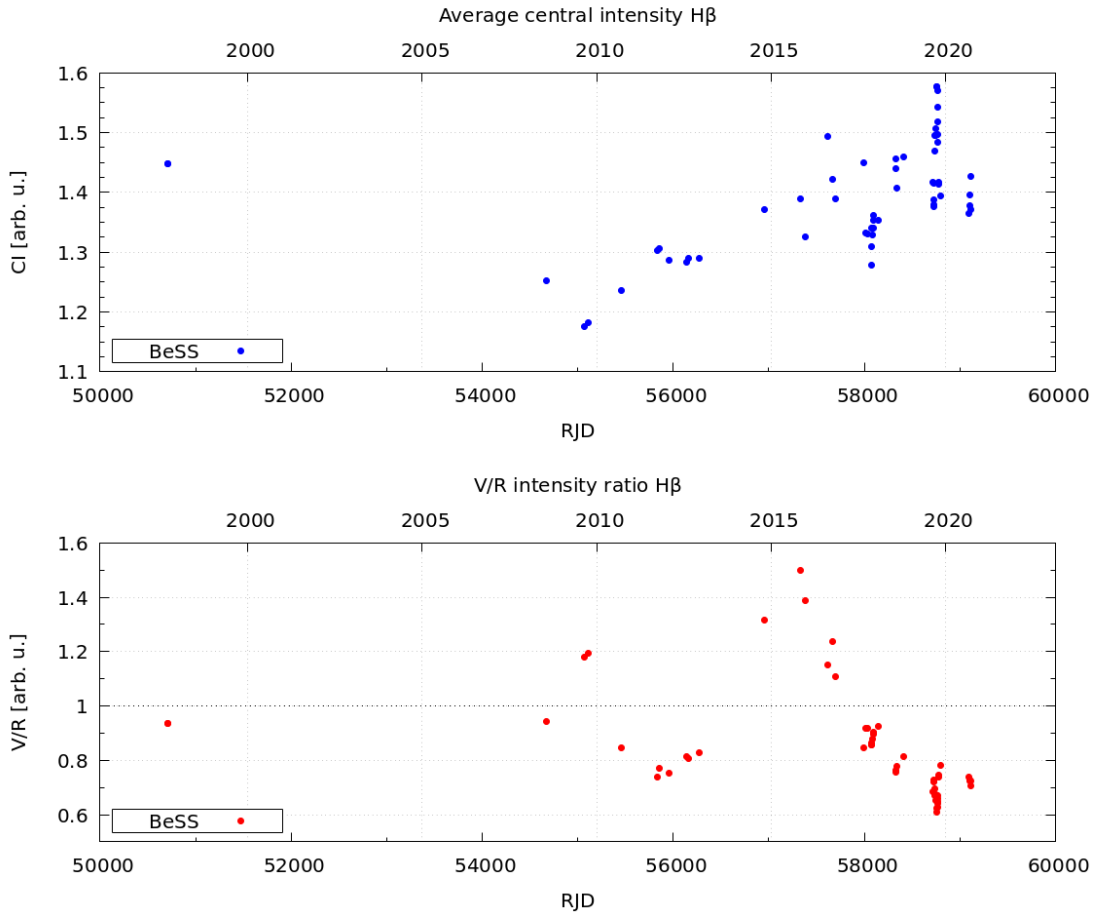

Figure 3.5: Secular changes of central intensity (top) and V/R ratio (bottom) of Hβ line.

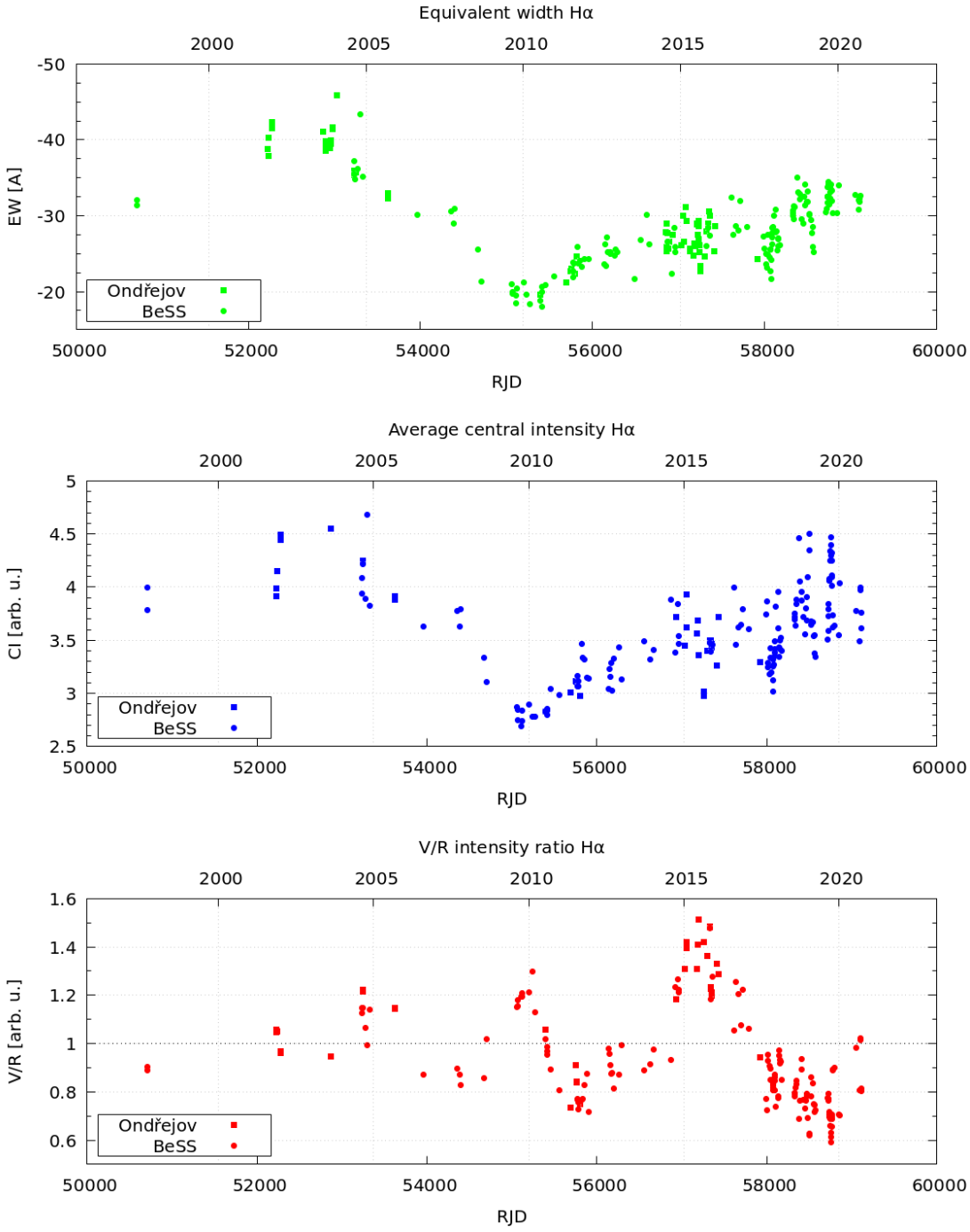

Figure 3.6: Secular changes of equivalent width (top), central intensity (centre) and V/R ratio (bottom) of Hα line.

3.4.2 He I λ6678

The emission component of the He I λ6678 line is much weaker and much narrower than the Balmer lines Hα and Hβ. This makes the absorption much more prominent and hiding some of the emission.

In order to circumvent this issue and to promote the emission in this line I took advantage of an interpolation tool for creating synthetic spectra `PYTERPOL` [Nemravová et al., 2016] and generated synthetic spectrum in the vicinity of He I λ6678 of a star with parameters corresponding to measurements of the primary [Gies et al., 1998, Mourard et al., 2015], namely $T_{\rm eff}$= 29.3 kK, $\log g = 4.07$ and $v_{\rm rot} = 410\,{\rm km{\cdot}s^{-1}}$.

I calculated radial velocity of the primary $v_{\rm rad}$ for all spectra containing the He λ6678 line as

$$v_{\rm rad} = K\cos(2\pi\varphi), \tag{3.6}$$

where the values of the semi-amplitude K and the ephemeris to calculate orbital phase are listed in Tab. 3.2.

I created a simple python code that interpolates the synthetic spectrum to the wavelength points of the signal and divides the spectrum of He I λ6678 by the synthetic spectrum. An example of such method can be seen in Fig. 3.7.

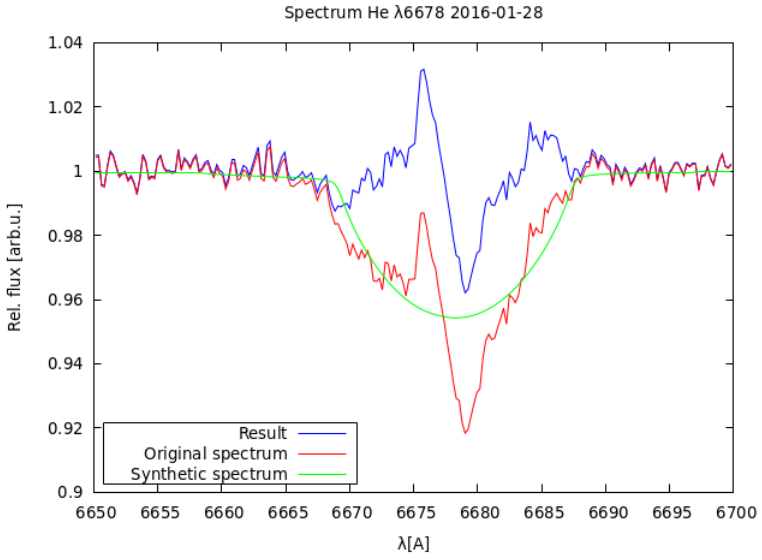

Figure 3.7: Removing underlying absorption in the line He I λ6678. The original spectrum (red) is divided by the synthetic spectrum (green) resulting in the spectrum in blue colour.

Using these divided spectra I found the highest intensity left and right from the line's laboratory wavelength and identified them as V and R peak and calculated the V/R ratio for this line. I then compared the results to the V/R variation of Hα, which can be seen in Fig. 3.8. This plot implies that the long-term V/R variation of the He and Hα line is correlated, both lines appear more red at near same periods of time. If this were indeed the case, it favours the model proposed by Gies et al. [2007] with a hot spot in the disc illuminated by the secondary.

The phase diagram of these variations suggests that if $V/R < 1$, it reaches its extreme at $\varphi \approx 0.25$ and as it reaches unity. it remains constant for the rest of

the cycle. The inverse is true if $V/R > 1$ where remains unity for the first half of the cycle and then it reaches its maximum at $\varphi \approx 0.75$.

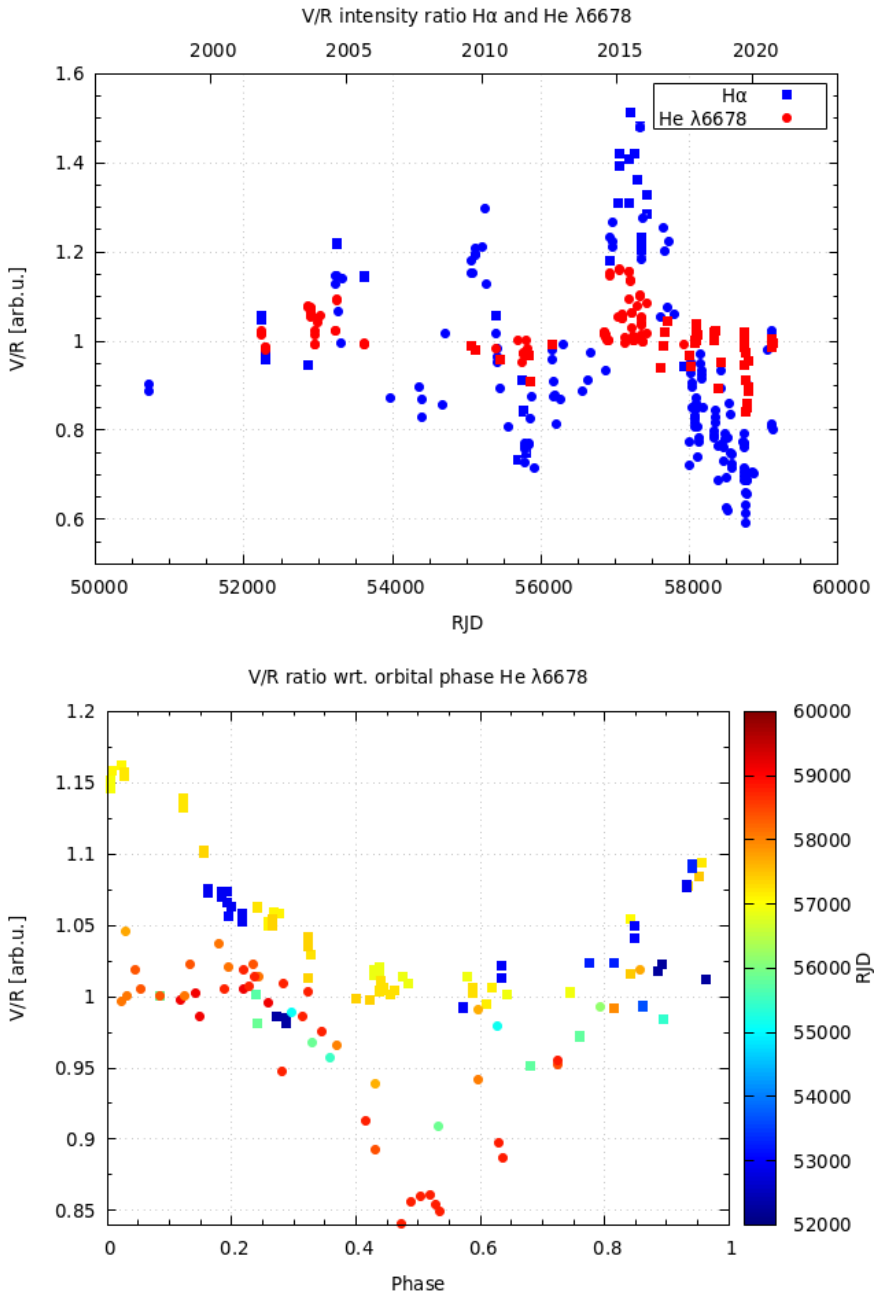

Figure 3.8: V/R ratio of line He I λ6678 compared to Hα in time (top) and its value with respect to orbital phase (bottom). In both graphs circular points correspond to data from BeSS database while squares come from Ondřejov. The phase diagram denotes the time of the measurement by the colour of the point as indicated by the colourbar with the oldest data being blue and the most recent ones being red.

4. Modeling of φ Per

To determine the properties of both the star as well as the surrounding disc, it is necessary to construct a sufficiently complex physical model of radiation transfer and, at the same time, to take into account different types of measurements as they provide different constrains on the model.

4.1 Physical model

As described by its authors Budaj and Richards [2004] 'program `SHELLSPEC` is designed to solve simple radiative transfer along the line of sight in moving media'. Assuming the local thermodynamic equilibrium and using the long characteristics method the program calculates synthetic images of objects defined on a 3D grid as a 2D projection of the monochromatic flux. The code also includes a number of opacity sources, including bound-bound (along with the natural, Stark and Van der Waals broadening of the lines), bound-free and free-free interaction as well as simplified Thomson and Rayleigh scattering on neutral hydrogen.

The program utilizes the so-called 'body-frozen' coordinates co-rotating with the binary's orbit. However, the transfer is calculated along the observer's line of sight which has the same center as the body-frozen grid and is rotated so that the z-axis points toward the observer. These grids are defined by their ranges in the (x, y, z) directions and intervals of grid-points (in $\mathrm{R}_\odot$ units). Both grids, the body-frozen and the line-of-sight, can have an additional sub-grid with own range and number of grid-points.

The code contains a number of predefined geometrical objects:

- non-transparent objects representing star-like objects which are defined by their position (x, y, z) in the body-frozen grid, radius R, effective temperature T and rotational velocity v_{rot}.
  - `STAR`: a central nontransparent object rotating as a solid body. It can have its own synthetic spectrum. It is designed for the brighter of the stars. It can be detached or filling its Roche lobe. In addition to the parameters listed it is defined by its mass M^{star}.
  - `COMPANION`: an object similar to the previous one but designed for the fainter star. Its mass is derived from the mass ratio q.
- semi-transparent objects located at some specific position (x, y, z) and moving with velocity (v_x, v_y, v_z) which are defined by their density ρ, temperature T and microturbulent velocity v_{trb}.
  - `SPOT`: a uniformly rotating sphere with the velocity $v^{\mathrm{sp}}_{\mathrm{rot}}$ and radius r^{sp}, which has constant temperature and density.
  - `DISC`: actually three types of objects:
    - wedge limited by the inner and outer spherical surface of radius $r^{\mathrm{dc}}_{\mathrm{in}}$ and $r^{\mathrm{dc}}_{\mathrm{out}}$ respectively and with angular half-width a^{dc},
    - slab with half-thickness a^{dc} limited by inner and outer spherical surface of radius $r^{\mathrm{dc}}_{\mathrm{in}}$ and $r^{\mathrm{dc}}_{\mathrm{out}}$, respectively, or a

* lens (two-axial ellipsoid) limited by the inner spherical radius $r_{\rm in}^{\rm dc}$ and the outer ellipsoid with semi-axes $r_{\rm out}^{\rm dc}$ and $a^{\rm dc}$, perpendicular and parallel to the rotation axis respectively.

In all cases, the velocity follows the Keplerian rotation, determined by the central mass $M_e^{\rm dc}$ and the density varies as a radial power-law with exponent $e_\rho^{\rm dc}$. The temperature can be:

* constant,
* depend on r as (accretion profile)

$$\frac{T(r)}{T^{\rm dc}} = \left(\frac{r^{\rm dc}}{r}\right)^{\frac{3}{4}} \left(1 - \sqrt{\frac{r^{\rm dc}}{r}}\right)^{\frac{1}{4}} , \tag{4.1}$$

* depend on r as power-law

$$\frac{T(r)}{T^{\rm dc}} = \left(\frac{r}{r_{\rm in}^{\rm dc}}\right)^{e_T} . \tag{4.2}$$

– `ENVELOPE`: a Roche-shaped object with constant temperature and density. Its shape is defined by the fill-factor $f_f^{\rm en}$, i.e. the ratio of the envelope's substellar point and the radius of the L1 point. The vertical extension is limited to $\pm h^{\rm en}$.

– `NEBULA`: a more robust case of the `DISC` object with a detailed vertical structure. It's vertical scale depends on $H(r) \propto \sqrt{T_{\rm gas}(r)}$ with a cut-off at $\pm a^{\rm neb} H(r)$. Density is assumed to follow a power law with respect to the radial coordinate with exponent $e_\rho^{\rm neb}$, with the vertical profile

$$\rho(z,r) = \rho(0,r) \exp\left[-\frac{z^2}{2H(r)^2}\right] . \tag{4.3}$$

It may contain a region with wind starting at $h_{\rm wind}^{\rm neb} H(r)$ and here the density structure follows

$$\rho(z,r) = \rho(0,r) \exp\left[-\frac{(h_{\rm wind}^{\rm neb})^2}{2}\right] . \tag{4.4}$$

Similarly to the `DISC` object there are three possible temperature profiles as described by Equations (4.1) and (4.2). However, there may be an inversion of temperature starting at $h_{\rm inv}^{\rm neb} H(r)$, with temperature multiplication factor $t_{\rm inv}^{\rm neb}$.

Furthermore, stellar wind is possible as an additional velocity component added to the Keplerian velocity of the disk, starting from $h_{\rm vel}^{\rm nb} H(r)$. The velocity component is calculated as

$$v(r,z) = v_{\rm wind}^{\rm nb} \left(1 - \frac{r^{\rm nb}}{\sqrt{r^2+z^2}}\right)^{e_{\rm wind}^{\rm nb}} . \tag{4.5}$$

– `SHELL`: an isothermal sphere with a power-law velocity field surrounding the central object, restricted by its inner $r_{\rm in}^{\rm sh}$ and outer $r_{\rm out}^{\rm sh}$ radius.

– `JET`: has a shape of one or two opposite cones emerging from the centre with optional inclination and is restricted by its inner $r_{\rm in}^{\rm jet}$ and outer $r_{\rm out}^{\rm jet}$ radius.
– `STREAM`: a cylinder with uniform velocity representing the streams of mass transfer.

The code `PYSHELLSPEC` [Mourard et al., 2018, Brož et al., 2021] works as a python wrapper utilizing the `SHELLSPEC` code. It provides a parallelization of the computation and utilizes a minimization algorithm for the χ^2-value [Nelder and Mead, 1965]. A general observable quantity $x_{ij}^{\rm obs}$, which is denoted by the index $i \in [1, N_j]$ in the j-th dataset, out of total number of datasets M, which has a weight w_j. If this quantity was measured with an uncertainty σ_{ij} and is compared to the respective synthetic quantity $x_{ij}^{\rm synth}$, the value of χ^2 is given as

$$\chi^2 = \sum_j^M w_j \sum_i^{N_j} \frac{\left(x_{ij}^{\rm obs} - x_{ij}^{\rm synth}\right)^2}{\sigma_{ij}^2} \,. \tag{4.6}$$

Furthermore `PYSHELLSPEC` provides the possibility of addition of sprectrointerferometric data along with computation of their synthetic values and comparison with the observed ones in terms of the χ^2 metric. This is done using the Discrete Fourier transform method (DFT) of the synthetic image produced for a particular orbital phase and wavelength by the `SHELLSPEC` code.

The program is thus able to process the following observable quantities:

1. rectified spectra (time of observation, wavelength, flux relative to the continuum),
2. SED (time, wavelength, absolute flux),
3. light curve (time, passband, magnitude),
4. absolute interferometry (time, wavelength, u and v coordinate, squared visibility),
5. differential interferometry (time, wavelength, u and v coordinate, amplitude of visibility, visibility phase),
6. triple product (time, two sets of u and v coordinates, modulus of the triple product, closure phase).

`PYSHELLSPEC` also utilizes the code `PYTERPOL` [Nemravová et al., 2016] which interpolates within a set of pre-calculated synthetic spectra with various values of the effective temperature, the local gravity and the metallicity. The `SHELLSPEC` code, after creating star-like objects, assigns a synthetic spectrum to each point on its surface. The synthetic spectra must be unrotated because the rotation (as well as other velocities) is computed by `SHELLSPEC` itself.

4.2 Observational data used

As demonstrated in Chapter 3, the φ Per system undergoes secular variations. Consequently, in order to obtain a consistent model valid at a particular time interval, it is necessary to select a suitable subset of the available data.

4.2.1 Optical interferometry

Interferometric data used were obtained by Mourard et al. [2015], who observed φ Per during September and October 2011 by the CHARA Array [ten Brummelaar et al., 2005] located at the Mount Wilson Observatory. Data were measured using the VEGA spectro-interferometer in 4-T mode [Mourard et al., 2009] in the visible spectral region.

Prior to analysis, I removed some of the visibility data with poor quality that either were out of the $[0, 1]$ interval or their error was larger than 0.1. The time of each observation was transformed to from geocentric to heliocentric date.

To obtain the absolute squared visibilities, Mourard et al. [2015] used two callibrators HD 3360 and HD 25642 with known angular diameters 0.28(2) and 0.44(3) mas, respectively. These observations were done in four spectral intervals: 4905 (BR), 6435 (RB), 6555 (RC) and 6705 Å (RR), with the passbands 150 Å. In total, this dataset contains 492 observations after reduction.

The reduced interferometric observations are listed in Table 4.1 along with their respective observation time, telescope configuration and number of measurements for each of the spectral region. Further more the region RR is visualized in Fig. 4.1 with colour-coded values of the squared visibility.

t [RJD]	φ [arb.u.]	Configuration	# BR	# RB	# RC	# RR
55832.8635	0.35	S2E2W1W2	16	12	19	24
55852.7743	0.50	S1S2W1W2	4	10	19	19
55852.8543	0.50	S1S2W1W2	6	7	12	16
55852.9643	0.50	E1E2W1W2	19	0	12	10
55853.7243	0.50	S1S2W1W2	14	20	20	20
55853.7843	0.50	S1S2W1W2	15	17	20	20
55853.8844	0.50	E1E2W1W2	8	20	20	20
55853.9344	0.50	E1E2W1W2	2	23	26	22

Table 4.1: Optical interferometry VEGA data. The column 'φ' corresponds to the orbital phase, 'Configuration' denotes the CHARA telescopes used and the four last columns contain the number of measurements for the respective spectral region.

4.2.2 Spectra

The collection of spectra presented in Chapter 3 spans more than two decades of observations, while the interferometric data were all collected within approximately 3 weeks. I therefore selected 8 red spectra to cover the entire orbital period as thoroughly as possible.

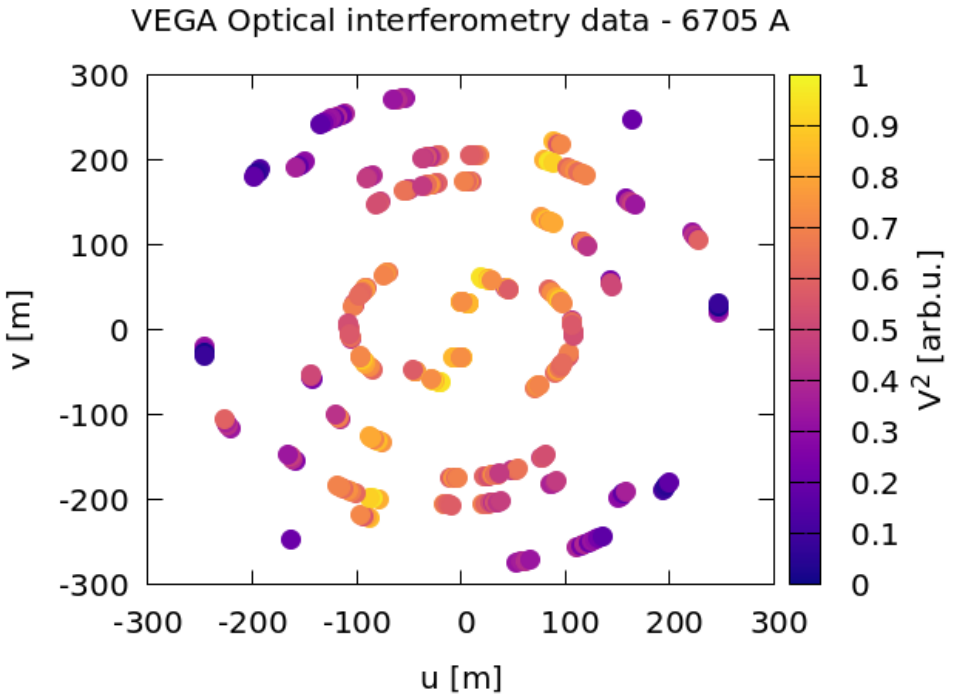

Figure 4.1: A (u, v)-plane coverage of VEGA observations with colour-coded values of the squared visibility.

Unfortunately I had less luck with spectra in the blue region. Although two of the red spectra selected extended to the blue wavelengths, I was forced to extend the time interval by approximately a year to use at least four blue spectra. To visualize the data, I plot them in a polar plot with the phase as the azimuthal coordinate in Fig. 4.2.

To shorten the calculation time I limited the continuum regions to 6540–6585 Å in the case of red spectra and 4855–4870 Å for blue spectra as these regions contain the Hα and Hβ lines, respectively.

The list of spectral datasets is shown in Table 4.2. In total, these datasets contain 5 639 idividual measurements in Hα and 4 180 measurements in Hβ. The measured uncertainty is difficult to estimate as the spectra were manually rectified. I set the value of $\sigma_{i,\mathrm{SPE}}$ as 0.01.

4.2.3 Absolute flux

To constrain the total emission computed by the model, I also included calibrated photometric measurements of φ Per. These were transformed to absolute flux using the Pogson equation

$$F_\nu = F_\nu^0 10^{\frac{2m}{5}}\,, \tag{4.7}$$

, where F_ν^0 is the calibration flux of a 0 mag star in a specific Johnson filter. The nominal fluxes were published by Bessell [1979]. Assuming that each measurement has an uncertainty Δm, the corresponding uncertainty of flux is

$$\Delta F_\nu = \frac{\mathrm{d}F}{\mathrm{d}m}\Delta m = \frac{2}{5}\ln(10) F_\nu \Delta m\,. \tag{4.8}$$

t [RJD]	φ [arb.u.]	Source	#	Dataset	Line
55693.60	0.99	Ond	175	1	Hα
55749.57	0.44	Ond	175	2	Hα
55759.52	0.51	Ond	176	3	Hα
55800.65	0.84	Ond	175	4	Hα
55774.59	0.63	BeSS	2054	6	Hα
55785.55	0.72	BeSS	1084	7	Hα
55831.52	0.08	BeSS	900	8	Hα
55857.42	0.29	BeSS	900	9	Hα
55831.52	0.08	BeSS	1415	11	Hβ
55857.42	0.29	BeSS	1418	12	Hβ
56163.41	0.70	BeSS	676	13	Hβ
56267.32	0.52	BeSS	671	14	Hβ

Table 4.2: Selected spectral datasets with their respective time of observation and calculated orbital phase. Column 'Source' indicates whether it is an Ondřejov or BeSS spectrum and the 'Line' column denotes whether the spectrum is in red region and contains Hα or blue region with Hβ.

The frequency-dependent flux F_ν is then converted to flux equidistant in wavelength $F_\lambda = \frac{c}{\lambda^2} F_\nu$.

Observations in the U, B and V filters were made during one night at the Hvar Observatory. The average values of three individual measurements are shown in Table 4.3. Values for the R and I filter were published by Ducati [2002]. The measurements, after conversion to the absolute flux, can be used to determine the spectral energy distribution (SED) and consequently the level of continuum.

For the purposes of describing the primary star I used the BSTAR and OSTAR grids [Lanz and Hubený, 2003, 2007]. The spectra spanned from 3250 Å to 7990 Å with a step of size 0.1 Å, extended to 10^4 Å using an extrapolation by the Planck function with steps of 10 Å.

t [RJD]	m	Δm	Source	Filter	λ_0	$\Delta\lambda$	F_ν^0	$10^4 F_\lambda$	$10^4 \Delta F_\lambda$
	[mag]				[Å]		[Jy]	[J · s^{-1} · m^{-3}]	
55876.22	3.24	0.01	H	U	3663	650	1810	20.45	0.19
55876.22	3.90	0.01	H	B	4361	890	4260	18.49	0.17
55876.22	4.03	0.01	H	V	5448	840	3640	8.98	0.08
51910.00	3.90	0.01	D	R	6407	1580	3080	6.20	0.06
51910.00	3.88	0.01	D	I	7980	1540	2550	3.37	0.03

Table 4.3: Absolute flux of φ Per.
Note: Column 'Source' refers to either observation from Hvar (H) or published by Ducati [2002] (D).

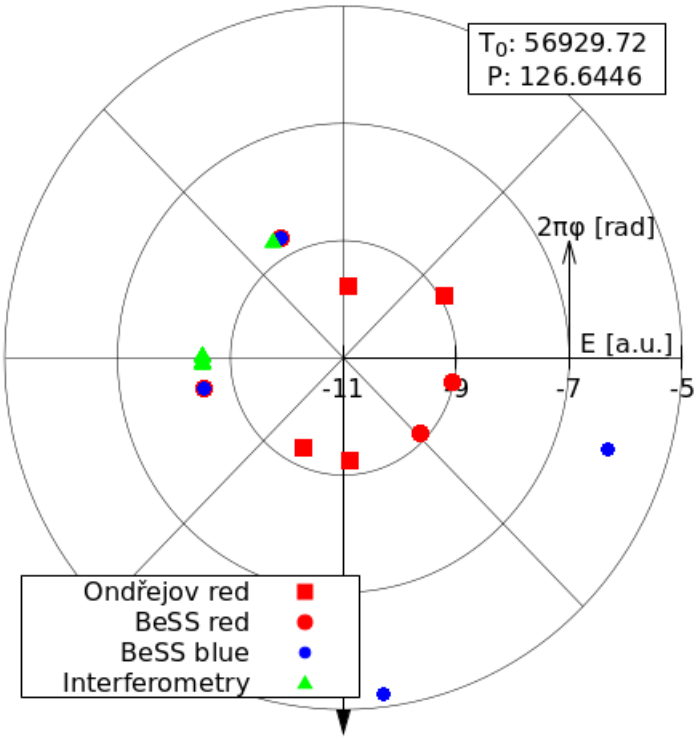

Figure 4.2: Graphical representation of the used data, radial axis corresponds to the epoch of the observation with respect to the ephemeris shown at the top of the table while the azimuth represents the orbital phase φ (the fractional part of the epoch). Two of the red spectra coincide with blue spectra.

4.3 Initial considerations

Any object surrounding either of the stars should to a high degree respect the Roche equipotentials. With the orbital period 126.64 d and masses of the components 9.6 and 1.2 $M_\odot$ [Mourard et al., 2015] the semimajor axis of the secondary equals approximately 234 $R_\odot$. Solving Equation (1.18) gives the location of the Lagrange points L_1 and L_2 as 164 and 322 $R_\odot$respectively. Given the upper limit of the primary radius being no larger then 10 $R_\odot$, taking into account the equatorial bulge, the star is by an order of magnitude smaller than the Roche lobe. Therefore it is reasonable to neglect its deformation caused by the gravitational effect of the secondary.

4.4 Fitting continuum interferometry

Most importantly, the optical interferometry constrains the physical extent of the disc. Before introducing any additional datasets, I shall consider only the interferometry data at first.

4.4.1 Geometrical model

In order to verify the presence of a disk surrounding the primary star being detected in the VEGA data I used the java software `LITpro` [Tallon-Bosc et al., 2008]. Here the user is able to create objects with various flux distribution in the field of view and the program computes synthetic visibilities on baselines given by the data.

To model the φ Per system, I used a uniform disk to represent the primary star and an elongated Gaussian to approximate the surrounding disk. In the program the uniform disk is described by its diameter $d_{\rm ud}$, flux weight $f_{\rm ud}$ and position of the centre ($x_{\rm ud}$, $y_{\rm ud}$) in the field of view. Meanwhile, the Gaussian is described by the FWHM along its minor axis $d_{\rm disk}$, flux weight $f_{\rm disk}$, elongation $e_{\rm disk}$ as a ratio between the major and minor axis, position angle of the major axis $\phi_{\rm disk}$ and position of the centre ($x_{\rm disk}$, $y_{\rm disk}$).

As the only data being used are the squared visibilities, it is possible to set the centre of both the star and the disk in the centre of the field of view. Upon assuming the radius of the star being $4.7\,{\rm R}_\odot$and the distance of the system as 186 pc the angular diameter of the star equals 0.24 mas. I fixed the angular diameter at this value as well as the position of both the star and the disk and let all other parameters converge. The result parameters of the best fit can be seen in Table 4.4 and the comparison between the model and the data as well as the synthetic image can be seen in Fig. 4.3.

This purely geometrical model can be used as a benchmark for further modeling in `PYSHELLSPEC`. It should be noted however, that in this model the two objects overlap at the centre to a large degree and thus the true flux weights might differ. In addition at no point was it considered that there is a part of the disc behind the star and therefore the rotated solution $\bar{\phi}_{\rm disk} = \phi_{\rm disk} + 180°$, meaning whether we can see 'above' or 'under' the disc, may also be valid. I also made an attempt to optimize the parameter $d_{\rm ud}$, however, it decreased significantly so it most likely is not well restricted by the data.

Par	Unit	Value	Error
$d_{\rm ud}$	mas	0.24	(fixed)
$f_{\rm ud}$		0.67	0.11
$d_{\rm disk}$	mas	0.16	0.03
$f_{\rm disk}$		0.33	0.07
$e_{\rm disk}$		4.1	0.9
$\phi_{\rm disk}$	°	103.6	1.6

Table 4.4: `LITpro` modeling of continuum interferometry – best-fit parameters.

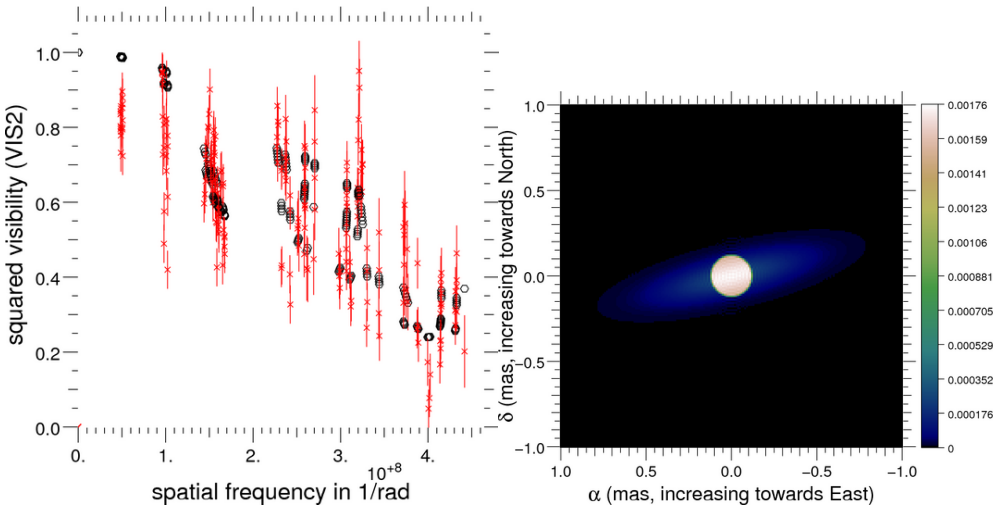

Figure 4.3: `LITpro` modeling of continuum interferometry: best fit comparison of the data and the model (left) and synthetic image (right).

4.4.2 Comparison of different disk-like structures

I constructed a set of five models with the star being surrounded by different structures – including three types of disc or a nebula-type object, with disc represented by either a wedge (model DcWedge), slab (DcSlab), or a lens (DcLens) while the nebula was computed for both power-law (NbPL) and accretion (NbA) temperature profiles.

The overall size of the grid was set to $[-50, 50]$ $R_\odot$ with distance between two grid-points of 0.4 $R_\odot$. The star (assuming its radius about 4.7 $R_\odot$) is then resolved by 23×23 pixels. As the interferometry is sensitive to the spatial flux distribution of the system and the contribution by the secondary is negligible in the visible passbands, the secondary was not included in this computation. Moreover, in order to 'prevent' the orbital motion of the primary and reduce the size of the grid (the program computes the Fourier transform of the image in barycentric coordinates), the value of the mass ratio q was set to $0.125 \cdot 10^{-4}$ (its presumed value multiplied by a factor of 10^{-4}).

The parameters optimized included the properties of the disc, where the outer radius was limited by the grid size (50 $R_\odot$), as well as the radius and temperature of the star to adjust the flux ratio between the disc and the star as well as the orbit's inclination and position angle. The distance was kept constant in this set of simulations (186 pc) as it should only be constrained by the SED.

A comparison between the continuum interferometric data and the best-fit models can be seen in Figures 4.4–4.8. In addition, the figures contain the synthetic image with a logarithmic scale. In the graphs comparing the modelled and observed visibilities I added the Fourier transform of a uniform disc for reference, derived from Eq. (1.33). This represents the star with the radius from the best-fit solution as it would be observed with no disc. In addition two further curves are present where the radius is multiplied by factors 3/2 and 2/3. This represents its possible range stemming from the star's oblique shape while in the model the star is spherical.

The differences between the various types of objects seem to be almost negligible when comparing the observed and synthetic interferometric data. Out of

the objects defined in the code, nebula is the most robust, containing a possibility of an optically thin atmosphere; it is also most tied to the physical quantities e.g. its thickness is governed by the temperature profile.

Apart from the apparent size of the star and the disc, the shape the V^2 function takes also depends on the flux ratio between the two. A dim but large disc does not appear that significantly in the interferometry as a bright albeit small one. This is due to the linearity of the Fourier transform where the complex visibility amplitudes are weighted by the respective flux, as can be seen from Eq. (1.36).

It should be noted, however, that despite the very similar synthetic squared visibilities some of the parameters differed significantly between the models. The area of the star in the model NbA was more than 2.3 times larger than in the model DcSlab (R^{star} being $7.09\,\text{R}_\odot$ and $4.65\,\text{R}_\odot$ respectively).

On the other hand in this model (and similarly in models DcWedge and NbPL) the disc is separated from the star by a visible gap whereas in the DcSlab and DcLens models this gap is not distinguished. It is reasonable to suspect that some flux of one object may be overflowing to the other and vice versa. This is impossible to constrain with purely interferometric data. In addition in the mode NbA, there appears to be an optically thick part of the disc present in front of the star blocking a part of its flux and effectively decreasing its observed size.

There is also a visible spread in values of temperature and density as well as their respective exponents. As previously said, the main constrain by the interferometry is the flux ratio which is governed mostly by the local temperature and density. The density in the model NbA converged to a value more than two orders of magnitude higher than other models. This high density caused a part of the disc to be optically thick and impossible to see-trough. As the disc was then opaque it was impossible to constrain its base density.

For the Nebula object, there are several parameters describing the atmosphere of the disc. These are, however, most likely not constrained by the interferometry as well.

Though the synthetic visibilities of all the models look similar, the synthetic images differ, e.g. in the model DcLens the projected disk appears to be only as wide as the star, while the disc in the model DcWedge seems much larger along the vertical axis. This is the effect of the used scale, where the outermost, dim parts only contribute negligible intensity in the image. The comparison of the two models in linear scale can be seen in Fig. 4.9 and it shows, that in fact both the discs do not extend past the stellar disk on the vertical axis.

Par	Unit	DcWedge	DcSlab	DcLens	NbPL	NbA
R^{star}	$\mathrm{R}_\odot$	5.24	4.65	5.20	6.32	7.09
T^{star}	kK	30.33	30.75	29.15	30.96	28.18
i	$^\circ$	73.54	82.88	81.82	75.31	79.87
Ω	$^\circ$	282.7	281.9	282.1	281.85	282.57
a	$^\circ/\mathrm{R}_\odot$/-	5.79	4.40	3.62	0.44	0.37
r_{in}	$\mathrm{R}_\odot$	9.3	10.3	10.9	13.1	16.6
r_{out}	$\mathrm{R}_\odot$	48.7	59.1	40.3	37.8	46.0
T	kK	12.36	12.72	14.91	11.64	16.66
ρ	10^{-12} g·cm^{-3}	13.30	6.51	7.67	13.89	3903.60
v_{trb}	km·s^{-1}	3	141	121	205	115
e_ρ		−2.94	−3.66	−3.56	−2.99	−0.70
e_T		−0.18	−0.45	−0.45	−1.05	
h_{inv}					1.4	1.3
T_{inv}					1.6	1.5
h_{wind}					2.7	2.5
h_{c}					22.6	10.9
h_{vel}					7.4	3.7
v_{wind}	10^3 km·s^{-1}				1.85	0.75
e_{wind}					4.6	2.6
h_{shd}					3.3	4.7
χ^2		1450	1494	1510	1519	1456
N_{IF}		260	260	260	260	260

Table 4.5: Models based only on interferometry in red continuum. The parameters in the 'Par' column are as follows: R^{star} – radius of the primary star, T^{star} – its temperature, i – orbital inclination, Ω – longitude of the ascending node, r_{in} – inner radius of the disc, r_{out} – outer radius of the disc, T – temperature, ρ – density, v_{trb} – micro-turbulent velocity, e_ρ – density radial dependence exponent, e_T – temperature exponent, h_{inv} – start of the inverse temperature region, T_{inv} – temperature multiplication factor in the inversion, h_{wind} – start of the wind region, h_{c} – multiplication factor of vertical scale height, h_{vel} – start of the radial wind, v_{wind} – terminal wind velocity, e_{wind} – wind velocity exponent, h_{shd} – start of the scattering region.
The exact meaning of the parameter a depends on the respective model as different structures use different definition but same notation. In general, though, it is related to the vertical extent of the object. For the wedge model this parameter is expressed in $^\circ$, for lens and slab in $\mathrm{R}_\odot$ while for the nebula object a is dimensionless. This is further explained in the code description at the beginning of this chapter.

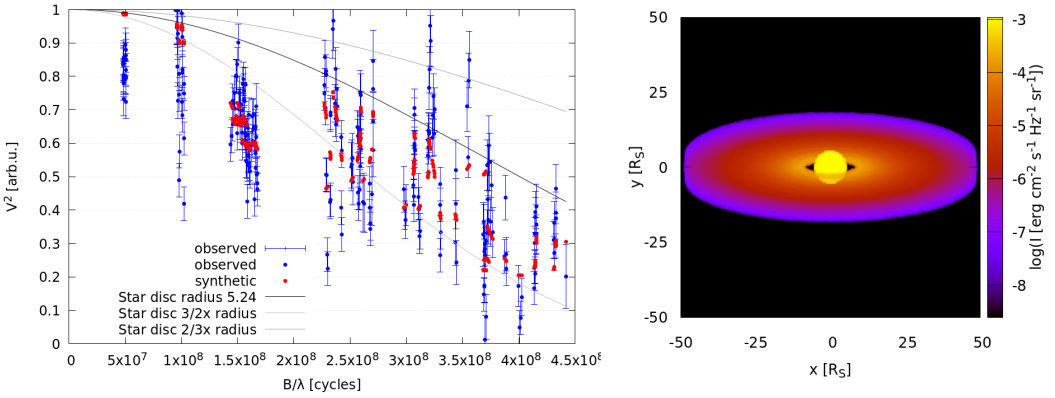

Figure 4.4: Model DcWedge: comparison between the best-fit model and RB and RR OI data (left) and synthetic image in normal coordinates (right). Along the synthetic squared visibilities three theoretical curves are plotted representing the star of radius from the fit and its value multiplied by a factors 3/2 and 2/3 as it would be observed without the surrounding disc.

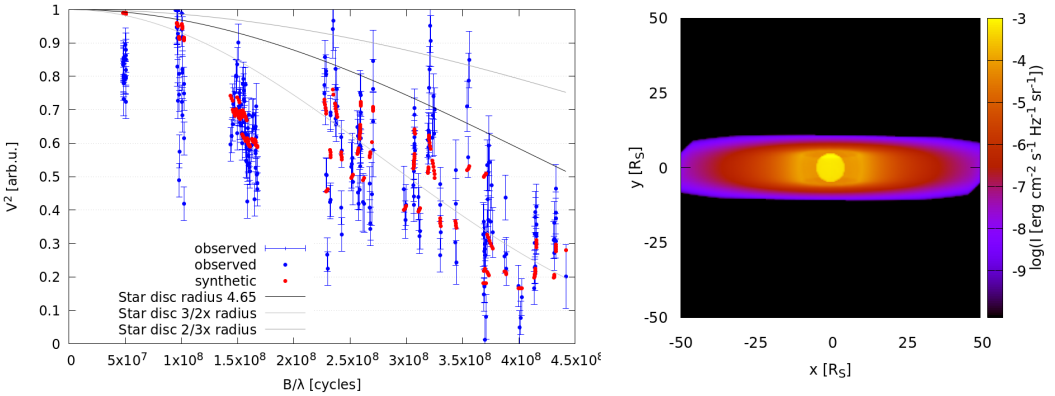

Figure 4.5: Model DcSlab: the same as Fig. 4.4.

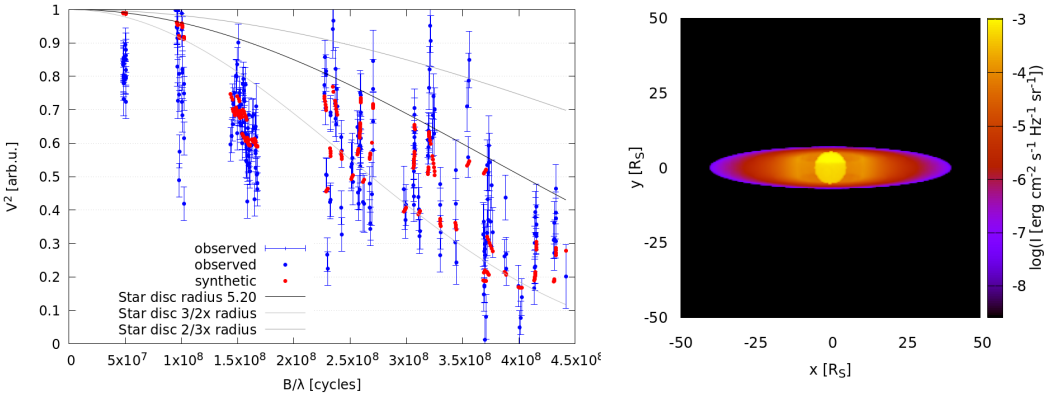

Figure 4.6: Model DcLens: the same as Fig. 4.4.

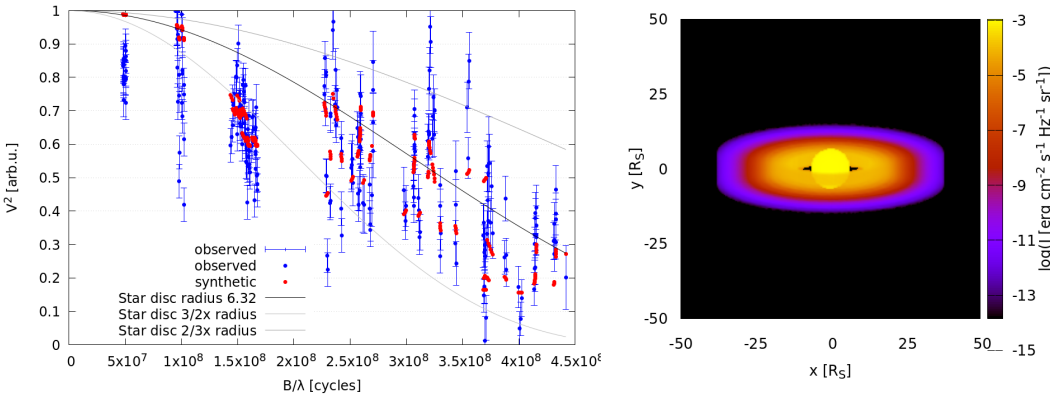

Figure 4.7: Model NbPL: the same as Fig. 4.4.

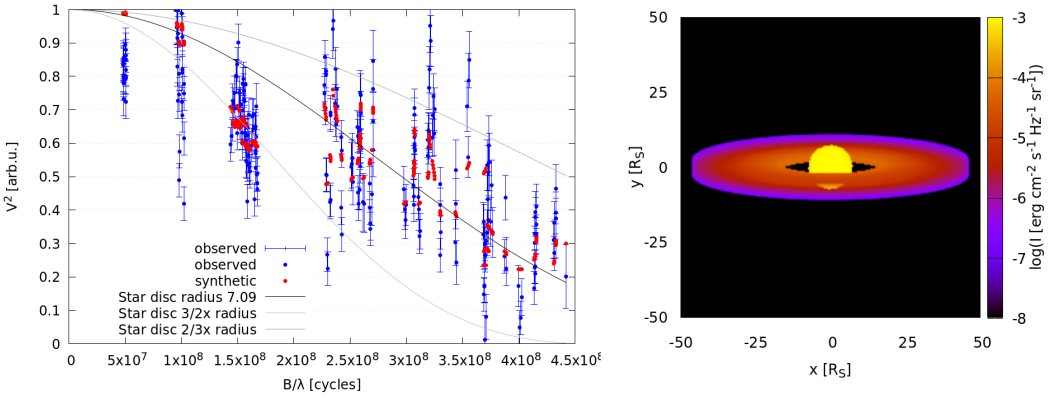

Figure 4.8: Model NbA: the same as Fig. 4.4.

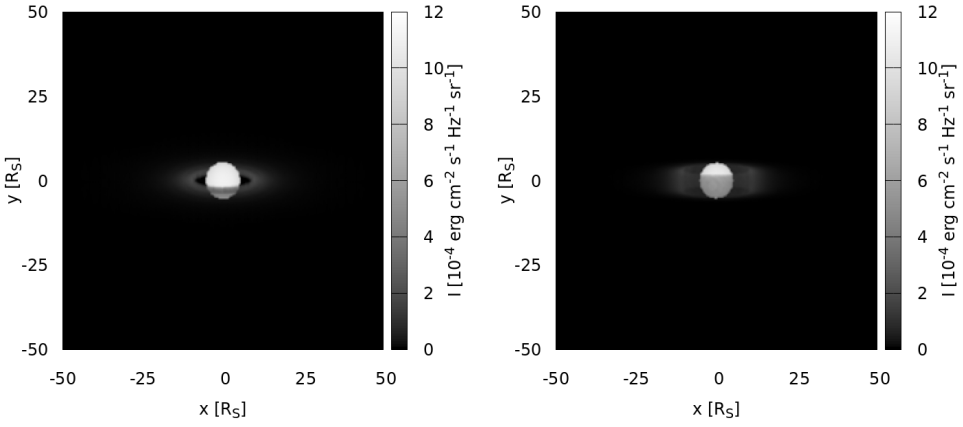

Figure 4.9: Comparison of the synthetic images from the model DcWedge (left) and DcLens (right) in linear scale of intensity.

4.4.3 Nebula with different temperature profiles

The flux of the disc depends on its properties such as density and temperature and their respective radial profiles. To map the χ^2-space more thoroughly I calculated the optimization for two distinct temperature ranges: 5 to 18 kK and 18 to 31 kK. The lower interval of temperatures corresponds to the expected maximum of Hα emission in such environment, while the second interval is closer to the temperature of the inner star. As there are two options for the form of the temperature profile (power-law and accretion) I created additional models for the aforementioned intervals. This lead to four distinct models.

I converged each model in two steps, first for the parameters of the nebula and subsequently fixing this result and converging the parameters of the star. The results can be seen in Tab. 4.6.

One can notice a set of butterfly-like structures which appear on the synthetic images above and below the disc. These are created by the presence of the wind region and temperature inversion. These regions are modelled as cones centered in the disc and the inclination and 2D projection results in this shape. However, it should be noted that the bulk of this region is more than 4 orders of magnitude weaker than the disc itself and as such its contribution to the continuum flux is minuscule.

Comparing these models reveals three of the models (namely the accretion high temperature and both power-law profiles) are similar with almost negligible differences. All calculations found a similar value of density (between 11 and $15 \cdot 10^{-12}\,\mathrm{g{\cdot}cm^{-3}}$). Although they share similar issues as the previous batch of models such as high visibilities on short cycles and inability to reproduce the high visibilities on long cycles.

However, the model A-lowT converged to a very different solution. It appears to be optically thicker than the other three, with density 3–4$\times$ higher, and the disc essentially covers the entire star. This could be understood as an alternative model, however, upon calculating the profile of Hα for such an optically thick model all the emission is diminished while the other models show at least some emission, as can be seen in Fig. 4.14. The Hα synthetic profile from the model PL-lowT does not match the observed data but this is not surprising because the model does not (yet) include any spectral data in the χ^2 metric (see Section 4.6).

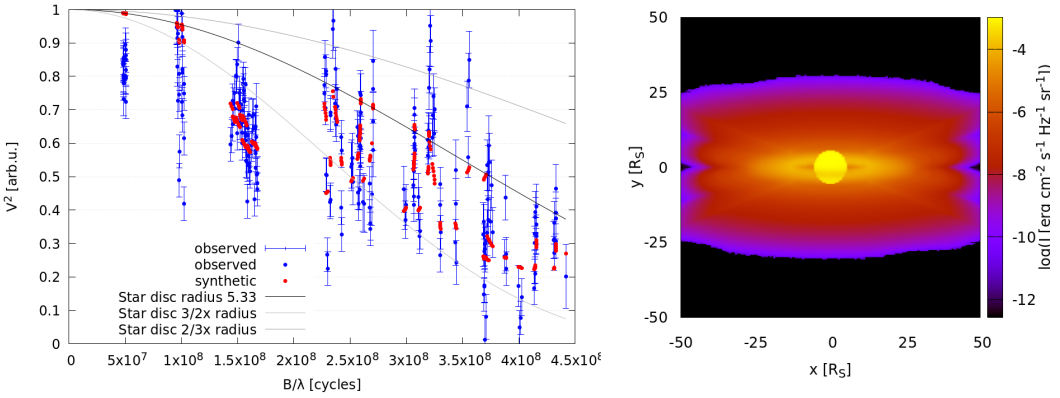

Figure 4.10: Model PL-lowT – nebula with power law and low temperature profile: comparison between the best-fit model and RB and RR intereferometric data (left) and synthetic image (right).

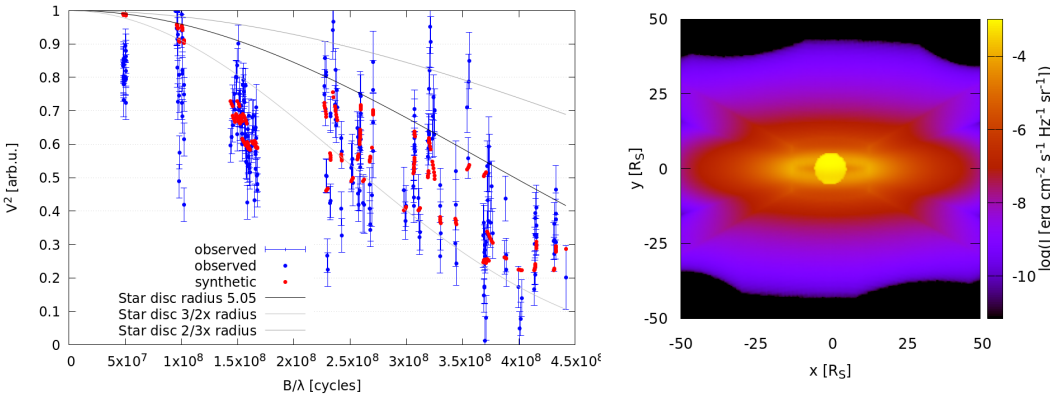

Figure 4.11: Model PL-highT – nebula with power law and high temperature profile: the same as Fig. 4.10

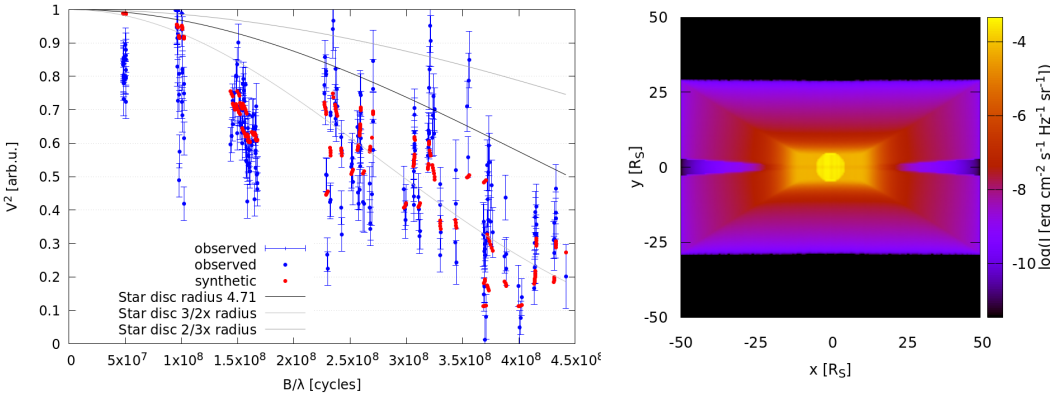

Figure 4.12: Model A-lowT – nebula with accretion and low temperature profile: the same as Fig. 4.10.

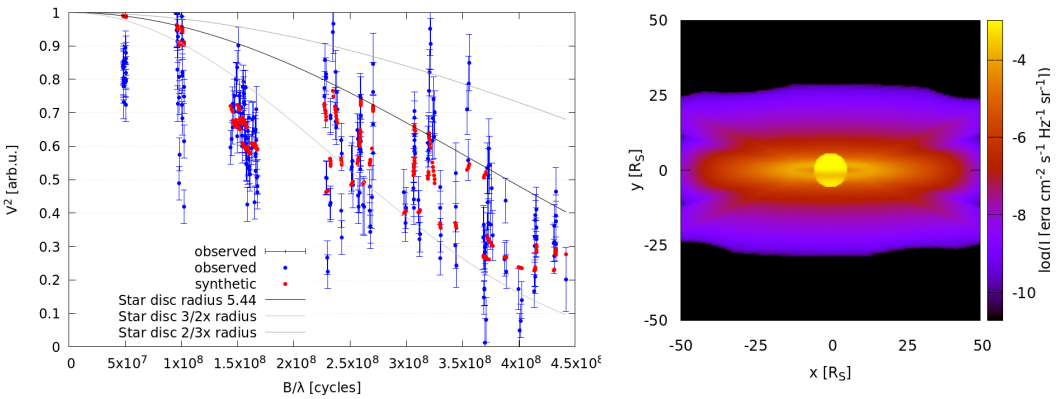

Figure 4.13: Model A-highT – nebula with accretion and high temperature profile: the same as Fig. 4.10.

Par	Unit	PL-lowT	PL-highT	A-lowT	A-highT
$r_{\rm in}$	$R_\odot$	12.86	12.62	9.67	12.75
$r_{\rm out}$	$R_\odot$	51.85	54.81	50.38	53.02
$h_{\rm inv}$		0.83	1.81	0.08	1.49
$t_{\rm inv}$		1.40	1.40	0.53	1.73
$h_{\rm wind}$		2.60	2.63	0.70	2.66
$h_{\rm c}$		4.72	5.20	7.34	3.80
$h_{\rm vel}$		4.78	4.88	6.72	4.57
$v_{\rm wind}$	km·s^{-1}	708.8	752.6	2455.3	663.4
$e_{\rm wind}$		2.95	3.73	6.00	3.60
$h_{\rm sh}$		3.17	2.99	0.51	3.09
T	K	14.55	26.81	17.48	33.92
ρ	10^{-12} g·cm^{-3}	11.49	11.24	48.67	15.04
$v_{\rm trb}$	km·s^{-1}	85.22	126.04	482.41	76.53
e_ρ		−2.54	−3.20	−0.18	−2.55
$e_{\rm T}$		−0.97	−1.02		
Ω	°	283.06	282.29	281.42	283.02
$R^{\rm star}$	$R_\odot$	5.33	5.05	4.70	5.44
$T^{\rm star}$	kK	32.25	31.86	29.30	30.21
i	°	80.72	79.13	90.00	83.08
Ω	°	281.23	282.18	281.42	281.99
d	pc	177.40	177.48	186.00	188.01
χ^2		1482	1472	1549	1485
$N_{\rm IF}$		260	260	260	260

Table 4.6: Models of Nb based only on interferometry in red continuum with two base temperatures of nebula, fitted subsequently for the nebula and then for the star.

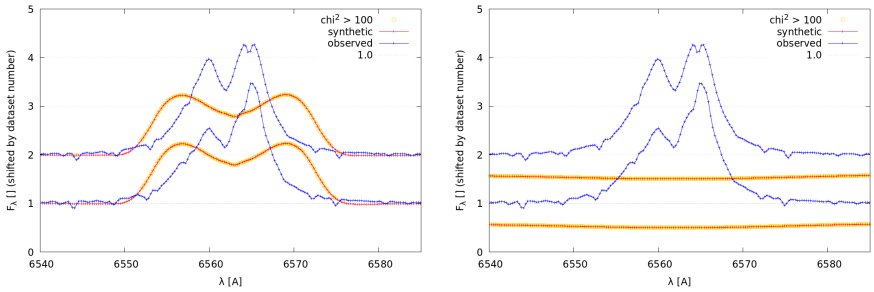

Figure 4.14: Comparison of Hα profile calculated for PL-lowT (left) and A-lowT (right) models.

4.4.4 Fitting with calibrated $V^2 > 1$

Even before attempting to converge any models based on interferometry I did not take into account measurements with $V^2 > 1$ as there must have definitely been an error during the data reduction. When fringes are detected, their visibility is compared to a calibrator star of known diameter, observed just before and after the science star. Because the theoretical value of the calibrator visibility is known from its diameter, it is possible to determine the visibility of the science fringes. A possible explanation might be that the calibrator fringes in these particular measurements were affected by a variable seeing and their visibility was temporarily lower than it was supposed to. This caused then the science fringes appear with relatively high contrast and thus having $V^2 > 1$. On the other hand if these measurements are included in one group of data ('shot') it may be more correct to use the whole group. It is thus possible to include them in the modeling to see how much it would affect the model.

I calculated the model PL-lowT including these troubling data. This naturally caused an increase of the χ^2-value but at the same time the residua were more evenly distributed. It also does not force the model into low $V^2 \approx 0.8$ on short baselines ($5 \cdot 10^7$ cycles). This is an important indication that the circumstellar matter is not distributed in a significantly larger volume. Eventually, it does not seem to have any large-scale impact on the final result, which is very similar to the original model PL-lowT.

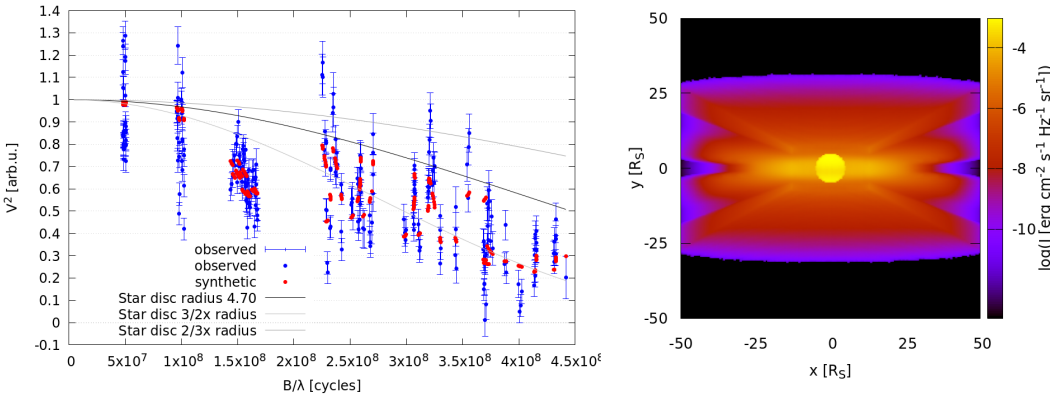

Figure 4.15: Model PL-lowT-highV – nebula with power-law and low temperature profile with the interferometric data with $V^2 > 1$ included: the same as Fig. 4.10.

4.5 Addition of SED

Before including any of the rectified (normalized) spectra, it is necessary to calibrate the continuum flux. The reason is that if the value of absolute continuum flux were too different from the observed and synthetic data, this would naturally, after normalization, affect all line intensities.

Due to the similarities between the models in the last set I chose the start of the computation as in the PL–lowT model i.e. temperature described as power-law with base value between 5 and 18 kK. Because the inclusion of interferometric data allows to solve for the angular size of all objects, I created two distinct models with distance fixed and free for optimization.

Upon reviewing the calculated fluxes, there appears to be a large difference in the U band where the synthetic value is higher than the observations suggest (subsequently decreasing all other synthetic values). There might be several reasons affecting this particular data-point. First, it is necessary to note that the calculation of the synthetic value in `SHELLSPEC` is actually monochromatic, that is the flux is only computed for the effective wavelength, not across the Balmer jump. This is a fairly good approximation for longer wavelengths where the Planck function is more gradual.

Second, one needs to consider the effective wavelength of the wide U band which is just before the Balmer jump, where the opacity of the star's atmosphere is relatively lower then after the jump.

Third, the program `SHELLSPEC` is a radiation equation solver along the line of sight. An important source of opacity in the UV region is scattering which is inversely proportional to the wavelength. It is possible that the model underestimate the scattering opacity.

Considering these explanations for the high synthetic value, I removed the U measurement from the dataset reran the convergence. With the largest χ^2-contribution removed, the contribution from interferometric data would outweigh the SED. To prevent this I set the weight of the IF data to 0.1.

As can be seen from Figs. 4.18 and 4.19, the models now recovered the photometric data almost exactly. On the other hand, this also caused a slight decrease in the synthetic V^2 in the region of $1.5 \cdot 10^8$ cycles.

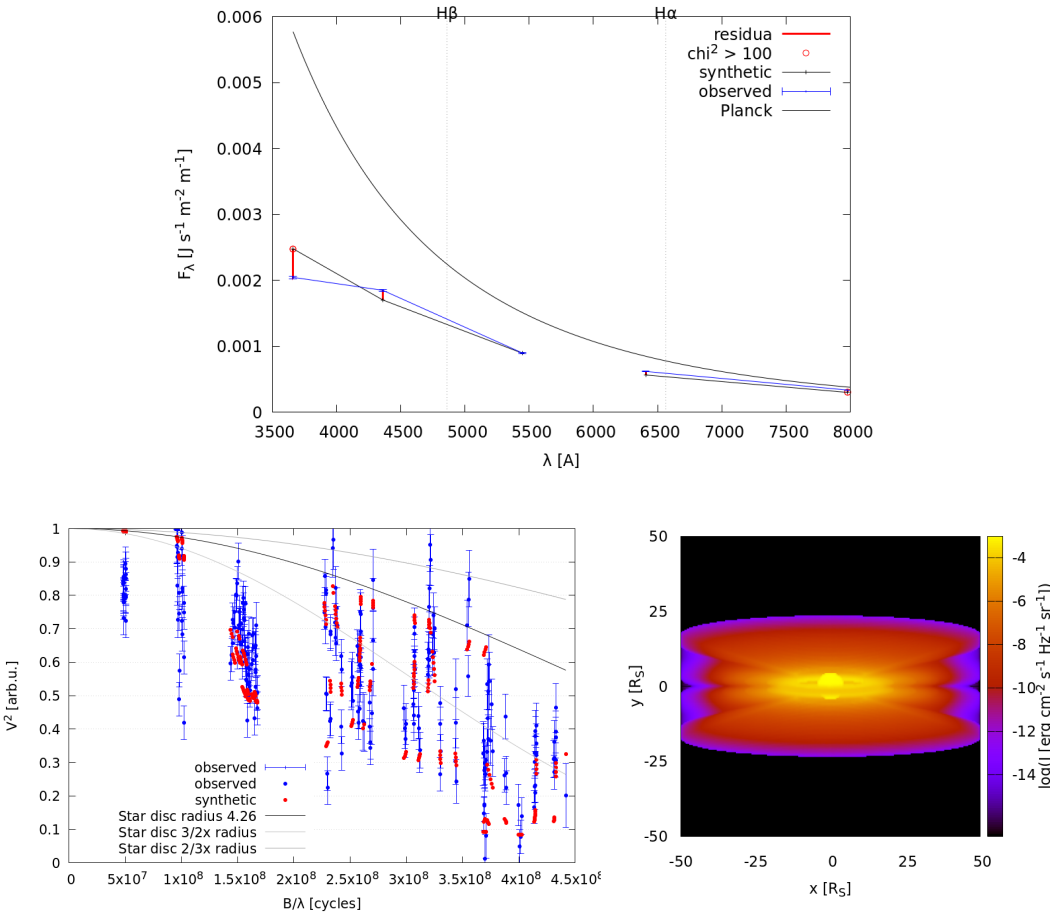

Figure 4.16: Model Nb-SED – nebula with SED data and fixed distance: comparison between the best-fit model and SED data (top) with the Planck function corresponding to the parameters of the star which is partially absorbed by the surrounding disc for reference. Best-fit squared V^2 with respect to B/λ compared to the red continuum observed interferometry (bottom left) and the synthetic image (bottom right).

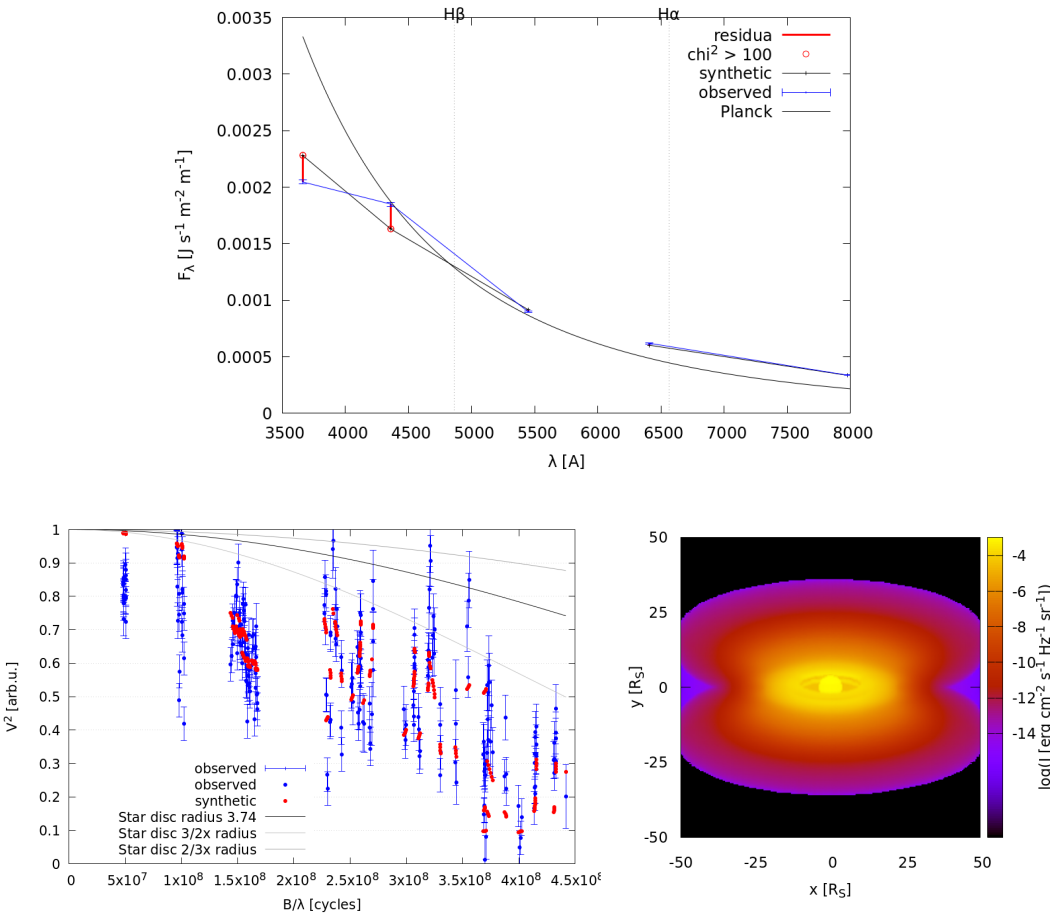

Figure 4.17: Model Nb-SED-D – nebula with SED data and fitted distance: the same as 4.16.

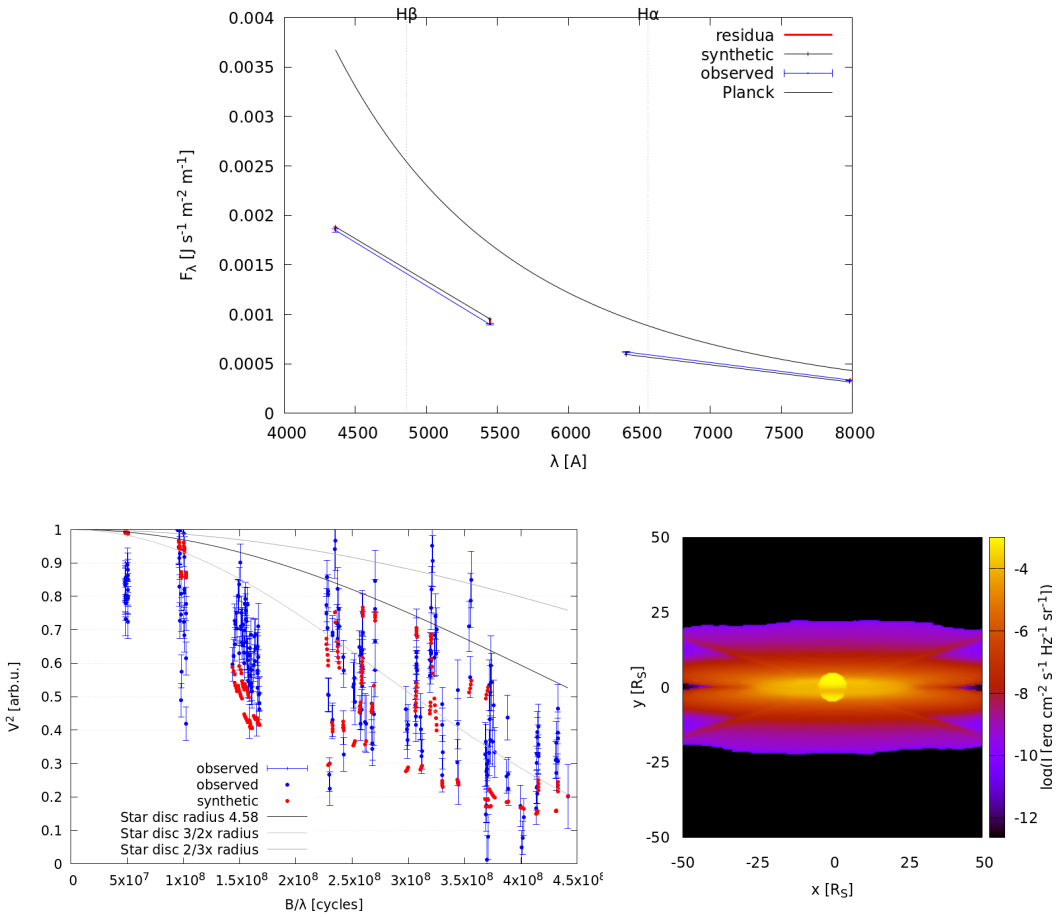

Figure 4.18: Model Nb-SED-rU – nebula with SED data (without the U-band measurement) and locked distance: the same as 4.16.

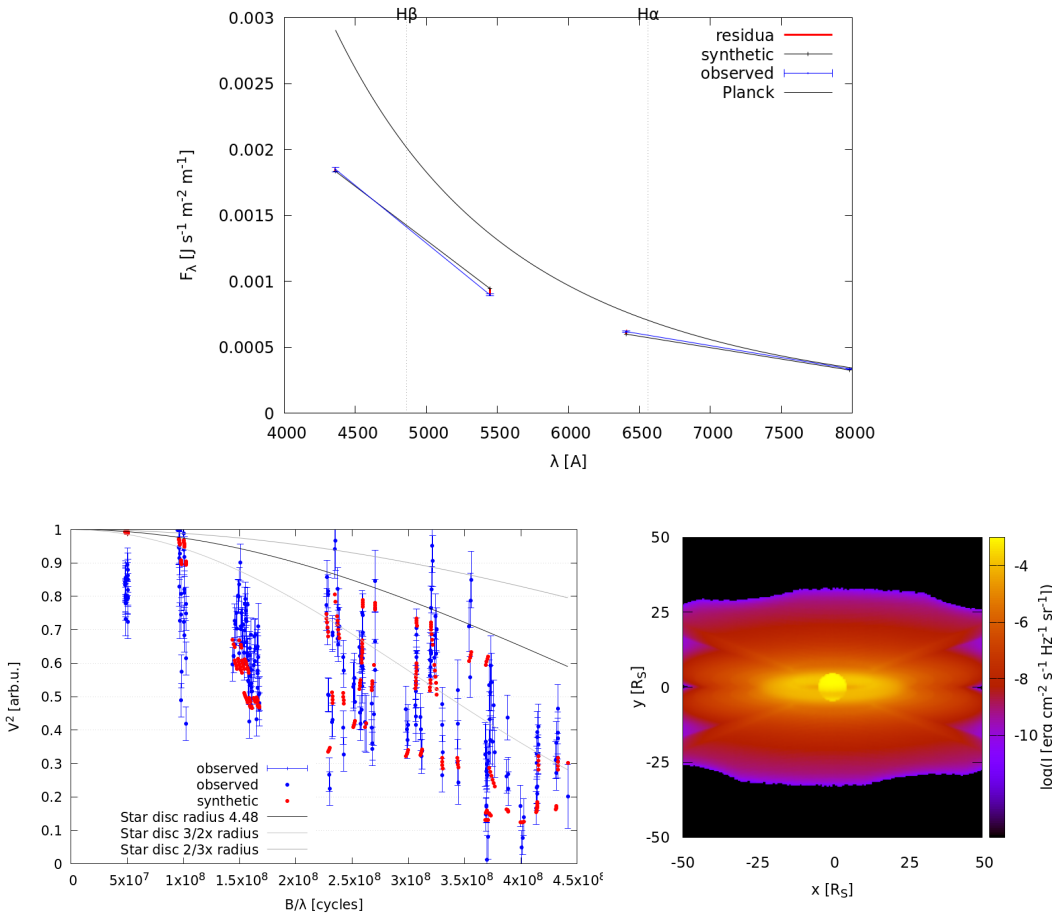

Figure 4.19: Model Nb-SED-rU-D – nebula with SED data (without the U-band measurement) and fitted distance: the same as 4.16.

Par	Unit	Nb-SED	Nb-SED-D	Nb-SED-rU	Nb-SED-rU-D
R^{star}	$\mathrm{R}_\odot$	4.26	3.74	4.58	4.48
T^{star}	kK	30.49	31.23	30.11	29.24
r_{in}	$\mathrm{R}_\odot$	11.24	10.44	13.41	13.41
r_{out}	$\mathrm{R}_\odot$	49.75	50.35	53.05	53.79
h_{inv}		0.77	0.63	0.73	0.75
t_{inv}		1.80	1.91	1.99	1.92
h_{wind}		2.67	2.50	2.96	2.64
h_{c}		4.91	7.76	3.85	5.51
h_{vel}		5.11	6.25	4.60	4.97
v_{wind}	$\mathrm{km{\cdot}s^{-1}}$	924.55	1117.19	1106.17	1205.27
e_{wind}		3.17	3.31	2.97	3.07
h_{sh}		3.91	2.60	4.58	4.07
T	kK	11.86	8.07	15.12	13.51
ρ	10^{-12} $\mathrm{g{\cdot}cm^{-3}}$	81.42	105.77	21.41	18.48
v_{trb}	$\mathrm{km{\cdot}s^{-1}}$	92.19	242.14	88.02	96.99
e_ρ		−4.79	−4.52	−2.71	−3.22
e_{T}		−1.09	−1.08	−1.08	−1.09
i	°	82.91	70.91		80.82
Ω	°	283.05	281.56	280.74	281.92
d	pc		219.60		199.71
N_{IF}		260	260	260	260
w_{IF}		1	1	0.1	0.1
χ^2_{IF}		1957	1587	248	193
N_{SED}		5	5	4	4
w_{SED}		1	1	1	1
χ^2_{SED}		823	336	109	54
χ^2_{total}		2780	1922	357	246

Table 4.7: Models of Nb based on interferometry in red continuum and SED.

4.6 Addition of red spectra

When attempting to create any model of the system with heterogeneous datasets one must always consider the importance of their relative weights as to balance the χ^2 contribution. Furthermore, even a single element of interferometric or photometric data provides more information and constrains on the model than a single element of the spectrum, despite being equivalent in the χ^2 metric.

In case of the data presented, it can be easily verified that spectra would dominate in the χ^2 metric and the resulting model would almost disregard the interferometry and photometry. The spectra in the red region amount to 5 637 points, while the interferometry to 260 and the SED to only 4. In the models using both interferometry and SED, the χ^2 contribution was about 20–40$\times$ larger from the interferometry than SED, as can be seen in Table 4.7, so the weight of SED must be set larger by about an order.

In all the previous sections, I also neglected the influence of the secondary to make the calculation of the Fourier transform simpler. In this case, however, the orbital velocity of the primary (K_1) cannot be neglected. Therefore, I set the mass ratio back to its original value (1/8). Instead, I changed the program itself and disabled the procedure of shifting the synthetic image to barycentric frame but kept the rotation due to i and Ω. It should be stressed out that this change does not have a negative effect if the model computes only synthetic visibilities. Once any data containing closure phases are added, this simplification cannot be used.

I tried to compute a model with the weights equal to 1 000 and 10 000 for the IF and SED data, respectively, and 1 for the spectra. The high value was chosen to see if the model can adapt to the spectra and if there is a significant difference with respect to previous models. The best-fit parameters of the described models are listed in Tab. 4.8.

Models SPE and SPE-wind

I converged the parameters with and without the addition of the wind region. The respective models are shown in Figures 4.20 and 4.21. However, it does not seem that the wind has a substantial impact on the model. Overall the model converged to an very thin disc with almost no vertical extension and no radial dependence in density ($|e_\rho| < 0.1$). The drop in squared visibilities is pronounced even further than in some of the IF + SED models in Section 4.5.

The increase in the synthetic Hα line intensity is steeper than in the observed data and the synthetic blue peak is significantly more prominent. The model being computed is axially symmetric and it is most likely not able to produce this observed asymmetry.

Model onlyWings

Perhaps it would help the convergence if the central part of the line was not included and only the line wings were computed. Consequently, I changed the

value of $\sigma_{i,\mathrm{SPE}}$ to 0.2 (i.e. 20× its previous value) for the data with wavelengths in the interval $[6558, 6567]$ Å .

However, this freedom in the convergence (as seen in Fig. 4.22) caused the core of the line to completely 'disappear' and the model was not even able to reproduce the red end of the wings. Furthermore, the central density reached very high values and most likely the central parts of the disc became optically thick.

Model onlySPE

To showcase a model being preferred purely by the spectra, I removed the IF and SED data entirely from one fitting (Fig. 4.23). It is clear that this model does not represent the system at all – the squared visibility drops to zero on very short baselines due to the huge disc being present and the SED show an excess on long wavelengths at the expense of the blue band. The resulting disc became not only geometrically large but also optically thick as it hides the central star almost entirely. However, this model does demonstrate the importance of the SED calibration – the synthetic level of continuum is about two times higher than the observed one in the Hα region.

There is, however, a small asymmetry in the central part of the synthetic line. So far, this has been the only model to produce such result. This is the effect of the optically thick disc blocking a part of the incoming light. Furthermore, as these asymmetries appear in the central part, they are partly related to the orbital motion of the disc. If the physical radius of the disc is about $50\,\mathrm{R}_\odot$, then the barycentre lies in about the middle of this distance.

Model Restricted

A large portion of the Hα emission comes from the disc's hot optically thin atmosphere. This is controlled mostly by the parameters of temperature inversion h_{inv} and t_{inv}. I thus manually searched within the space of parameters to find a model where the synthetic visibilities at $B/\lambda \approx 1.5 \cdot 10^8$ reflect the observed values while, at the same time, a sufficient emission is present. In order to shorten the time of one iteration, I converged only the Ondřejov spectra. To balance the χ^2 metric, I reduced the weights of IF and SED by a factor of 10.

I then fixed some parameters and let only the following converge: h_{inv}, t_{inv}, T, ρ, v_{trb}, i, Ω, and v_γ. For reference, Table 4.9 shows the upper and lower limit of each converged parameter. From Fig. 4.24, it is evident that the synthetic interferometry is comparable with the observed one, but the Hα line is much steeper and wider, with a more pronounced central absorption core than the previous models. Furthermore, the synthetic SED values are higher values for shorter wavelengths. Nevertheless, this is the *preferred* compromise model provided the φ Per system is composed of the central star and geometrically small optically thin disc and other flux flux contributions are negligible. See Chapter 5 for a discussion of other possibilities.

I also recovered some monochromatic synthetic images from the `SHELLSPEC` computation in several distinct wavelengths to demonstrate the changes in the structure of the disc across the Hα line, which can be seen in Fig. 4.25.

Par	Unit	SPE	SPE-wind	onlyWings	onlySPE	Restr	
R^{star}	$\mathrm{R}_\odot$	3.52	3.53	4.28	4.98	4.7	
T^{star}	kK	34.89	34.42	31.52	30.57	29.30	
R_{in}	$\mathrm{R}_\odot$	11.69	11.65	8.85	8.91	11.00	
R_{out}	$\mathrm{R}_\odot$	58.41	58.95	68.11	65.94	50.86	
h_{inv}		0.92	1.25	1.92	1.84	1.88	*
t_{inv}		1.89	1.89	1.74	1.30	2.88	*
h_{wind}			2.70				
h_{c}		0.44	0.47	5.00	5.37	2.49	
h_{vel}		7.82	7.85	7.44	7.44	6.50	
v	$\mathrm{km{\cdot}s^{-1}}$		1118.14				
e_{v}			1.14				
h_{sh}		4.95	3.70	6.44	6.75	4.17	
T	kK	14.85	14.85	13.19	12.81	16.48	*
ρ	10^{-12} g $\mathrm{cm^{-3}}$	9.93	9.88	199.66	495.92	44.29	*
v_{trb}	$\mathrm{km{\cdot}s^{-1}}$	1.73	2.20	5.55	24.38	44.90	*
e_ρ		−0.09	−0.07	−2.35	−1.00	−2.50	
e_{T}		−0.57	−0.57	−1.06	−0.44	−1.00	
i	°	81.85	81.64	75.70	85.08	85.23	*
Ω	°	287.12	285.62	286.64	270.00	281.99	*
v_γ	$\mathrm{km{\cdot}s^{-1}}$	−5.60	−10.00	7.91	−2.86	−6.61	*
χ^2_{IF}	10^6	2.92	2.92	1.61		0.16	
N_{IF}		260	260	260		260	
w_{IF}		1000	1000	1000		100	
χ^2_{SED}	10^6	0.38	0.33	0.52		0.07	
N_{SED}		4	4	4		4	
w_{SED}		10000	10000	10000		1000	
χ^2_{SPE}	10^6	5.63	5.29	0.67	1.69	1.71	
N_{SPE}		5637	5637	5637	5637	700	
w_{SPE}		1	1	1	1	1	
χ^2_{total}		8.93	8.54	2.81	1.69	1.95	

Table 4.8: Models of the disc based on red continuum interferometric and SED data along with Hα spectra. Note that for the Restr model, only the parameters denoted by * were converged, others were kept fixed.

Par	Unit	Lower	Upper	Fitted
h_{inv}		0.5	10	1.88
t_{inv}		0	3.0	2.88
T	kK	10	18	16.48
ρ	10^{-12} g·$\mathrm{cm^{-3}}$	9	100	44.29
v_{trb}	$\mathrm{km{\cdot}s^{-1}}$	0	50	44.9
i	°	70	90	85.23
Ω	°	270	340	281.99
v_γ	$\mathrm{km{\cdot}s^{-1}}$	-10	20	-6.61

Table 4.9: Fitted parameters of the model Restr with their lower and upper limit assumed in the convergence.

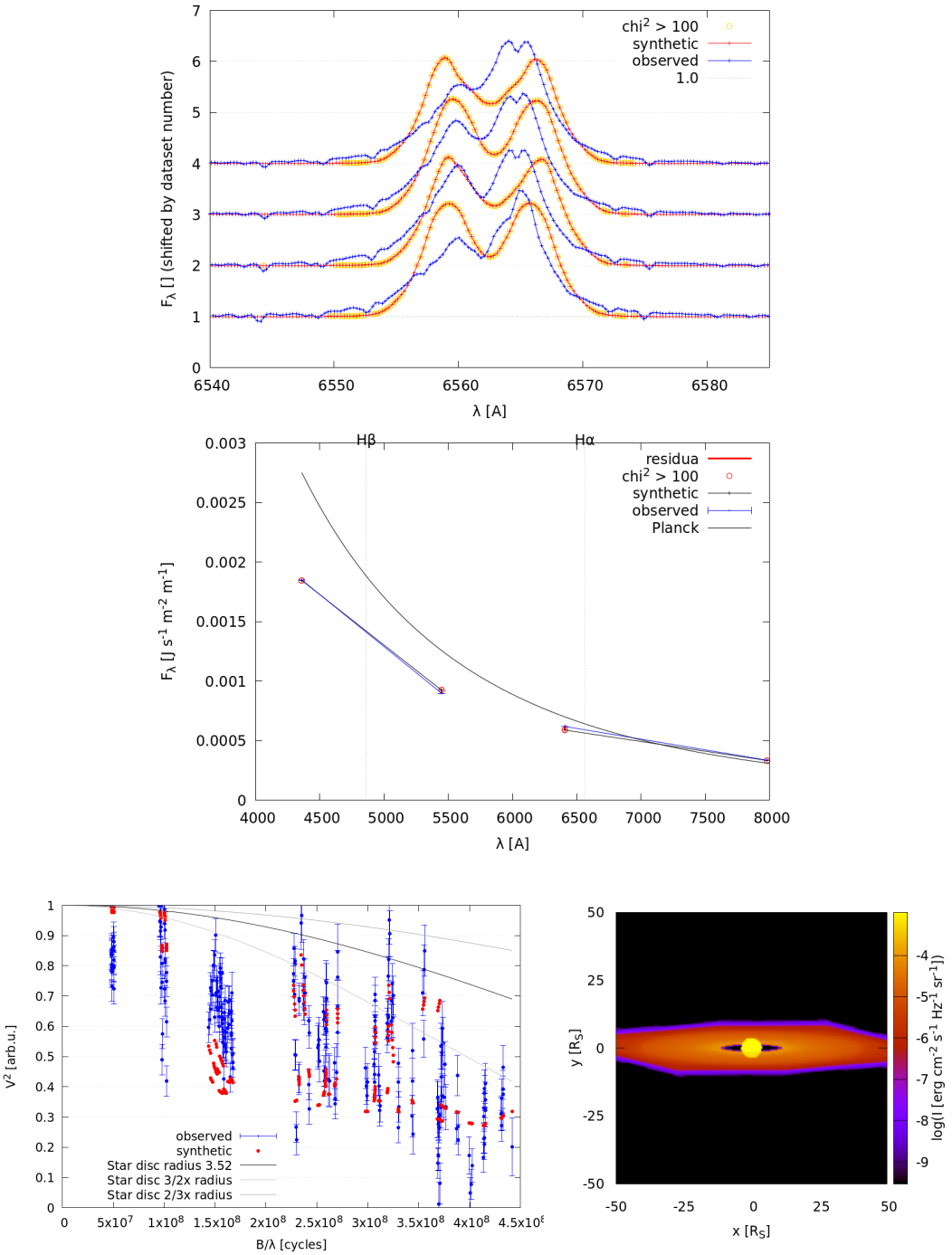

Figure 4.20: Model Nb-SPE: nebula with interferometry, SED data and spectra included: comparison between the best-fit model and observed data, Hα profile (top), SED (centre), interferometry (bottom left) and the synthetic image (bottom right). Note than only the Ondřejov spectra are displayed in the top diagram for comparison.

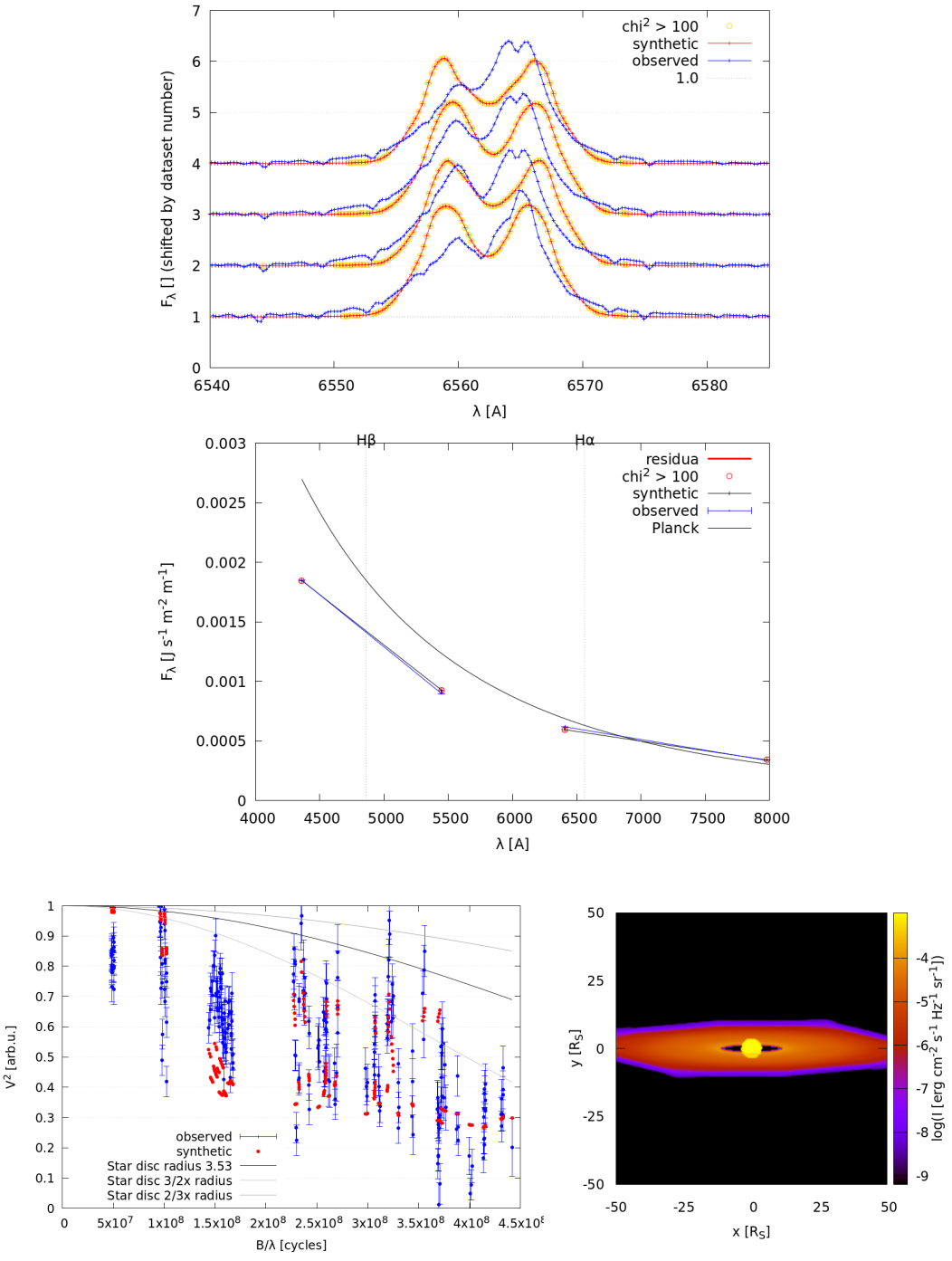

Figure 4.21: Model Nb-SPE-wind: the same as Fig. 4.20.

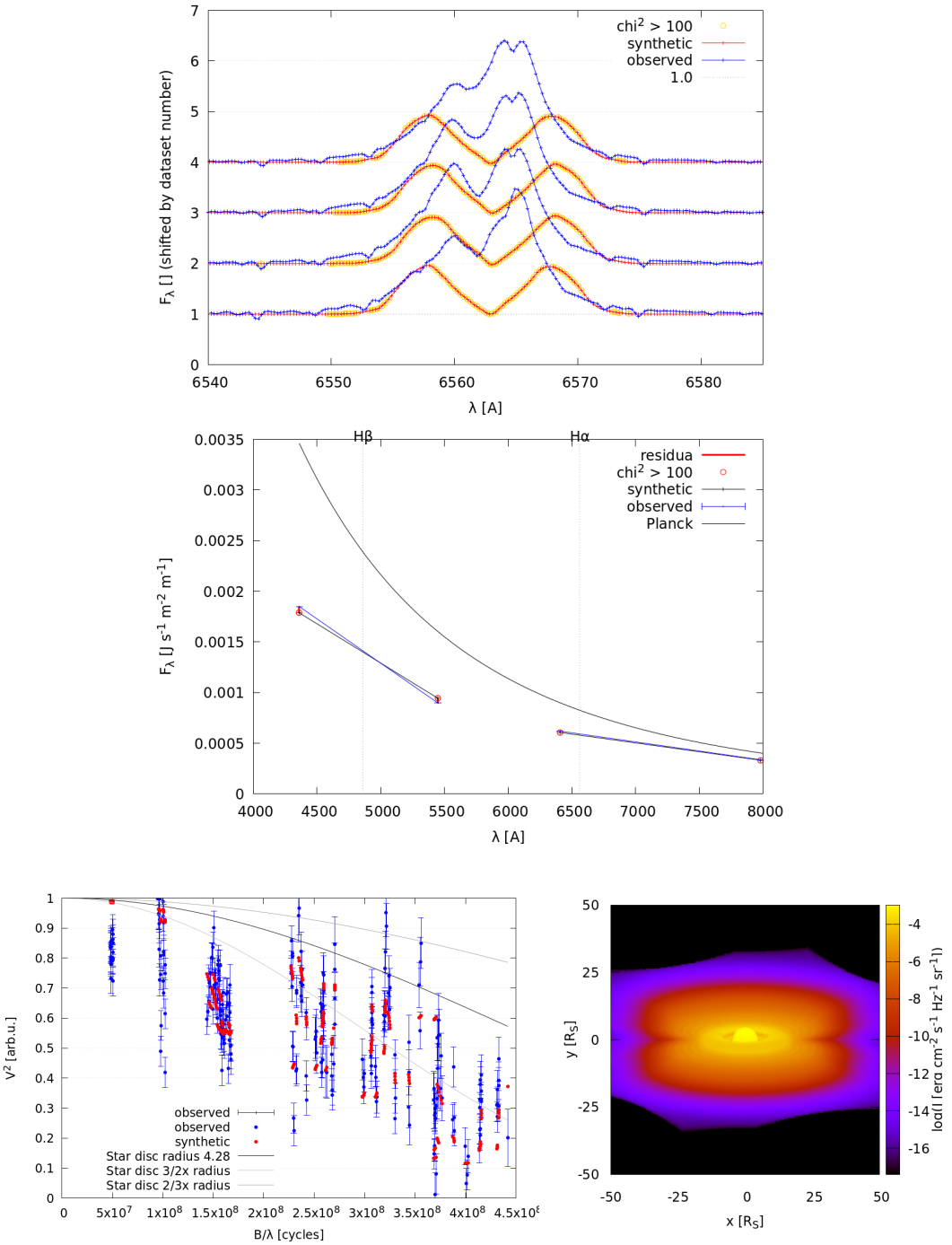

Figure 4.22: Model Nb-SPE-onlyWings: the same as Fig. 4.20.

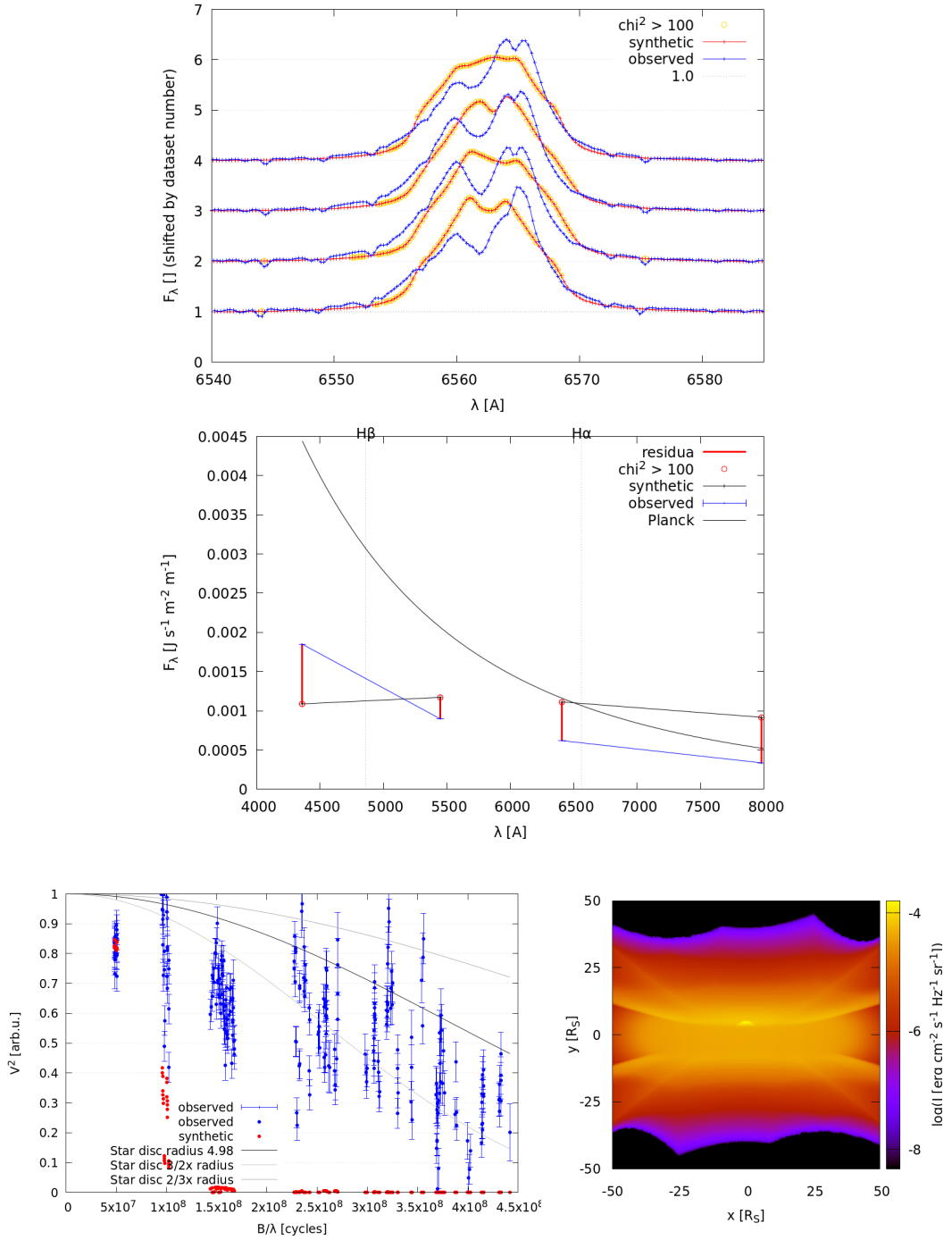

Figure 4.23: Model Nb-onlySPE: the same as Fig. 4.20. Note that in this case only the spectra were converged and the interferometry and SED data are shown only for reference.

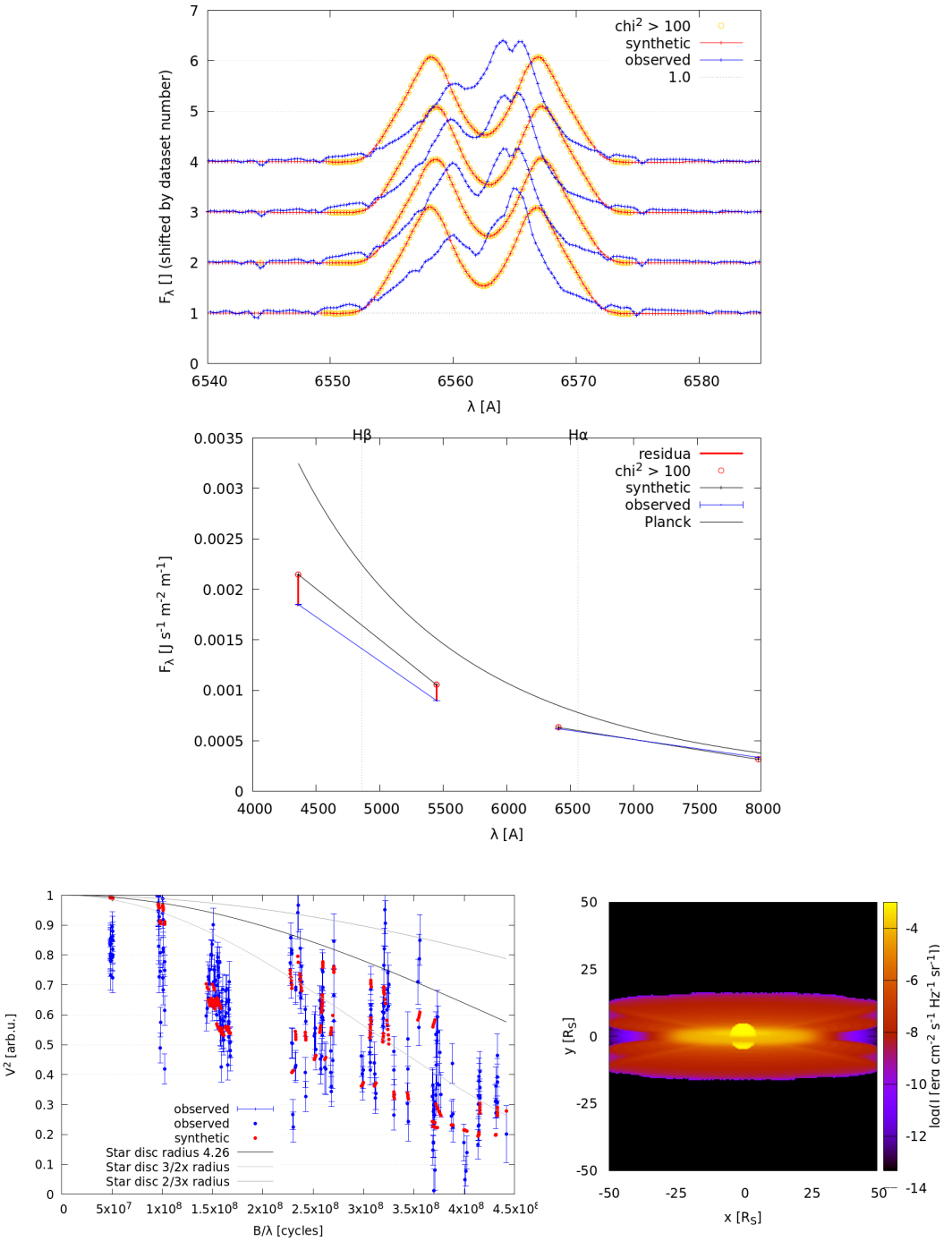

Figure 4.24: Model Nb-SPE-Restricted: the same as Fig. 4.20.

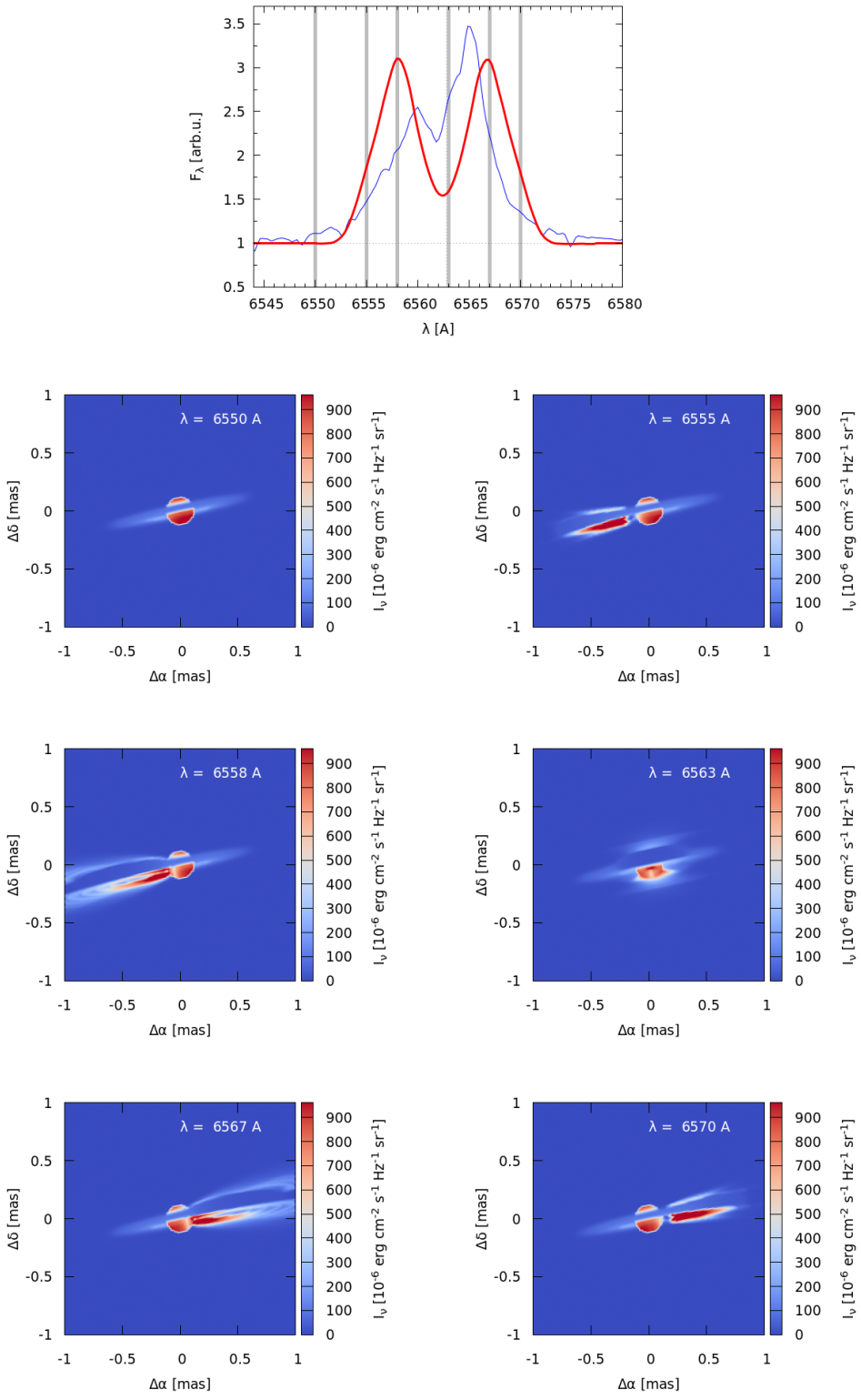

Figure 4.25: Model Nb-SPE-Restricted: flaring of the disc in the Hα region. Top: Hα synthetic (red) and observed (blue) profile. The grey vertical lines denote the wavelength of the synthetic images below. Bottom set of six: synthetic images where he system is rotated as seen on the celestial sphere and coloured by the value of the synthetic intensity.

5. Discussion

5.1 Spectra analysis

φ Per proved to be an interesting and challenging system. In Chapter 3, I studied nearly 400 spectra, namely the radial velocities, equivalent widths, central intensities and V/R ratios of Balmer lines Hα, Hβ, Hγ and the line He I λ6678.

Fortunately the times of observation of the BeSS spectra complement the Ondřejov observations very well and their combination showed clear long-term variations in all the aforementioned observables.

I attempted to remove the observed long-term variation of radial velocities in order to find an orbital solution. To do this, I split the measurements into 19 datasets each having its own systemic velocity. The datasets must had been neither too few to describe well the secular changes nor too many as then the orbital solution would be lost.

Nevertheless I was also able to measure old spectra of Hγ and include them in the orbital solution, as well as data from the IUE and HST spacecrafts. This gives a robust result of the ephemeris spanning more than 120 years. There is a clear inconsistency in determining the mass of the primary, as can be seen in Tab 5.1. It should be noted, however, that in this work I used data from both HST and IUE, unlike both Gies et al. [1998] and Mourard et al. [2015] who only used the HST data. Their inclusion lead to a higher value of the amplitude K_2 and consequently $M_1 \sin^3(i)$.

It should be noted that even after removing the long term variation there is a spread of velocities of about $\pm 10\,\mathrm{km{\cdot}s^{-1}}$ in the phase diagram. It might originate from too sparse selection of the seed-points as well as errors in measuring the velocities. Though I attempted to reduce the error by measuring the RVs multiple times. Another reason may be a presence of some additional variations of the system that was not taken into consideration.

This is also indicated by the measurements of central intensity, equivalent width and V/R ratio as they are less dependent on the user performing the tasks and even these showed dispersion. The V/R ratio undergoes cyclic changes about five years long. At the same time the equivalent width of Hα and its central intensity vary in yet another mode and they seem to be linked together.

$M_1 \sin^3(i)$ [$M_\odot$]	Error [$M_\odot$]	Source
16.35	2.83*	Božić et al. [1995]
8.91	0.26	Gies et al. [1998]
8.94	0.28	Mourard et al. [2015]*
11.84	0.64	this work

Table 5.1: Comparison of previously published masses for the primary component. Note that Božić et al. [1995] did not publish the error of their computation for the mass and it was estimated based on the relevant values and their uncertainties presented in their work. Mourard et al. [2015] in their work published the value $M \sin^3(i)/\sin^3(i)$, which was calculated using their found value of i.

5.2 Modeling

Before the use of PYSHELLSPEC, I used the program LITpro to construct a purely geometrical model in order to reproduce the result of Mourard et al. [2015]. While the star was approximated as a uniform disk, the circumstellar matter by a Gaussian distribution of intensity. I found that the radius of the star is not well constrained as the incoming flux overflows between the uniform disk and the Gaussian. I therefore fixed its value to the one derived from its presumed size and distance. It should be noted, that this differs from the approach of Mourard et al. [2015], who let its diameter converge and received different results with much smaller value and, as a consequence, so differ the flux ratios as well. On the other hand, both models reached the same value of the position angle.

During the modeling, only red continuum interferometry was considered and the Hα line was not included. This is due to SHELLSPEC, which computes monochromatic synthetic images. While in the continuum region it is safe to assume that the spatial distribution of the intensity is nearly constant with respect to the wavelength, it would not be correct to treat the broad-band interferometry in the region with such a prominent line in the same way.

Another potential solution and a new source of constrains could be to use self-calibrated narrow-band interferometric observations as presented in the work of Mourard et al. [2015]. These, however, use a cross-correlation with the broad-band image and it would be necessary to compute multiple synthetic images across the Hα line ad their subsequent flux-weighted averaging. This, however, requires a substantial modification of the PYSHELLSPEC code.

Similar arguments were made for the removal of the U band from the modeling of SED due to the presence of the Balmer jump. Furthermore, scattering, which is treated by the program only parametrically, might be significant in this spectral region.

An assumption within the SHELLSPECcode is that all the matter the light rays pass through is in the local thermodynamic equilibrium (LTE). This may not hold true in some parts of the disc, mainly areas with low density and high temperature. It is, however, difficult to quantify the difference between the two approaches as a non-LTE model is substantially different from the LTE one. Also, while the radiative transfer within the disc is treated as in LTE, the synthetic spectra used to model the primary star are, actually, computed for non-LTE conditions.

One obvious shortcoming of the models presented is that over the entire modeling a spherical shape of the primary star was assumed. This is definitely not the case as it is almost critically rotating, which can be seen from the very broadened photospheric lines. Such shape causes the temperature at the equator to be significantly lower than at the pole by a factor of about 1.16 (from Eq. 1.15 assuming 3/2 ratio in radius). The parameters $T^{\rm star}$ and $R^{\rm star}$ then refer to some mean value between the polar and equatorial one. This mean value is most likely weighted by the flux as it is only constrained from the interferometry. It is also important to note that some of the synthetic flux may overflow between the two objects.

Recently, a communication with Dr. J. Budaj brought this issue to his attention. He was able to finish a new update utilizing the method described in Section

1.2.1, namely Eq. (1.14) governing the shape of the primary star. Unfortunately, by the time of implementation, this work has been reaching its final stages and it was not possible to include it.

An important factor of the metallicity of the star as well as the surrounding circumstellar matter has not been addressed. Instead, solar metallicity was assumed. The true metallicity may be difficult to estimate. A large portion of the mass of the primary and presumably the disc came from the more evolved secondary during the mass transfer period. The evolution calculations made by Schootemeijer et al. [2018] yield that only about 40% of the current mass originally belonged to the primary while 60% was transferred from its companion, which is now a stripped-down helium dwarf.

Overall, this work significantly expands the work done by Mourard et al. [2015] as it uses realistic radiative transfer computation. Especially, it includes the addition of spectral energy distribution and individual spectral lines, which provide significant constrains on the model. Even though it supports their model of a relatively small disc surrounding the primary star, there are some caveats.

In particular, the spectral line profiles were not reproduced exactly, it is possible that a part of the incoming flux affecting the lines might originate in a different structure. Consequently, another step in the modeling would be addition of a shell surrounding the disc that is visible purely in Hα and only slightly contributes to the continuum. Another possibility is addition of an assymetric hot region facing the companion. This presence of a long-lived asymmetric structure in the disc, which is suggested by the long-time spectral variations, was not yet examined.

Conclusions

The principal findings of this study can be summarized as follows. In Chapter 3, I examined a rich set of 398 spectra of the φ Per system, namely Balmer lines Hα, Hβ and Hγ as well as He I λ6678. From the measured as well as previously published radial velocities I determined the new ephemeris

$$T_{\mathrm{RV\ max}} = \mathrm{HJD}\ 2\,456\,929.72(67) + 126\overset{\mathrm{d}}{.}6446(69) \times E, \tag{5.1}$$

with the values of velocity amplitude $K_1 = 11.16$ and $K_2 = 89.34\,\mathrm{km{\cdot}s^{-1}}$, which corresponds to the masses $M \sin^3(i)$ of the primary and the secondary as 11.84 and $1.48\,\mathrm{M_\odot}$, respectively. The value of M_1 is a significant revision of the value published by Mourard et al. [2015] and provides a more self-consistent model of the primary. The result for M_2 gives a more massive He remnant, comparable to the Chandrasekhar limit for white dwarfs.

The measurements of radial velocities as well as the intensities, equivalent widths and V/R ratios of Balmer lines show long-term variations with different durations. The timescale of the V/R changes is similar to previously observed long term variations and corresponds to the viscous timescale.

In Chapter 4, I used complex radiative transfer computations to derive the physical parameters of the φ Per primary and the surrounding disc. I constructed a number of models in an attempt to reproduce the observed interferometric visibilities, spectral energy distribution (SED) and spectra using the program `PYSHELLSPEC`. It turned out to be important to account for *all* observational datasets, because the system's parameters are often constrained by different observables. This is a great advantage of the program used that it can account for these orthogonal measurements.

Out of the constructed models, the preferred model (denoted as 'Restr' in Table 4.8) consisted of a disc extended from 11 to $50\,\mathrm{R_\odot}$ with the temperature of 16.5 kK and density $4.4 \cdot 10^{-11}\,\mathrm{g{\cdot}cm^{-3}}$ at the inner rim. Moreover, it is possible that there is a more extended optically thin structure contributing to the Hα flux.

Considering the evolution of the system, there is a possible relation to the system β Lyr which is in an early stage with ongoing mass transfer [Mourard et al., 2018, Brož et al., 2021], while in the φ Per system the mass transfer already ceased. The primary (gainer) is well separated from its Roche lobe, but it is critically rotating and still surrounded by circumstellar matter. The secondary is also separated (contracted), but its rotation is sub-critical [Thaller et al., 1995, Gies et al., 1998].

Bibliography

H. A. Abt and S. G. Levy. Binaries among B2 - B5 IV, V absorption and emission stars. *The Astrophysical Journal Suppl. Ser.*, 36:241–258, Feb 1978. doi: 10.1086/190498.

T. G. Barnes, D. S. Evans, and T. J. Moffett. Stellar angular diameters and visual surface brightnesses - III. An improved definition of the relationship. *Monthly Notices of the Royal Astronomical Society*, 183:285–304, May 1978. doi: 10.1093/mnras/183.3.285.

M. S. Bessell. UBVRI photometry II: the Cousins VRI system, its temperature and absolute flux calibration, and relevance for two-dimensional photometry. *Publications of the Astronomical Society of the Pacific*, 91:589–607, October 1979. doi: 10.1086/130542.

J. E. Bjorkman. *Circumstellar Disks*, volume 497, page 239. 1997. doi: 10.1007/BFb0113487.

J. Bodensteiner, T. Shenar, and H. Sana. Investigating the lack of main-sequence companions to massive be stars. *A&A*, 641:A42, 2020. doi: 10.1051/0004-6361/202037640. URL `https://doi.org/10.1051/0004-6361/202037640`.

H. Božić, P. Harmanec, J. Horn, P. Koubský, G. Scholz, D. McDavid, A.-M. Hubert, and H. Hubert. Toward a consistent model of the B0.5IVe + sdO binary phi Persei. *Astronomy & Astrophysics*, 304:235, December 1995.

M. Brož, D. Mourard, J. Budaj, P. Harmanec, H. Schmitt, I. Tallon-Bosc, D. Bonneau, H. Božić, D. Gies, and M. Šlechta. Optically thin circumstellar medium in the β Lyr A system. *Astronomy & Astrophysics*, 645:A51, January 2021. doi: 10.1051/0004-6361/202039035.

C. F. Brown. BV photometry of the binary Be star Phi Persei. *Publications of the Astronomical Society of the Pacific*, 104:38–43, January 1992. doi: 10.1086/132955.

J. Budaj and M. T. Richards. A description of the shellspec code. *Contributions of the Astronomical Observatory Skalnate Pleso*, 34(3):167–196, October 2004.

W. W. Campbell. Six stars whose velocities in the line of sight are variable. *Astrophysical Journal*, 16, September 1902. doi: 10.1086/140954.

J. B. Cannon. The Orbit of ϕ Persei. *Journal of the Royal Astronomical Society of Canada*, 4:195, Jun 1910.

J. B. Cannon. A Note on ϕ Persei. *Journal of the Royal Astronomical Society of Canada*, 5:372, Dec 1911.

A. C. Carciofi, A. S. Miroshnichenko, A. V. Kusakin, J. E. Bjorkman, K. S. Bjorkman, F. Marang, K. S. Kuratov, P. García-Lario, J. V. Perea Calderón, J. Fabregat, and A. M. Magalhães. Properties of the δ Scorpii Circumstellar Disk from Continuum Modeling. *Astrophysical Journal*, 652(2):1617–1625, December 2006. doi: 10.1086/507935.

A. Chalabaev and J. P. Maillard. On the rapid spectral variability of Be-stars: High spectral resolution study of Gamma Cas, Phi Per, and 59 CYG. *Astronomy & Astrophysics*, 127:279–288, November 1983.

G. W. Collins. The Use of Terms and Definitions in the Study of be Stars (review Paper). In Arne Slettebak and Theodore P. Snow, editors, *IAU Colloq. 92: Physics of Be Stars*, page 3, January 1987.

A. Dapergolas, G. di Cola, A. Guarnieri, and G. Madama. Photoelectric Photometry of Some Be Stars. *Information Bulletin on Variable Stars*, 1920:1, Feb 1981.

O. Delaa, Ph. Stee, A. Meilland, J. Zorec, D. Mourard, Ph. Bério, D. Bonneau, O. Chesneau, J. M. Clausse, P. Cruzalebes, K. Perraut, A. Marcotto, A. Roussel, A. Spang, H. McAlister, T. ten Brummelaar, J. Sturmann, L. Sturmann, N. Turner, C. Farrington, and P. J. Goldfinger. Kinematics and geometrical study of the Be stars 48 Persei and ψ Persei with the VEGA/CHARA interferometer. *Astronomy & Astrophysics*, 529:A87, May 2011. doi: 10.1051/0004-6361/201015639.

J. R. Ducati. VizieR Online Data Catalog: Catalogue of Stellar Photometry in Johnson's 11-color system. *VizieR Online Data Catalog*, January 2002.

O. L. Dustheimer. Spectrographic observations of phi Persei. *Publications of Michigan Observatory*, 7:171–189, Jan 1939.

J. P. Frédette. The Riddle of Phi Persei. *Journal of the Royal Astronomical Society of Canada*, 19:185, Oct 1925.

D. R. Gies, C. Y. Willis, L. R. Penny, and D. McDavid. The He I 6678-wavelength emission line of Phi Persei - New evidence of the companion star. *Publications of the Astronomical Society of the Pacific*, 105:281–286, March 1993. doi: 10.1086/133143.

D. R. Gies, W. G. Bagnuolo, Jr., E. C. Ferrara, A. B. Kaye, M. L. Thaller, L. R. Penny, and G. J. Peters. Hubble Space Telescope Goddard High Resolution Spectrograph Observations of the Be + sdO Binary phi Persei. *Astrophysical Journal*, 493:440–450, January 1998. doi: 10.1086/305113.

D. R. Gies, W. G. Bagnuolo, Jr., E. K. Baines, T. A. ten Brummelaar, C. D. Farrington, P. J. Goldfinger, E. D. Grundstrom, W. Huang, H. A. McAlister, A. Mérand, J. Sturmann, L. Sturmann, Y. Touhami, N. H. Turner, D. W. Wingert, D. H. Berger, M. V. McSwain, J. P. Aufdenberg, S. T. Ridgway, A. L. Cochran, D. F. Lester, N. C. Sterling, J. E. Bjorkman, K. S. Bjorkman, and P. Koubský. CHARA Array K'-Band Measurements of the Angular Dimensions of Be Star Disks. *Astrophysical Journal*, 654:527–543, January 2007. doi: 10.1086/509144.

P. S. Goraya. Variability of the H-alpha emission in Phi Per. *Astronomy and Space Science*, 107:323–325, December 1984. doi: 10.1007/BF00653536.

M. Güssow. Lichtelektrische Beobachtungen veränderlicher Sterne. III. *Astronomische Nachrichten*, 237(19):321, Jan 1930. doi: 10.1002/asna.19292371902.

P. Guthnick and R. Prager. *Veröf. König Sternwarte Berlin-Babelsberg*, 2:1, 1918.

E. M. Halbedel. Current Microvariability for the Be Star phi Persei. *Information Bulletin on Variable Stars*, 2885:1, Mar 1986.

P. Harmanec. Review of observational facts about Be stars. *Hvar Observatory Bulletin*, 7(1):55–88, January 1983.

P. Harmanec, D. V. Bisikalo, A. A. Boyarchuk, and O. A. Kuznetsov. On the role of duplicity in the Be phenomenon. I. General considerations and the first attempt at a 3-D gas-dynamical modelling of gas outflow from hot and rapidly rotating OB stars in binaries. *Astronomy & Astrophysics*, 396:937–948, December 2002. doi: 10.1051/0004-6361:20021534.

P. Harmanec, J. Lipták, P. Koubský, H. Božić, J. Labadie-Bartz, M. Šlechta, S. Yang, and A. Harmanec. A new study of the spectroscopic binary 7 Vul with a Be star primary. *Astronomy & Astrophysics*, 639:A32, July 2020. doi: 10.1051/0004-6361/202037964.

E. M. Hendry. Masses and Orbital Elements of the Binary System Phi Persei. In *Bulletin of the American Astronomical Society*, volume 7 of *Bulletin of the American Astronomical Society*, page 268, March 1975.

E. M. Hendry. Toward a Model for the BE Binary System phi Per. In A. Slettebak, editor, *Be and Shell Stars*, volume 70 of *IAU Symposium*, page 429, 1976.

J. Horn, J. Kubát, P. Harmanec, P. Koubský, P. Hadrava, V. Šimon, S. Štefl, and P. Škoda. Spectroscopic orbit of the triple star 55 Ursae Majoris. *Astronomy & Astrophysics*, 309:521–529, May 1996.

W. Hummel and S. Štefl. The circumstellar structure of the Be shell star phi Persei. II. Modeling. *Astronomy & Astrophysics*, 368:471–483, March 2001. doi: 10.1051/0004-6361:20000559.

J. A. Hynek. The Helium Anomaly in phi Persei. *Astrophysical Journal*, 100:151, September 1944. doi: 10.1086/144652.

M. M. Jarad, R. W. Hilditch, and Ian Skillen. A radial-velocity study of 18 emission-line B stars. *Monthly Notices of the Royal Astronomical Society*, 238: 1085–1106, Jun 1989. doi: 10.1093/mnras/238.4.1085.

M. Jaschek, A. Slettebak, and C. Jaschek. Be star terminology. *Be Star Newsletter*, 4:9–11, January 1981.

C. E. Jones, C. Tycner, T. A. A. Sigut, J. A. Benson, and D. J. Hutter. A Parameter Study of Classical Be Star Disk Models Constrained by Optical Interferometry. *Astrophysical Journal*, 687(1):598–607, November 2008. doi: 10.1086/591726.

F. C. Jordan. Spectrographic observations of [phi] Persei. *Publications of the Allegheny Observatory of the University of Pittsburgh*, 3:31–41, 1916.

R. Kippenhahn and A. Weigert. Entwicklung in engen Doppelsternsystemen I. Massenaustausch vor und nach Beendigung des zentralen Wasserstoff-Brennens. *Zeitschrift für Astrophysik*, 65:251, January 1967.

S. Kříž and P. Harmanec. A Hypothesis of the Binary Origin of Be Stars. *Bulletin of the Astronomical Institutes of Czechoslovakia*, 26:65, January 1975.

Th. Lanz and I. Hubený. A Grid of Non-LTE Line-blanketed Model Atmospheres of O-Type Stars. *The Astrophysical Journal Suppl. Ser.*, 146(2):417–441, June 2003. doi: 10.1086/374373.

Th. Lanz and I. Hubený. A grid of NLTE line-blanketed model atmospheres of early b-type stars. *The Astrophysical Journal Supplement Series*, 169(1): 83–104, mar 2007. doi: 10.1086/511270. URL `https://doi.org/10.1086/511270`.

W. J. S. Lockyer. The spectrum of φ Persei (type Bope). *Monthly Notices of the Royal Astronomical Society*, 85:580, May 1925. doi: 10.1093/mnras/85.7.580.

W. J. S. Lockyer. The spectrum of phi Persei (Sp. Type Bope) throughout a complete cycle (1925-26). *Monthly Notices of the Royal Astronomical Society*, 86:474, May 1926. doi: 10.1093/mnras/86.7.474.

L. B. Lucy and M. A. Sweeney. Spectroscopic binaries with circular orbits. *Astronomical Journal*, 76:544–556, August 1971.

H. Ludendorff. Über das Spektrum und die Radialgeschwindigkeit von phi Persei. *Astronomische Nachrichten*, 186:17, September 1910. doi: 10.1002/asna.19101860202.

H. Ludendorff. Weitere Untersuchungen über die Radialgeschwindigkeit von φ Persei. *Astronomische Nachrichten*, 192(11):173, Aug 1912. doi: 10.1002/asna.19121921102.

H. A. McAlister, T. A. ten Brummelaar, D. R. Gies, W. Huang, Jr. W. G. Bagnuolo, M. A. Shure, J. Sturmann, L. Sturmann, N. H. Turner, S. F. Taylor, D. H. Berger, E. K. Baines, E. Grundstrom, C. Ogden, S. T. Ridgway, and G. van Belle. First results from the CHARA array. i. an interferometric and spectroscopic study of the fast rotator α leonis (regulus). *The Astrophysical Journal*, 628(1):439–452, jul 2005. doi: 10.1086/430730. URL `https://doi.org/10.1086%2F430730`.

A. Meilland, P. Stee, M. Vannier, F. Millour, A. Domiciano de Souza, F. Malbet, C. Martayan, F. Paresce, R. G. Petrov, A. Richichi, and A. Spang. First direct detection of a Keplerian rotating disk around the Be star α Arae using AMBER/VLTI. *Astronomy & Astrophysics*, 464(1):59–71, March 2007. doi: 10.1051/0004-6361:20064848.

G. R. Miczaika. Über das System ψ Persei. Mit 6 Textabbildungen. *Zeitschrift fur Astrophysik*, 28:43, Jan 1950.

D. Mourard, J. M. Clausse, A. Marcotto, K. Perraut, I. Tallon-Bosc, Ph. Bério, A. Blazit, D. Bonneau, S. Bosio, Y. Bresson, O. Chesneau, O. Delaa, F. Hénault, Y. Hughes, S. Lagarde, G. Merlin, A. Roussel, A. Spang, Ph. Stee, M. Tallon, P. Antonelli, R. Foy, P. Kervella, R. Petrov, E. Thiebaut, F. Vakili, H. McAlister, T. ten Brummelaar, J. Sturmann, L. Sturmann, N. Turner, C. Farrington, and P. J. Goldfinger. VEGA: Visible spEctroGraph and polArimeter for the CHARA array: principle and performance. *Astronomy & Astrophysics*, 508(2):1073–1083, December 2009. doi: 10.1051/0004-6361/200913016.

D. Mourard, J. D. Monnier, A. Meilland, D. Gies, F. Millour, M. Benisty, X. Che, E. D. Grundstrom, R. Ligi, G. Schaefer, F. Baron, S. Kraus, M. Zhao, E. Pedretti, P. Berio, J. M. Clausse, N. Nardetto, K. Perraut, A. Spang, P. Stee, I. Tallon-Bosc, H. McAlister, T. ten Brummelaar, S. T. Ridgway, J. Sturmann, L. Sturmann, N. Turner, and C. Farrington. Spectral and spatial imaging of the Be+sdO binary ϕ Persei. *Astronomy & Astrophysics*, 577:A51, May 2015. doi: 10.1051/0004-6361/201425141.

D. Mourard, M. Brož, J. A. Nemravová, P. Harmanec, J. Budaj, F. Baron, J. D. Monnier, G. H. Schaefer, H. Schmitt, I. Tallon-Bosc, J. T. Armstrong, E. K. Baines, D. Bonneau, H. Božić, J. M. Clausse, C. Farrington, D. Gies, J. Juryšek, D. Korčáková, H. McAlister, A. Meilland, N. Nardetto, P. Svoboda, M. Šlechta, M. Wolf, and P. Zasche. Physical properties of β Lyrae A and its opaque accretion disk. *Astronomy & Astrophysics*, 618:A112, October 2018. doi: 10.1051/0004-6361/201832952.

C. Neiner, B. de Batz, F. Cochard, M. Floquet, A. Mekkas, and V. Desnoux. The Be Star Spectra (BeSS) Database. *Astronomical Journal*, 142(5):149, November 2011. doi: 10.1088/0004-6256/142/5/149.

John A Nelder and Roger Mead. A simplex method for function minimization. *The computer journal*, 7(4):308–313, 1965.

J. A. Nemravová, P. Harmanec, M. Brož, D. Vokrouhlický, D. Mourard, C. A. Hummel, C. Cameron, J. M. Matthews, C. T. Bolton, H. Bozi´c, R. Chini, T. Dembsky, S. Engle, C. Farrington, J. H. Grunhut, D. B. Guenther, E. F. Guinan, D. Korcáková, P. Koubský, R. Krícek, R. Kuschnig, P. Mayer, G. P. McCook, A. F. J. Moffat, N. Nardetto, A. Prsa, J. Ribeiro, J. Rowe, S. Rucinski, P. Skoda, M. Slechta, I. Tallon-Bosc, V. Votruba, W. W. Weiss, M. Wolf, P. Zasche, and R. T. Zavala. i: a unique laboratory to study the dynamic interaction in a compact hierarchical quadruple system. *A&A*, 594:A55, 2016. doi: 10.1051/0004-6361/201628860. URL `https://doi.org/10.1051/0004-6361/201628860`.

A. T. Okazaki. Long-Term V/R Variations of Be Stars Due to Global One-Armed Oscillations of Equatorial Disks. *Publications of the Astronomical Society of Japan*, 43:75–94, February 1991.

R. D. Oudmaijer and A. M. Parr. The binary fraction and mass ratio of Be and B stars: a comparative Very Large Telescope/NACO study. *Monthly Notices*

of the Royal Astronomical Society, 405(4):2439–2446, July 2010. doi: 10.1111/j.1365-2966.2010.16609.x.

G. J. Peters. Evidence for the Existence of Mass-Exchange Binary be Stars from Periodic Spectral Variations. In Arne Slettebak, editor, *Be and Shell Stars*, volume 70 of *IAU Symposium*, page 417, January 1976.

G. J. Peters, D. R. Gies, E. D. Grundstrom, and M. V. McSwain. Detection of a Hot Subdwarf Companion to the Be Star FY Canis Majoris. *Astrophysical Journal*, 686(2):1280–1291, October 2008. doi: 10.1086/591145.

G. J. Peters, T. D. Pewett, D. R. Gies, Y. N. Touhami, and E. D. Grundstrom. Far-ultraviolet Detection of the Suspected Subdwarf Companion to the Be Star 59 Cygni. *Astrophysical Journal*, 765(1):2, March 2013. doi: 10.1088/0004-637X/765/1/2.

G. J. Peters, L. Wang, D. R. Gies, and E. D. Grundstrom. The Hot Companion and Circumbinary Disk of the Be Star HR 2142. *Astrophysical Journal*, 828 (1):47, September 2016. doi: 10.3847/0004-637X/828/1/47.

R. Poeckert. He II emission in the Be star Phi Persei. *The Astrophysical Journal*, 233:L73–L75, October 1979. doi: 10.1086/183079.

R. Poeckert. A spectroscopic study of the binary Be star Phi Persei. *Publications of the Astronomical Society of the Pacific*, 93:297–317, June 1981. doi: 10.1086/130828.

R. S. Polidan. On the Detection of Binary be Stars. In Arne Slettebak, editor, *Be and Shell Stars*, volume 70 of *IAU Symposium*, page 401, January 1976.

O. R. Pols, J. Cote, L. B. F. M. Waters, and J Heise. The formation of be stars through close binary evolution. *Astronomy and Astrophysics*, 241:419–438, 1991.

A. Quirrenbach, D. F. Buscher, D. Mozurkewich, C. A. Hummel, and J. T. Armstrong. Maximum-entropy maps of the Be shell star dzeta Tauri from optical long-baseline interferometry. *Astronomy & Astrophysics*, 283:L13–L16, March 1994.

A. Quirrenbach, K. S. Bjorkman, J. E. Bjorkman, C. A. Hummel, D. F. Buscher, J. T. Armstrong, D. Mozurkewich, N. M. Elias, II, and B. L. Babler. Constraints on the Geometry of Circumstellar Envelopes: Optical Interferometric and Spectropolarimetric Observations of Seven Be Stars. *Astrophysical Journal*, 479:477–496, April 1997. doi: 10.1086/303854.

Th. Rivinius, D. Baade, and S. Stefl. Non-radially pulsating be stars*. *A&A*, 411 (2):229–247, 2003. doi: 10.1051/0004-6361:20031285.

Th. Rivinius, A. C. Carciofi, and Ch. Martayan. Classical Be stars. Rapidly rotating B stars with viscous Keplerian decretion disks. *The Astronomy and Astrophysics Review*, 21:69, October 2013. doi: 10.1007/s00159-013-0069-0.

H. F. Schiefer. A Spectrographic Study of φ Persei. *Astrophysical Journal*, 84: 568, Dec 1936. doi: 10.1086/143784.

A. Schootemeijer, Y. Götberg, S. E. de Mink, D. Gies, and E. Zapartas. Clues about the scarcity of stripped-envelope stars from the evolutionary state of the sdO+Be binary system phi Persei. *Astronomy & Astrophysics*, 615:A30, July 2018. doi: 10.1051/0004-6361/201731194.

A. Secchi. Schreiben des herrn prof. secchi, dir. der sternwarte des collegio romano, an den herausgeber. *Astronomische Nachrichten*, 68(4):63–64, 1867. doi: 10.1002/asna.18670680405.

J. Silaj, C. E. Jones, C. Tycner, T. A. A. Sigut, and A. D. Smith. A SYSTEMATIC STUDY OF h PROFILES OF be STARS. *The Astrophysical Journal Supplement Series*, 187(1):228–250, mar 2010. doi: 10.1088/0067-0049/187/1/228.

M. Singh, M. Mon, T. Kogure, and M. Suzuki. Spectroscopic Study of the Be Star Phi Persei. *Publications of the Astronomical Society of Japan*, 46:27–43, Feb 1994.

A. Slettebak. On the Axial Rotation of the Brighter O and B Stars. *Astrophysical Journal*, 110:498, Nov 1949. doi: 10.1086/145226.

O. Struve. On the Origin of Bright Lines in Spectra of Stars of Class B. *Astrophysical Journal*, 73:94, March 1931. doi: 10.1086/143298.

O. Struve and K. Wurm. The Excitation of Absorption Lines in Outer Atmospheric Shells of Stars. *Astrophysical Journal*, 88:84, Jul 1938. doi: 10.1086/143961.

I. Tallon-Bosc, M. Tallon, E. Thiébaut, C. Béchet, G. Mella, S. Lafrasse, O. Chesneau, A. Domiciano de Souza, G. Duvert, D. Mourard, R. Petrov, and M. Vannier. LITpro: a model fitting software for optical interferometry. In Markus Schöller, William C. Danchi, and Françoise Delplancke, editors, *Optical and Infrared Interferometry*, volume 7013, pages 491 – 499. International Society for Optics and Photonics, SPIE, 2008. doi: 10.1117/12.788871. URL `https://doi.org/10.1117/12.788871`.

T. A. ten Brummelaar, H. A. McAlister, S. T. Ridgway, Jr. Bagnuolo, W. G., N. H. Turner, L. Sturmann, J. Sturmann, D. H. Berger, C. E. Ogden, R. Cadman, W. I. Hartkopf, C. H. Hopper, and M. A. Shure. First Results from the CHARA Array. II. A Description of the Instrument. *Astrophysical Journal*, 628(1):453–465, July 2005. doi: 10.1086/430729.

M. L. Thaller, W. G. Bagnuolo, Jr., D. R. Gies, and L. R. Penny. Tomographic Separation of Composite Spectra. III. Ultraviolet Detection of the Hot Companion of phi Persei. *Astrophysical Journal*, 448:878, August 1995. doi: 10.1086/176016.

Y. Touhami, D. R. Gies, G. H. Schaefer, H. A. McAlister, S. T. Ridgway, N. D. Richardson, R. Matson, E. D. Grundstrom, T. A. ten Brummelaar, P. J. Goldfinger, L. Sturmann, J. Sturmann, N. H. Turner, and C. Farrington. A CHARA Array Survey of Circumstellar Disks around Nearby Be-type Stars. *Astrophysical Journal*, 768(2):128, May 2013. doi: 10.1088/0004-637X/768/2/128.

C. Tycner, G. C. Gilbreath, R. T. Zavala, J. T. Armstrong, J. A. Benson, Arsen R. Hajian, D. J. Hutter, C. E. Jones, T. A. Pauls, and N. M. White. Constraining Disk Parameters of Be Stars using Narrowband Hα Interferometry with the Navy Prototype Optical Interferometer. *Astronomical Journal*, 131(5):2710–2721, Jun 2006. doi: 10.1086/502679.

S. Štefl, W. Hummel, and T. Rivinius. The circumstellar structure of the Be shell star phi Per. I. Data analysis. *Astronomy & Astrophysics*, 358:208–220, June 2000.

H. von Zeipel. The radiative equilibrium of a slightly oblate rotating star. *Monthly Notices of the Royal Astronomical Society*, 84:684–701, June 1924. doi: 10.1093/mnras/84.9.684.

L. Wang, D. R. Gies, and G. J. Peters. Detection of the Ultraviolet Spectrum of the Hot Subdwarf Companion of 60 Cygni (B1 Ve) from a Survey of IUE Spectra of Be Stars. *Astrophysical Journal*, 843(1):60, July 2017. doi: 10.3847/1538-4357/aa740a.

L. Wang, D. R. Gies, and G. J. Peters. Detection of Additional Be+sdO Systems from IUE Spectroscopy. *Astrophysical Journal*, 853(2):156, February 2018. doi: 10.3847/1538-4357/aaa4b8.

J. P. Wisniewski, Z. H. Draper, K. S. Bjorkman, M. R. Meade, J. E. Bjorkman, and A. F. Kowalski. DISK-LOSS AND DISK-RENEWAL PHASES IN CLASSICAL be STARS. i. ANALYSIS OF LONG-TERM SPECTROPOLARIMETRIC DATA. *The Astrophysical Journal*, 709(2):1306–1320, jan 2010. doi: 10.1088/0004-637x/709/2/1306.

M. Wolf, P. Harmanec, H. Božić, P. Koubský, S. Yang, D. Ruždjak, M. Šlechta, H. Ak, H. Bakış, V. Bakış, A. Oplištilová, and K. Vitovský. Long-term, orbital, and rapid variations of the Be star V923 Aql = HD 183656$\star$. *Astronomy & Astrophysics*, 647:A97, March 2021. doi: 10.1051/0004-6361/202039740.